Dijet production in polarized proton-proton collisions at $\sqrt{s} = 200$ GeV

by

Matthew Walker

Submitted to the Department of Physics
in partial fulfillment of the requirements for the degree of

Doctor of Philosophy in Physics

at the

MASSACHUSETTS INSTITUTE OF TECHNOLOGY

June 2011

Author .....
Department of Physics
April 29, 2011

Certified by .....
Bernd Surrow
Associate Professor
Thesis Supervisor

Accepted by .....
Krishna Rajagopal
Associate Department Head for Education

Dijet production in polarized proton-proton collisions at $\sqrt{s} = 200$ GeV

by

Matthew Walker

Submitted to the Department of Physics
on April 29, 2011, in partial fulfillment of the
requirements for the degree of
Doctor of Philosophy in Physics

Abstract

Polarized deep inelastic scattering (DIS) experiments indicate that quarks only carry approximately 30% of the proton spin, which led to interest in measuring the contributions of other components. Through polarized proton-proton collisions at the Relativistic Heavy Ion Collider (RHIC), the world's only polarized proton collider, it is possible to make an extraction of the polarized gluon distribution function $\Delta g(x)$. This function describes the contribution of the gluon polarization to the proton spin.

This thesis presents a measurement of the $p + p \rightarrow$ Jet + Jet + X (dijet) cross section from the 2005 RHIC running period and a measurement of the longitudinal double spin asymmetry A_{LL} from the 2009 RHIC running period, both made using the Solenoidal Tracker at RHIC (STAR). The cross section is measured over the invariant mass range $20 < M < 116$ GeV/c^2 with systematic uncertainties between 20 and 50%, driven by the jet energy scale uncertainty. The asymmetry is measured over the invariant mass range $20 < M < 80$ GeV/c^2 in three different detector acceptances.

The asymmetry measurement is compared to several theory scenarios in each of the detector acceptances, which allows extraction of the shape of the polarized gluon distribution function $\Delta g(x)$. The results are consistent with a small, but positive, total gluon polarization.

Thesis Supervisor: Bernd Surrow
Title: Associate Professor

Acknowledgments

There are many people who I need to thank for helping make this thesis possible. First, my advisor, Bernd Surrow, whose passion for the RHIC-Spin program and dedication to producing important results allowed me to work on this exciting analysis and whose support helped me forge ahead. Bob Redwine provided important guidance in navigating the political waters of the STAR collaboration and in managing the thesis writing "problem."

I am in debt to many people who supported and scrutinized this analysis, the core of whom were past and present members of the RHIC-Spin group: Renee Fatemi, Ross Corliss, Fang Guo, James Hays-Wehle, Alan Hoffman, Chris Jones, Adam Kocoloski, William Leight and Tai Sakuma. Special mentions need to be made for Jan Balewski, whose enthusiasm led to my simulation being completed on the cloud, and for Joe Seele and Mike Betancourt, for many discussions about all aspects of the analysis and support in the face of adversity. Members of the STAR collaboration deserve my gratitude. Stephen Trentalange has been exceptionally supportive and taught me much about calorimeters. Jérôme Lauret helped me explore cloud computing in physics and supported my efforts as part of the Software and Computing team.

Many people gave me opportunities to enjoy life outside of work, including the members of Statmechsocial, Physics GSC, Ultimate Pickup and the Sidney-Pacific community. Roger and Dottie Mark and Roland Tang and Annette Kim have kept me well fed over the past few years. Nan Gu pressed me to get involved in many extracurriculars. The Feng and Benz families have been enormously supportive. My brother, Nick, and sister, Liz, never failed to lift my spirits or to let me get complacent.

My girlfriend has supported, entertained and commiserated with me even as she works on her own doctoral studies. Thank you for putting up with me, Annie.

Finally, I can hardly express the gratitude I have for my parents. From them, I have inherited my curiosity, pragmatism and perseverance. They have supported and prodded me through many challenges and have always looked out for my best interests. Mom, Dad, Thank you.

Contents

List of Figures

List of Tables

Chapter 1

Introduction

The proton is a composite particle made up of quarks and gluons whose interactions are described by quantum chromodynamics (QCD). The spin structure of the proton remains an area of intense study by both experimentalists and theorists. It can be described in a simple picture as

$$\frac{1}{2} = \frac{1}{2}\Delta\Sigma + L_q + \Delta G + L_g \tag{1.1}$$

where $\Delta\Sigma$ represents the quark spin contribution, ΔG represents the gluon spin contribution, and $L_{q(g)}$ represents the quark (gluon) orbital angular momentum. This relation can actually be constructed in QCD in the infinite momentum frame and the light cone gauge [5].

Chapter 1 discusses the theoretical background of understanding the proton spin, taking a historical approach.

Chapter 2 describes the experimental setup of the Relativistic Heavy Ion Collider (RHIC) and the Solenoidal Tracker at RHIC (STAR), which were used to measure the gluon polarization in proton-proton collisions.

Chapter 3 covers the theoretical basis of jets and discuss methods for finding jets with a focus on the methods used in this thesis.

Chapter 4 describes the simulation package used to help understand physics and detector effects that need to be corrected for in the measurement of jet observables

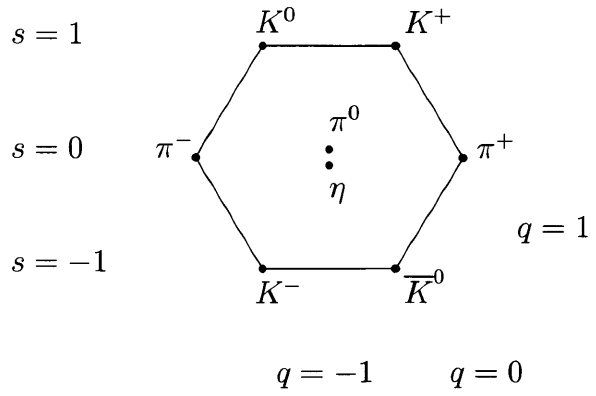

Figure 1-1: The particles arranged in the meson octet in the Eightfold Way have horizontal lines of constant strangeness and diagonal lines of constant electric charge

and methods used to improve the quality of those simulations.

Chapter 5 explains the measurement of the dijet cross section in the RHIC run 5 data collected at STAR.

Chapter 6 explains the measurement of the dijet longitudinal double-spin asymmetry in the RHIC run 9 data collected at STAR.

Chapter 7 discusses the impact of these measurements and what future work can be done to expand on their results.

1.1 Early Proton Structure

Discovery of the proton can be attributed to Rutherford [6], who proved in 1919 that nitrogen nuclei contained hydrogen nuclei. It was already known that the masses of the other nuclei were multiples of the mass of the hydrogen nuclei. Rutherford thus concluded that the hydrogen nucleus was a building block of the heavier nuclei and coined the term proton.

Hints that the proton had complicated internal structure included measurement of its anomalous magnet moment [7], but it was not until 1961 when Gell-Mann proposed the Eightfold Way to explain the growing numbers of hadrons being discovered in cosmic ray measurements and early accelerator experiments that there was a consistent way to describe that structure. Using charge and strangeness, Gell-Mann classified

the hadrons into a variety of multiplets based on their spin. The Quark Model, introduced by Gell-Man and Zweig in 1964, explained why the hadrons fit into categories so nicely by proposing that the hadrons were composite particles made of even smaller quarks.

The final touch to the quark model was the proposal that the quarks also carried a new kind of charge dubbed color by Greenberg [8]. This addition saved the quark model from conflict with the Pauli exclusion principle. The problem was caused by the Δ^{++}, which the quark model suggested was made up of three up quarks in the same state. By introducing color, Greenberg was able to defuse the problem and save the quark model. To explain why only certain combinations of quarks are found in nature, the theory also requires that only colorless particles are stable.

The quark model provides a simple explanation of all of the baryon spins. Three spin $\frac{1}{2}$ particles combine into two possible spin states,

$$\frac{1}{2} \otimes \frac{1}{2} \otimes \frac{1}{2} = \frac{3}{2} \oplus \frac{1}{2}.$$

Baryons with spin $\frac{1}{2}$ and $\frac{3}{2}$ are observed in nature, agreeing with the interpretation of quark generation of baryon spin. Thus, the origin of the proton's spin has a straightforward explanation in a static model of the proton structure.

1.2 Deep Inelastic Scattering

While the quark model successfully explained the hadron hierarchy, observation of isolated free quarks was impossible under its rules. However, experiments using charged lepton beams on proton targets in deep inelastic scattering (DIS) finally gave access to the proton structure. Figure 1-2 illustrates the DIS process. The idea behind using electrons to probe the structure is that the scattering cross section is proportional to the squared form factor $F(q)$ of a charge distribution [9]. The cross section can be written as

$$\frac{d\sigma}{d\Omega} = \left(\frac{d\sigma}{d\Omega}\right)_{point} |F(q)|^2 \tag{1.2}$$

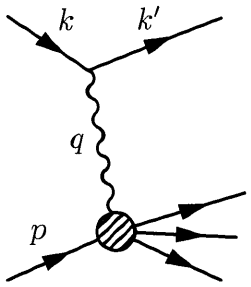

Figure 1-2: A simple Feynman diagram illustrating deep inelastic scattering (DIS), in which an electron scatters off a quark in the target proton.

where $F(q)$ is the Fourier transform of the charge distribution.

The situation becomes slightly more complicated for protons. The cross section for DIS can be described as

$$d\sigma \propto \frac{1}{Q^4} L^{\mu\nu} W_{\mu\nu}, \tag{1.3}$$

where $L^{\mu\nu}$ is the lepton tensor, which describes the physics on the lepton side of the photon propagator, and $W_{\mu\nu}$ is the hadronic tensor, which contains all of the information on the hadronic side.

In DIS, there are two Lorentz invariant quantities that describe the kinematics:

$$\begin{aligned} Q^2 &= -q^2 \\ x &= \frac{Q^2}{2p \cdot q} \end{aligned}$$

where q is the momentum transfer through the photon and p is the proton momentum. The variable x is called Bjorken-x and is often interpreted in the infinite momentum frame as the fraction of the proton momentum carried by the struck quark.

Using charge conservation and the fact that the lepton tensor $L^{\mu\nu}$ is symmetric, it's possible to write the hadronic tensor in terms of two structure functions $W_1(Q^2, x)$ and $W_2(Q^2, x)$. The cross section becomes

$$\frac{d\sigma}{d\Omega dE'} \propto \frac{1}{Q^4}(2W_1(Q^2, x)\sin^2\frac{\theta}{2} + W_2(Q^2, x)\cos^2\frac{\theta}{2}), \tag{1.4}$$

where θ is the angle of the scattered electron and E' is the energy of the scattered

electron.

Bjorken proposed that these functions are independent of Q^2 in the deep inelastic scattering regime, which is a consequence of the point like nature of the proton constituents. This behavior is called Bjorken scaling and was confirmed by experiments at SLAC [10]. In this regime, the structure functions are rewritten as

$$\begin{aligned} MW_1(Q^2, x) &\longrightarrow F_1(x) \\ \frac{Q^2}{2Mc^2x} W_2(Q^2, x) &\longrightarrow F_2(x). \end{aligned}$$

Callan and Gross went on to suggest that the two scaling functions are related by $2xF_1(x) = F_2(x)$, which was also confimed at SLAC.

In the parton model, the function $F_1(x)$ can be written as

$$F_1(x) = \frac{1}{2} \sum_i e_i^2 f_i(x), \tag{1.5}$$

where q_i is the charge of a quark, $f_i(x)$ is the individual quark distribution function, and the sum over i is over both quark and anti-quark flavors. The quark distribution functions can be thought of as probability distributions for the amount of the proton's momentum carried by quarks of a certain flavor.

The proton includes not only the two up and one down valence quarks that primarily govern its characteristics, but also a sea of quarks and gluons that mediate the strong interaction. Therefore, the proton structure function should be

$$2F_1(x) = (\frac{2}{3})^2[u(x) + \overline{u}(x)] + (\frac{1}{3})^2[d(x) + \overline{d}(x) + s(x) + \overline{s}(x)], \tag{1.6}$$

including the contributions of strange quarks, but not heavier quarks. The up quark distribution should have some contribution from the valence up quarks and some from the sea up quarks and the same for down quarks. We also expect all of the sea quarks

and anti-quarks should have approximately the same distributions:

$$\begin{aligned} u(x) &= u_{valence}(x) + u_{sea}(x) \\ d(x) &= d_{valence}(x) + d_{sea}(x) \\ u_{sea}(x) &= d_{sea}(x) = \overline{u}(x) = \overline{d}(x) = s(x) = \overline{s}(x). \end{aligned}$$

Adding in the constraint that the quantum numbers of the proton must be conserved provide sum rules for the quark distribution functions:

$$\begin{aligned} \int_0^1 [u(x) - \overline{u}(x)]dx &= 2, \\ \int_0^1 [d(x) - \overline{d}(x)]dx &= 1, \\ \int_0^1 [s(x) - \overline{s}(x)]dx &= 0. \end{aligned}$$

These sum rules, represented by the integrals over x, are actually sums over all quarks of the relevant flavor. The idea of a sum rule will be important below.

Using these quark distributions, it is possible to calculate the momentum fraction carried by all quarks, ϵ_q:

$$\epsilon_q = \int_0^1 x \sum_i q_i(x)dx = 1 - \epsilon_g, \tag{1.7}$$

where $q_i(x)$ are again the quark distribution functions and ϵ_g is the momentum fraction carried by gluons. Experimental measurements of $F_2(x)$ for both the proton and the neutron have found that $\epsilon_u = 0.36$ and $\epsilon_d = 0.18$. By neglecting the contribution from heavier quarks, that implies $\epsilon_g = 0.46$. So here is the first clear evidence that the effects of the gluon are important in understanding the proton.

The same framework of quark distribution functions can be used to discuss the spin component of the proton. The polarized quark distribution functions $\Delta q(x)$ are defined as [11]

$$\Delta q(x) \equiv q^{\uparrow} - q^{\downarrow}, \tag{1.8}$$

where $q^{\uparrow}$ is the quark distribution function for quarks that are polarized along the direction of the proton's polarization and $q^{\downarrow}$ is the quark distribution function for quarks with the opposite polarization. A quark spin-dependent structure function $g_1(x)$ is defined in terms of these distribution functions as

$$g_1(x) = \frac{1}{2}\sum_i e_i^2 \Delta q_i(x). \tag{1.9}$$

Ellis and Jaffe derived a sum rule for $g_1(x)$ by assuming an unpolarized quark sea [12] for polarized DIS on both proton and neutron targets:

$$\int_0^1 dx g_1^{ep}(x) = \frac{1.78}{12} g_A \tag{1.10}$$

$$\int_0^1 dx g_1^{en}(x) = \frac{-0.22}{12} g_A \tag{1.11}$$

where g_A is the axial vector coupling. Experimental values of $g_A = 1.248 \pm 0.010$ correspond to $\int_0^1 dx g_1^{ep}(x) = 0.185$.

Polarized DIS is sensitive to $g_1(x)$ by measuring two asymmetries [11]. $A_{\parallel}$ is the asymmetry for when the lepton and nucleon spins are aligned and anti-aligned longitudinally. $A_{\perp}$ is the asymmetry for a longitudinally polarized lepton and transversely polarized nucleon. Measurements of $g_1(x)$ made by the European Muon Collaboration (EMC), shown in Fig. 1-3, and the Spin Muon Collaboration (SMC) using polarized muons on polarized proton and deuteron targets found significant disagreements with the Ellis-Jaffe calculation.

The contribution of the quark spin to the spin of the nucleon $\Delta\Sigma$ can be written in this framework as

$$\Delta\Sigma = \int_0^1 dx \sum_i (\Delta q_i(x) + \Delta\overline{q}_i(x)). \tag{1.12}$$

If all of the spin of the nucleon came from the quark spins, $\Delta\Sigma$ would be one. In Ellis and Jaffe's calculation, $\Delta\Sigma = 0.59$, and the rest is presumed to come from quark angular momentum. The discrepancy between the Ellis-Jaffe number and the

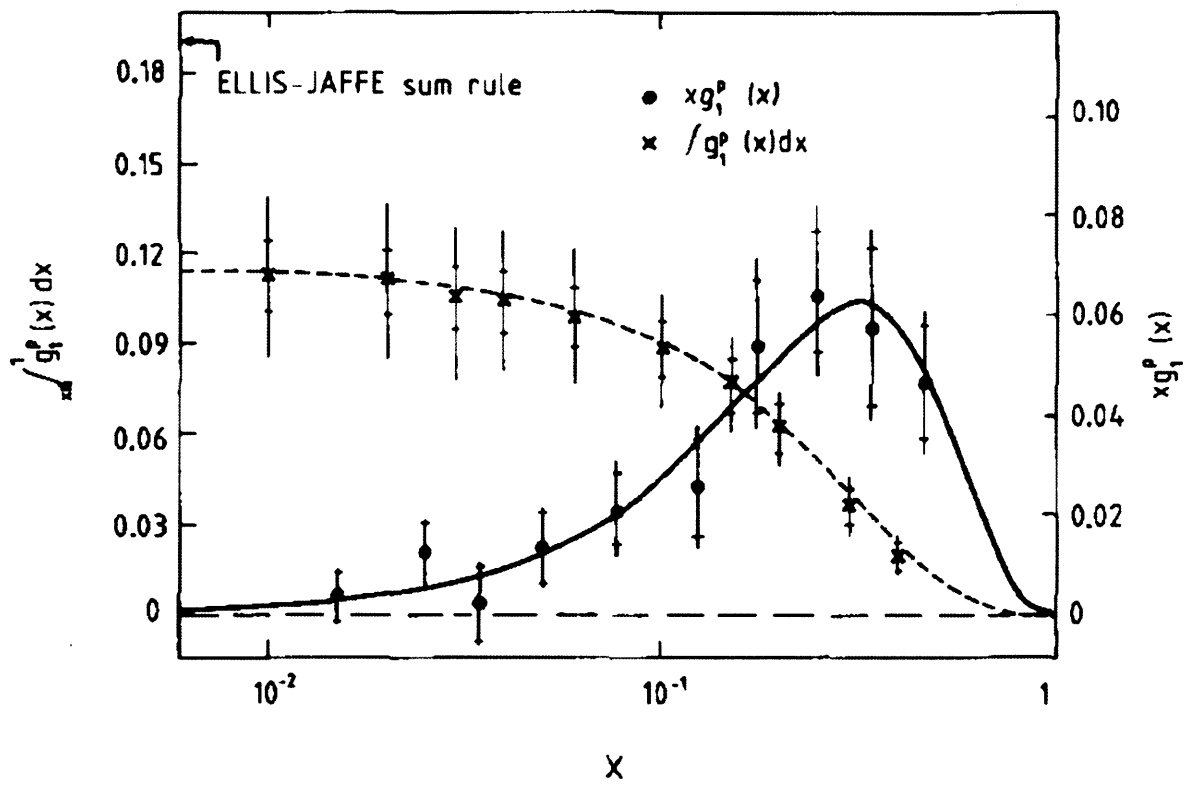

Figure 1-3: Measurements of the first moment of $g_1(x)$ by the EMC experiment are shown by the left axis and the crosses. The data disagree with the Ellis-Jaffe calculation (shown top left) [1].

experimental results suggested that $\Delta\Sigma$ is even smaller and that the role of the gluon was greater than previously believed.

1.3 Quantum Chromodynamics

Quantum chromodynamics (QCD) is a quantum field theory with SU(3) gauge invariance. The QCD Lagrangian is found by imposing local gauge invariance [6]:

$$\mathcal{L} = [i\hbar c\overline{\psi}\gamma^{\mu}\partial_{\mu}\psi - mc^2\overline{\psi}\psi] - \frac{1}{16\pi}F_{\kappa}^{\mu\nu}F_{\mu\nu}^{\kappa} - (q\overline{\psi}\gamma^{\mu}\lambda_{\kappa}\psi)A_{\mu}^{\kappa}, \tag{1.13}$$

where A_{μ}^{κ} are the gluon fields, $F_{\mu\nu}^{\kappa}$ are the color fields, λ^{κ} are the Gell-Mann matrices, and q is the color charge.

In QCD, it's possible to write the angular momentum operator in gauge-invariant form [11]:

$$J_{QCD} = J_q + J_g \tag{1.14}$$

with

$$\begin{aligned} J_q &= \int d^3x[x \times T_q] \\ &= \int d^3x[\psi^{\dagger}\frac{\Sigma}{2}\psi + \psi^{\dagger}x \times (-iD)\psi], \\ J_g &= \int d^3x[x \times (E \times B)]. \end{aligned} \tag{1.15}$$

The angular momentum for the quark and the gluon are generated from their respective momentum densities T_q and $E \times B$. The quark spin term is associated with the Dirac spin matrix Σ, and the quark orbital angular momentum is associated with the covariant derivative $D = \nabla - iqA$. For a proton moving in the z direction, in the positive helicity state, the expectation of J_z is

$$\frac{1}{2} = \frac{1}{2}\Delta\Sigma + L_q + J_g. \tag{1.16}$$

It is tempting to try to separate the contributions of the gluon into the contri-

butions of the spin component and the orbital angular momentum component. It is possible to define a gluon helicity distrubtion $\Delta g(x)$ using infrared factorization in light cone coordinates as [11]

$$\Delta g(x,\mu^2) = \frac{i}{2}\int \frac{d\lambda}{2\pi} e^{i\lambda x}\langle PS|F^{+\alpha}(0)U(0,\lambda n)\widetilde{F}^{+}_{\alpha}(\lambda n)|PS\rangle, \tag{1.17}$$

where $\widetilde{F}_{\alpha\beta} = (1/2)\epsilon_{\alpha\beta\mu\nu}F^{\mu\nu}$. The first moment of $\Delta g(x)$ is in general a non-local operator. In the light cone gauge, the first moment, ΔG becomes a local operator that can be interpreted as the gluon spin density operator. In this gauge, it is possible to write $J_g = \Delta G + L_g$, where L_g is defined as the gluon orbital angular momentum contribution to the proton spin, but there is no way to measure it. Because this separation is possible, there is interest in trying to measure the polarized gluon distribution function $\Delta g(x)$ experimentally.

In polarized proton-proton collisions, the longitudinal double spin asymmetry A_{LL} is sensitive to polarized distribution functions. This asymmetry has the generic structure

$$A_{LL} = \frac{\sum_{f_1,f_2,f} \Delta f_1 \times \Delta f_2 \times \Delta d\hat{\sigma}^{f_1 f_2 \longrightarrow fX} \times D_f}{\sum_{f_1,f_2,f} f_1 \times f_2 \times d\hat{\sigma}^{f_1 f_2 \longrightarrow fX} \times D_f}, \tag{1.18}$$

where $(\Delta)f_i$ are the (polarized) distribution functions for quarks or gluons, $(\Delta)d\hat{\sigma}^{f_1 f_2 \longrightarrow fX}$ is the (polarized) cross section for the process $f_1 f_2 \longrightarrow fX$, and D_f is the fragmentation function for the final state f. Measurements of A_{LL} for different final states provide input to global analyses that can constrain $\Delta g(x)$.

An early extraction of ΔG using DIS data was done prior to RHIC data taking that made the best fit and a calculation for an expected A_{LL} [13]. Though GRSV-std (after the authors) was the best fit value, a variety of other scenarios of ΔG were used to generate A_{LL} curves to compare measurements to. Early STAR measurements [14] excluded large values of ΔG (Fig. 1-4). Along with PHENIX results, this data was incorporated into a newer global extraction by DSSV [2] to provide substantial improvements on the constraints on ΔG. The DSSV extraction suggests a smaller gluon polarization than GRSV std.

The attraction of using dijets for a measurement of the asymmetry is that, to

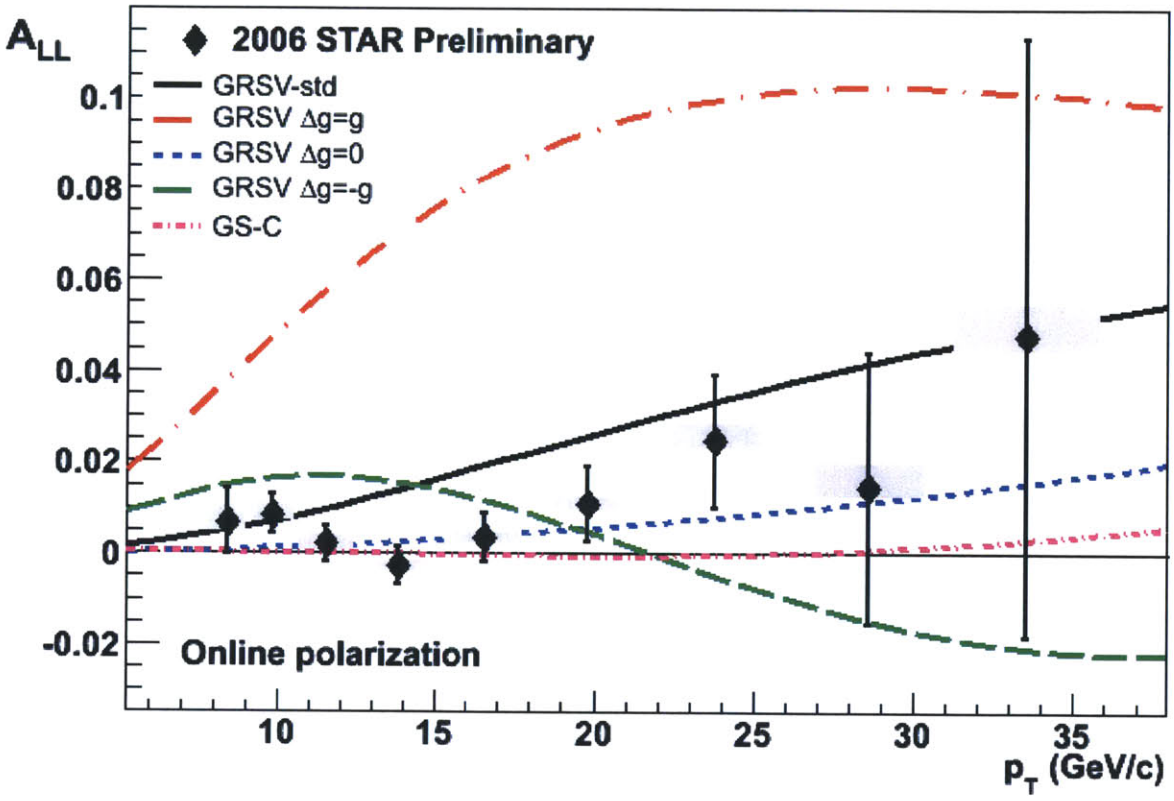

Figure 1-4: An early measurement of A_{LL} using inclusive jets from STAR in 2006 constrained ΔG, in particular excluding large positive values.

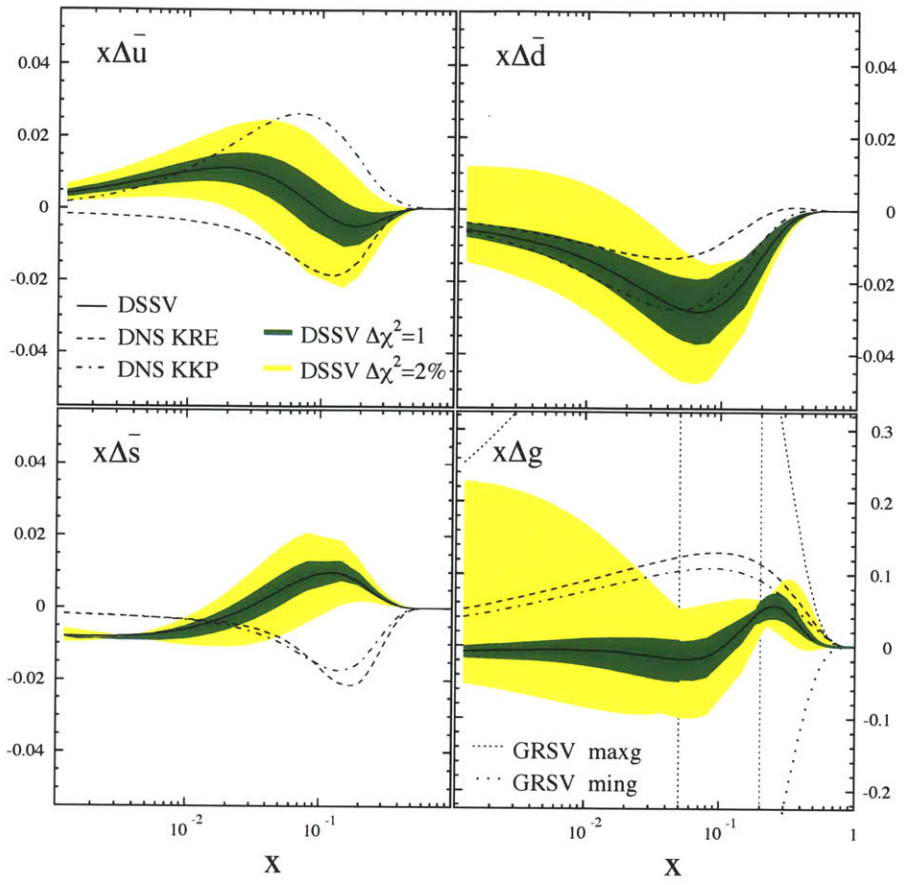

Figure 1-5: STAR data contributed to a significant constraint on a global extraction of $\Delta g(x)$ [2].

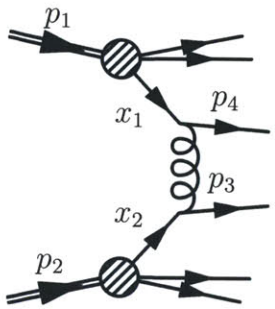

Figure 1-6: This Feynman diagram depicts the collision of two protons, p_1 and p_2. The colliding quarks, x_1 and x_2, have momentum fraction x of their respective protons. Outgoing quarks, p_3 and p_4, can be used to calculated the initial quark kinematics.

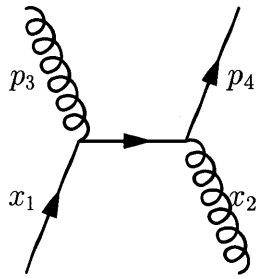

Figure 1-7: A leading-order diagram in QCD for quark-gluon scattering.

leading order, the kinematics of the two jets can be related to the kinematics of the initial partons. Figure 1-6 shows a Feynman diagram illustrating the collision of two protons with momentum p_1 and p_2. In this figure, a quark is selected from each of the protons with momentum fractions x_1 and x_2 according to parton distribution functions. The cross section of the interaction between the two quarks can be calculated in perturbative QCD. The outgoing quarks then fragment into jets, which can be reconstructed in a detector. This fragmentation cannot be described perturbatively; instead some model must be invoked. Effects caused by the interactions of remaining proton fragments (unlabeled) are collectively called underlying event.

Figure 1-7 shows a Feynman diagram for another process called quark-gluon scattering, which is one of the processes sensitive to the gluon polarization. The experiment will attempt to reconstruct p_3 and p_4 of the outgoing jets in order to calculate x_1 and x_2. From conservation of energy and momentum, it is possible to show that

$$\begin{aligned} x_1 &= \frac{1}{\sqrt{s}}(p_{T3}e^{\eta_3} + p_{T4}e^{\eta_4}) \\ x_2 &= \frac{1}{\sqrt{s}}(p_{T3}e^{-\eta_3} + p_{T4}e^{-\eta_4}) \\ M &= \sqrt{x_1 x_2 s} \\ \eta_{34} &= \frac{\eta_3 + \eta_4}{2} = \frac{1}{2}\ln\frac{x_1}{x_2}, \end{aligned} \tag{1.19}$$

where $\sqrt{s}$ is the center of mass energy of the colliding protons and $\eta_{3(4)}$ is the pseudorapidity of the outgoing parton.

Since the dijet measurement provides more complete information about the initial

kinematics than inclusive measurements, this A_{LL} will provide stronger constraints on the shape of $\Delta g(x)$.

Chapter 2

Experimental Setup

Currently, the only polarized proton-proton collider in the world is located in Upton, NY at Brookhaven National Laboratory (BNL). The RHIC is capable of producing polarized proton-proton collisions with $\sqrt{s}$ up to 500 GeV and has demonstrated polarizations of 60%. Heavy ions, including Au and Cu, are also collided at RHIC.

STAR is a large acceptance, multi-purpose detector at RHIC. Its ability to reconstruct charged tracks and electromagnetic energy deposits with full azimuthal coverage over two units in pseudorapidity makes it the only detector at RHIC capable of making jet measurements.

This chapter will provide a background on the systems used in RHIC and STAR that are relevant to the measurement of dijets.

2.1 RHIC

2.1.1 Polarized proton source

The source of polarized protons in RHIC is the optically-pumped, polarized-ion source (OPPIS) that was originally constructed for use at KEK and upgraded at TRIUMF [15]. The source works by optically pumping a Rb vapor with a 4.0W pulsed Ti:sapphire laser. The polarization is transfered to atomic H in spin-exchange polarization collisions. The spin is transferred from the electron to the proton in the

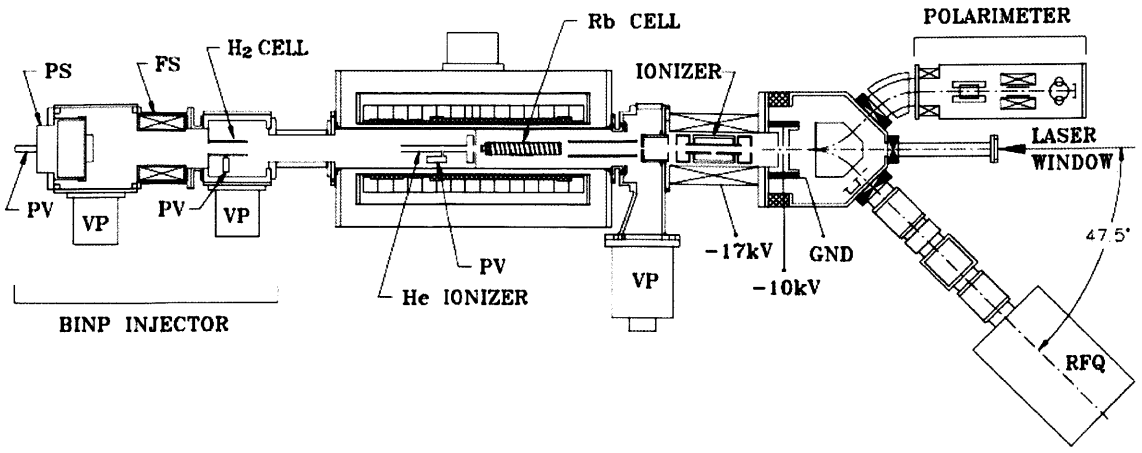

Figure 2-1: A schematic of RHIC's polarized proton source. Protons from the ECR source enter at the left and polarized H^- exits at 35 keV from the lower right [3]

.

H^0 through a Sona transition, which is a method of transferring polarization from an electron to the nucleus using a magnetic field gradient.

Protons are produced using a 28 GHz electron cyclotron resonance (ECR) ion source in a 10 kG field and extracted in a 27 kG field[16]. The gas composition of the ECR source was altered to include portions of water, which helps isolate the plasma from the cavity walls, and oxygen, which helps activate the wall surface for better electron emission to the plasma. These adjustments to the gas mixture allow stable operation for hundreds of hours.

The protons are converted to an atomic H beam by passing through an H_2 cell. The H^0 then enters the Rb cell to be polarized. Polarized H^0 then enter a sodium jet ionizer, where the H^0 take electrons from a sodium vapor, and emerge as H^-, which can be accelerated from approximately 3.0 keV to 35 keV. Figure 2-1 shows a diagram of the system.

The source is capable of providing 0.5 mA with 80% polarization during 300 μs pulses, which corresponds to 9×10^{11} polarized H^-.

2.1.2 Preinjection

The H^- exit the source at 35 keV and travels along a transport line to enter a radio frequency quadrupole (RFQ). The RFQ was designed and built at Lawrence Berkeley National Laboratory and delivered to BNL in 1987 to replace the 750 keV Cockroft-Walton preinjector for the linac [17]. It has four 1.6m vanes fabricated from fully annealed, copper plated mild steel and operates at the linac frequency of 201.25 MHz, accelerating the H^- to 753 keV.

A 6 m transport line carries the H^- from the RFQ to the linac. There are magnetic quadrupoles to maintain transverse matching, and longitudinal bunch structure is maintained using three RF buncher cavities for entry into the linac.

The RHIC proton linac accelerates the H^- to 200 MeV through 9 RF cavities [18]. The linac fires in 500 μs pulses and currents of approximately 37 mA are achieved at the end with a beam spread of 1.2 MeV[19].

After the linac, the H^- are strip injected into the Booster. A single pulse from the linac is captured in a single bunch with a total efficiency from the source of about 50%, amounting to 4×10^{11} protons. Though the booster was originally intended for use as a proton accumulator, the OPPIS provides enough protons that only a single pulse is needed to fill the bunch. This bunch is accelerated to 1.5 GeV and transferred to the Alternating Gradient Synchrotron (AGS).

The AGS accelerates protons in a single bunch up to 24.3 GeV [20]. The 240 magnets of the AGS are connected in series with a total resistance of 0.27 Ω and a total inductance of 0.75 H [21]. The AGS can achieve acceleration cycles at about 1.0 Hz.

Once the protons have been accelerated to injection energy, they are sent to RHIC through the AGS-to-RHIC (ATR) transfer line, which consists of over 770 m of lines, 80 dipoles, 31 quadrupoles, 35 correctors, and 2 Lambertson magnets [22]. The line is divided into four sections (shown in Figure 2-2). The U-line accepts protons from the AGS with matching optics and ends with zero dispersion. The W-line carries the protons dispersion-free using vertical and horizontal bends to a switch for the two

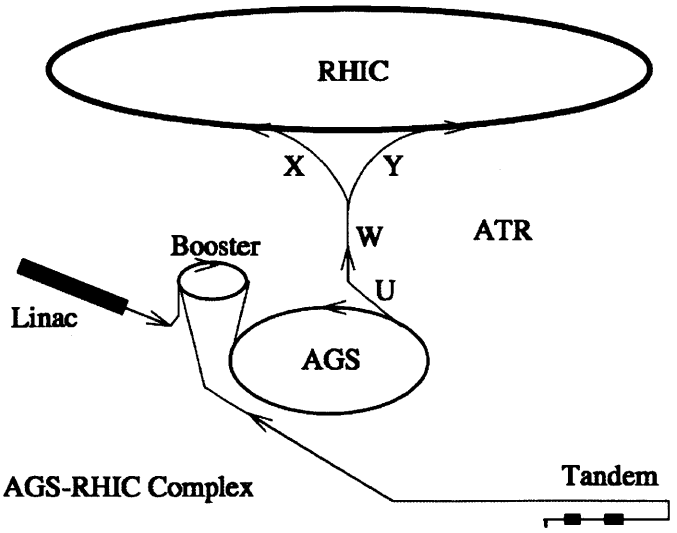

Figure 2-2: A diagram labeling the different sections of the AGS to RHIC transfer line, which are described in the text.

RHIC rings. The X (Y) line bends the beam to the blue (yellow) ring and prepares it for vertical injection.

2.1.3 Storage ring

The RHIC collider consists of two intersecting rings of superconducting magnets with a circumference of 3.8 km. It is capable of accelerating protons to 250 GeV and Au ions to 100 GeV/nucleon, which cover 1 to 2.5 in the ratio of atomic number over charge, A/Z. RHIC operates with up to 120 bunches filled (including abort gaps) in its 360 RF buckets [23]. The acceleration RF system operates at 28 MHz, and the storage system operates at 197 MHz.

The stored beam energy is over 200 kJ per ring for each species, which is sufficient to cause component damage. The abort system can begin safe disposal of the beam within four turns (50 μs) and takes only one turn to dump the entire beam to an internal beam dump.

The main components of the magnet system are 396 dipoles, 492 quadrupoles, 288 sextupoles, and 492 corrector magnets at each quadrupole. The arc dipoles, of which there are 288, have a bending radius of 243 m, a field of 3.5 T, and a current

of 5.1 kA for the top energy.

RHIC circulates supercritical helium to cool the magnets to 4.6 K, within a tolerance of 0.1 K. The entire cold mass of the system is 2.15×10^6 kg with a heat content of 1.74×10^{11} J from 4 to 300 K. The helium is compressed at BNL, requiring approximately 12 MW of electrical power. Another 9 MW is needed for the rings and experiments and 10 MW is needed for the AGS. The beam tube is maintained at $< 10^{-11}$ mbar in the ring and at about 7×10^{-10} mbar in the insertion regions. The interaction points are located in 17.2 m straight sections of beam pipe between two DX magnets, which are common to the two beams and bend them into the interaction regions.

2.1.4 Maintaining and Monitoring Polarization

The spin direction of a beam of polarized protons in an external magnet field is explained by the Thomas-BMT equation [24]:

$$\frac{d\vec{P}}{dt} = -\frac{e}{\gamma m}[G\gamma \vec{B}_{\perp} + (1+G)\vec{B}_{\parallel}] \times \vec{P}, \tag{2.1}$$

where P is the polarization vector, G is the anomalous magnetic moment of the proton, and γ is the boost factor. The spin tune $\nu_{sp} = G\gamma$ is the number of full spin precessions for every revolution.

Accelerating polarized beams encounter depolarizing resonances when the spin precession frequency equals the frequency with which the beam encounters spin perturbing effects. These resonances can be classified into two types: imperfection resonances caused by magnet errors and intrinsic resonances caused by the focusing fields of the accelerator.

The imperfection resonance condition is $\nu_{sp} = n$, where n is an integer, which means imperfection resonances are separated by 523 MeV in proton energy. The intrinsic resonance condition is $\nu_{sp} = kP \pm \nu_y$, where k is an integer, P is the superperiodicity of the accelerator (12 in the AGS and 3 in RHIC), and ν_y is the vertical betatron tune. These resonances can be overcome by applying corrections to the

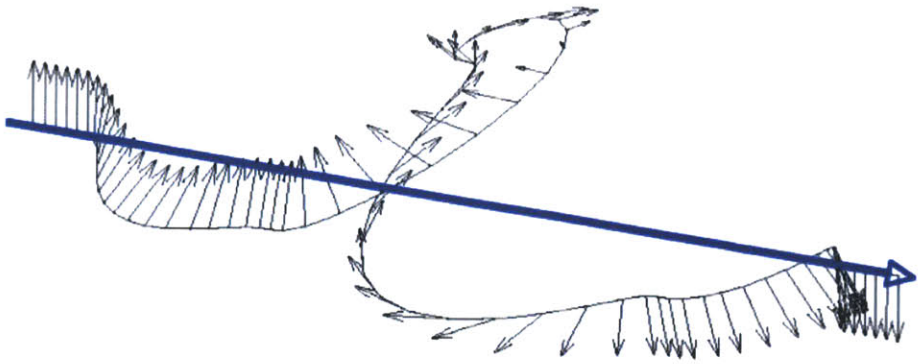

Figure 2-3: The precession of the spin vector for a transversely polarized beam as it traverses a full Siberian Snake along the beam direction (shown in blue).

vertical orbit for imperfection resonances and by using a betatron tune jump for the intrinsic resonances. However, at RHIC, this would call for nearly 200 corrections during the acceleration cycle to 100 GeV.

The development of a Siberian Snake provides an alternative method to maintaining polarization. The Siberian Snake generates a 180° spin rotation as the protons pass through (Fig. 2-3), which means protons encounter depolarizing forces in the opposite direction on each circuit of the ring. This procedure is effective as long as the spin rotation from the Siberian Snake is much larger than the rotation due to resonance fields. In the language of spin tunes, the Siberian Snakes make ν_{sp} always a half integer and energy independent.

The Siberian Snakes are constructed of a set of four superconducting helical dipole magnets producing fields up to 4 T. The Snakes produce the required spin rotation with no net change of the particle trajectory. By controlling the currents in the different helices, it is possible to change the amount of spin rotation and the axis of rotation.

Protons in RHIC are stored with their spins in the transverse direction. To turn the spin to the longitudinal direction, spin rotator magnets are installed at two of the interaction points. These magnets have nearly identical designs to the Siberian Snakes, but are operated with different parameters.

The polarization of the beam is measured using two methods at RHIC. One

method is the measurement of the asymmetry in proton-Carbon elastic scattering in the Coulomb-Nuclear Interference (CNI) region of the beam off a carbon ribbon target. The CNI polarimeters observe very small-angle p+C elastic scattering in each beam using silicon strip detectors [25]. Each polarimeter has three strips that serve as left-right detectors; one horizontal and one each at $\pm 45°$. High statistics can be accumulated relatively quickly using the CNI polarimeter, allowing measurements to be taken multiple times per fill. Generally, physics events are not taken during these short runs because a target is being inserted into the beam. The polarization P_{beam} obtained from the CNI polarimeters is given by

$$P_{beam} = \frac{\varepsilon_{beam}}{A_N}, \tag{2.2}$$

where σ_{beam} is the asymmetry measured by the detector and A_N is the analyzing power of the p+C elastic scattering reaction, which must be determined experimentally [26].

The absolute polarization is measured by Polarized Atomic Hydrogen Jet Target Polarimeter (H-Jet polarimeter) using proton-proton elastic scattering on a transversly polarized proton target [26]. The analyzing power A_N should be the same for the target and beam polarizations because the particles are identical and satisfy the equation:

$$A_N = -\frac{\varepsilon_{target}}{P_{target}} = \frac{\varepsilon_{beam}}{P_{beam}}, \tag{2.3}$$

where ε is the raw asymmetry and P is the polarization. The beam polarization can therefore be measured according to

$$P_{beam} = -P_{target}\frac{\varepsilon_{beam}}{\varepsilon_{target}}, \tag{2.4}$$

so long as the target polarization P_{target} is well calibrated. Because the H-Jet polarimeter uses protons for both the beam and target, many systematic effects cancel in the ratio of raw asymmetries.

The H-Jet polarimeter was installed in March 2004 at IP 12 of the RHIC ring, where the 3000 kg apparatus sits on rails allowing it to move 10 mm in either direction

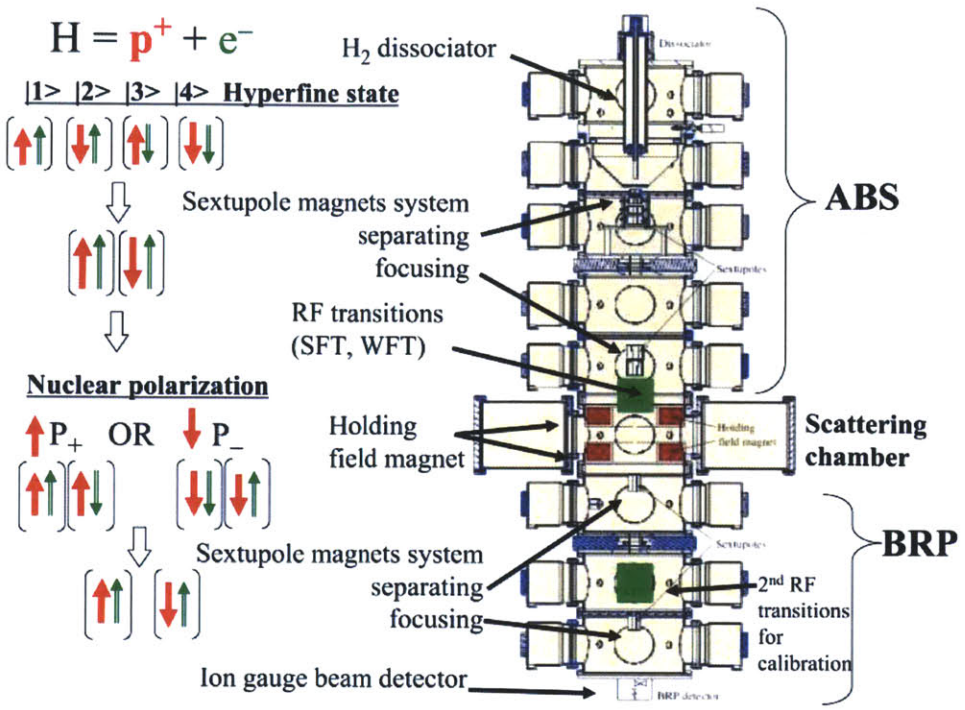

Figure 2-4: A diagram of the H-Jet polarimeter.

along the x-axis (horizontal, perpendicular to the beam axis). The device is made up of three sections, the atomic beam source (ABS), the scattering chamber, and the Breit-Rabi Polarimeter (BRP). A diagram of the polarimeter is included as Fig. 2-4. In the ABS, the polarized atomic beam is produced with a 6.5 mm FWHM. The beam intensity in the scattering chamber was measured to be 1.2×10^{17} atoms/s in the commissioning run in 2004, resulting in a target thickness of 1.3×10^{12} atoms/cm^2. The BRP measured an effective target polarization of 92.4%.

The recoil spectrometer detects the recoil proton from the elastic scattering event using three pairs of silicon strip detectors that cover 15° in azimuth centered on the horizontal plane about 80 cm from the beam. Each detector consists of 16 strips oriented vertically, providing 5.5 mrad coverage in polar angle. The kinetic energy of the recoil is calculated using the time-of-flight relative to the bunch crossing time given by the RHIC clock.

Elastic events are selected by making a cut on the time of flight and kinetic energy

of the recoil proton. By measuring the raw asymmetry for both the beam and target, according to the formula [26]:

$$\varepsilon = \frac{\sqrt{N_{\uparrow}^{L} \cdot N_{\downarrow}^{R}} - \sqrt{N_{\uparrow}^{R} \cdot N_{\downarrow}^{L}}}{\sqrt{N_{\uparrow}^{L} \cdot N_{\downarrow}^{R}} + \sqrt{N_{\uparrow}^{R} \cdot N_{\downarrow}^{L}}}, \tag{2.5}$$

with the event yields sorted by spin state (up-down) and detector side (left-right), it is possible to calculate the beam polarization according to Eq. 2.4. This measurement is used to provide the absolute polarization, to which the CNI polarimeters are normalized.

2.2 STAR

Calorimetry provided by the Barrel Electromagnetic Calorimeter (BEMC) and tracking providing by the Time Projection Chamber (TPC) over 2π in azimuth and two units of pseudorapidity form the core of STAR's ability to reconstruct jets over a large acceptance. The BEMC is also used for the trigger at level 0 and level 2 along with the Beam-Beam Counters (BBCs). The BBCs also record the relative luminosity, which is vital to the measurement of asymmetries in STAR.

2.2.1 BEMC

The BEMC [27] is a lead-scintillator sampling calorimeter covering 2π in azimuthal angle ϕ and $|\eta| < 1$ in pseudorapidity. It is divided into 4800 towers, each covering 0.05 by 0.05 in $\eta - \phi$ space. The towers in turn are grouped into 120 modules that each cover 0.1 in azimuth and one unit of pseudorapidity (2 by 20 towers). The BEMC surrounds the TPC, starting at a radius of approximately 225 cm and extending approximately 30 cm where it terminates upon reaching the STAR solenoid.

Each module of 40 towers is constructed of 21 mega-tiles of scintillator, interleaved with 20 plates of lead absorber. A cross section of a tower showing the layout can be seen in Fig. 2-6. The mega-tiles are each divided into 40 optically isolated tiles

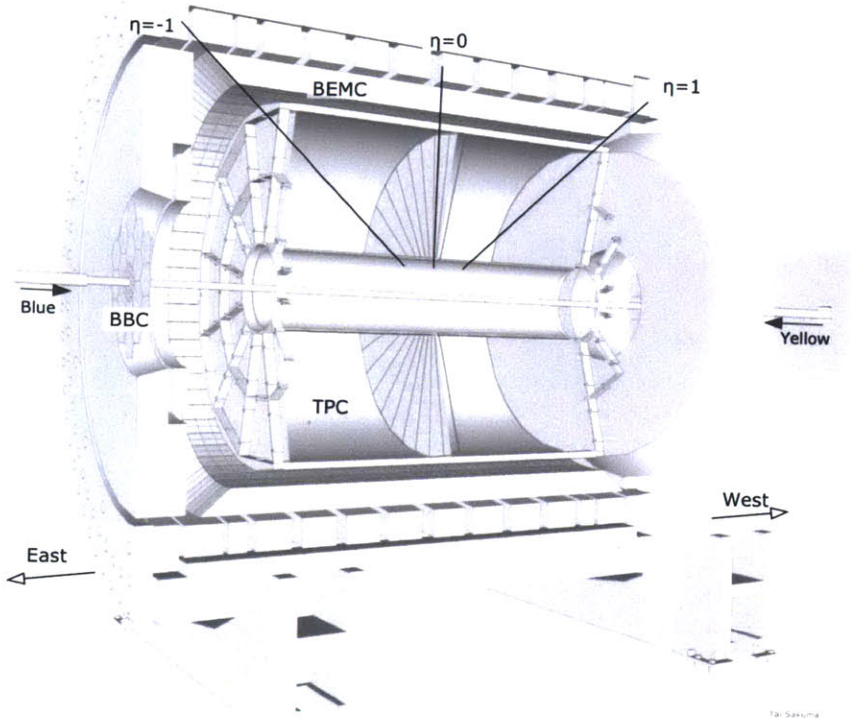

Figure 2-5: A diagram of the STAR detector with the primary detectors used for the jet analysis labeled.

corresponding to the towers of that module using a groove machined into each layer and filled with an opaque silicon dioxide epoxy. A black line painted on the uncut scintillator reduces optical cross talk to less than 0.5 %. The two front scintillator layers are 6 mm thick; the remaining scintillator and lead layers are 5 mm thick. This extra thickness is needed because these two layers are used for a pre-shower detector and have a double readout. The scintillator layers are read out using a wavelength shifting fiber embedded into a σ groove in each tile.

The fibers for each tower terminate in a multi-fiber optical connector at the back of the module and the light is carried out through a 2.1 m long multi-fiber optical cable where the light from the 21 scintillator tiles is combined onto a photomultiplier tube (PMT) through a Lucite light mixer.

The PMTs are Electron Tube Inc. model 9125B with 11 dynodes and mean quantum efficiency of 13.3% with a standard deviation of 1.3%. Quality assurance tests performed on the PMTs after delivery verified that all PMTs had a quantum

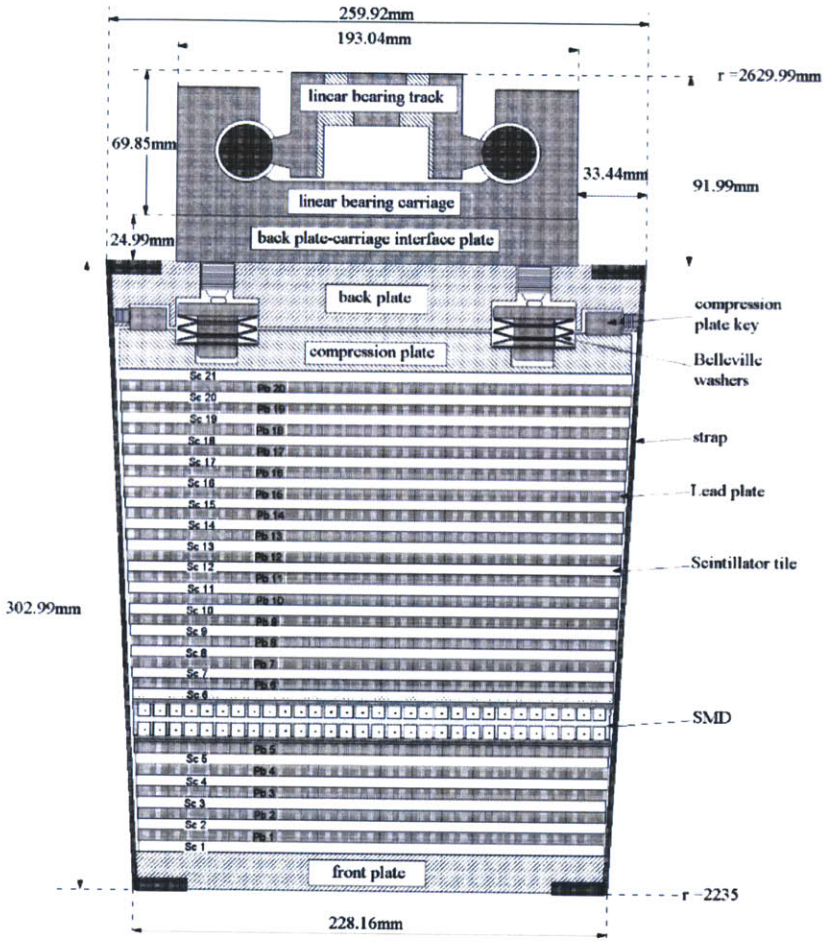

Figure 2-6: A cross section of a BEMC module showing the mechanical assembly of a tower including the compression components and the location of the shower maximum detector.

efficiency greater than 10% at 490 nm, a dark current of less than 5 nA, and a non-linearity of less than 2%.

The calorimeter modules are 26 cm wide and 293 cm long. Each of the towers is projective relative to the origin of the STAR coordinate system. A combination of straps and a compression plate exert a pressure of approximately 15 psi, which is sufficient to hold a module together through friction in any orientation. The modules are positioned on a rail mounting system.

Tests of the BEMC show that an average of 3 photo-electrons per minimum ionizing particle are produced, which results in a resolution of $14\%/\sqrt{E}$ with a 1.5% constant added in quadrature. The test also show that the transverse uniformity of the light from each tile is better than 5% RMS, the longitudinal uniformity is better than 10% RMS within each tower, and the total optical cross talk is less than 0.5% between adjacent tiles. The BEMC absolute scale for electromagnetic energy reconstruction has subsequently been determined to better than 2%. This calibration is discussed in App. A.

In addition to the BEMC towers, there is a Barrel Preshower Detector (BPRS) and a Barrel Shower Maximum Detector (BSMD). The BPRS consists of the first two scintillator tiles of the BEMC towers. The BSMD is a wire proportional counter with a strip readout using gas amplification that sits behind the fifth lead layer at a depth of approximately 5 radiation lengths. Neither detector is used in the analysis discussed in this work.

A significant fraction of STAR's triggering capability is provided by the BEMC. In this analysis, the Level 0 (L0) Barrel Jet Patch (BJP) triggers and the Level 2 (L2) Jet (L2J) triggers are used. The L0 BJP trigger sums over BEMC towers in a fixed region covering one unit of pseudorapidity and one unit of azimuthal angle, which is made up of 400 towers. There are six jet patches on the east half of the BEMC and six more on the west half. The summed energy in a single jet patch must be above a predetermined threshold for the event to pass the trigger. Generally, there are multiple BJP triggers with different prescales and thresholds. The L2J trigger is fed by the events that pass an L0 BJP trigger, and it also sums over groups of 400

towers, but by using a scanning technique that allows the center of the block to move. The L2J trigger has thresholds for both single jet and dijet events. There is also a percentage of events that are allowed to randomly pass the trigger.

The L0 trigger decisions are calculated on a set of FPGAs called Data Storage and Manipulator boards (DSMs) that have their own independent data acquisition pipelines, as well as pedestals and status tables. The L2 trigger decisions are calculated on a dedicated CPU.

2.2.2 TPC

The STAR Time Projection Chamber (TPC) is the primary tracking device used by STAR analyses [28]. The acceptance covers the full range in azimuthal angle and ± 1.3 units of pseudorapidity from the STAR origin. The TPC is able to reconstruct 3000 tracks in a single event, measuring their momenta from 100 MeV/c to 30 GeV/c. Particle identification is possible through measurements of dE/dx.

The TPC is a 4.2 m long, 4 m diameter cylindrical gas volume (see Fig. 2-7). To make momentum measurements possible, it sits in a solenoidal magnet with a 0.5 T field along the z-axis of the TPC, which coincides with the beam axis. A conductive membrane at the center of the TPC is kept at 28 kV, which results in an electric field of approximately 135 V/cm that causes ionization electrons to drift to readouts at each end. Field uniformity is maintained by a series of 182 rings biased by resistor chains. The TPC is filled with P10 gas (10% methane, 90% argon) kept at 2 mbar above atmospheric pressure. The drift velocity is approximately 5.5 cm / μs, which is calibrated in situ using a laser calibration system that generates electrons from aluminum strips on the central membrane.

The readout system at the ends consists of three wire planes and a pad plane. The first wire plane is a gating grid, which is used to maintain the uniform drift field and minimize the amount of pile-up clusters read out. The next two wire planes form the amplification region, which has a gain of approximately 1000 in the outer sectors and 4000 in the inner sectors. The pad plane behind the amplification measures induced charge in over 135,000 pads, which are used to reconstruct hits. The x-y position of

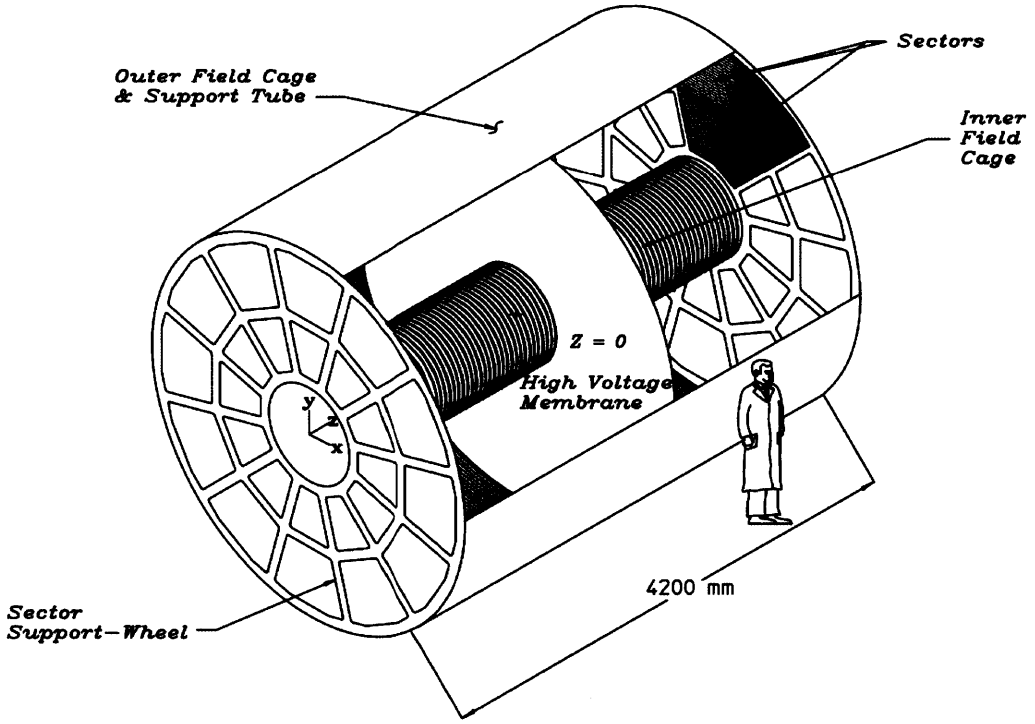

Figure 2-7: The STAR TPC provides large acceptance tracking of charged particles, vertex reconstruction, and particle identification.

a hit is found by calculating the energy weighted center of a cluster of three pads, and the z position is found by measuring the amount of time it took for the cluster to drift in the TPC.

Tracks are reconstructed by fitting the hits to a helix, from which the momentum can be extracted. The momentum resolution is approximately 2%. Vertices are reconstructed by extrapolating tracks back to the beamline with a resolution of approximately 1 mm in proton-proton collisions.

2.2.3 BBC

The Beam-Beam Counters (BBC) are detectors consisting of rings of scintillator tiles positioned around the beam pipe on both ends of STAR [29]. They provide full azimuthal coverage and cover the pseudorapidity range $3.4 < |\eta| < 5.0$ as seen in Fig. 2-8. A coincidence requirement on hits in the East and West BBCs defines the minimum bias trigger in proton-proton collisions. The timing resolution of the BBCs is approximately 2 ns and the coincidence trigger uses an 8 ns timing window.

The BBCs also serve as a luminosity monitor for both the absolute luminosity and the relative luminosity between collisions of different spin states. To be able to record data at the high rates required to perform this function accurately, a fast scaler board system is used for BBC data acquisition. The VME memory module allows the scaler board to record 40 bits at 10 MHz for 24 hours. The bunch crossing and spin information is stored in 7 bits, and the remaining 17 bits describe the detector information being recorded in the 40 bits of data.

2.2.4 ZDC

The Zero Degree Calorimeter (ZDC) is a hadronic calorimeter positioned in the RHIC tunnel on either side of the detector past the magnets which turn the beam in and out of the interaction region beam pipe [30]. Its position can be seen in Fig. 2-9. The ZDC therefore measures neutral hadrons that are remnants from collisions. It was designed for use in collisions of heavy nuclei, with the need to measure the single

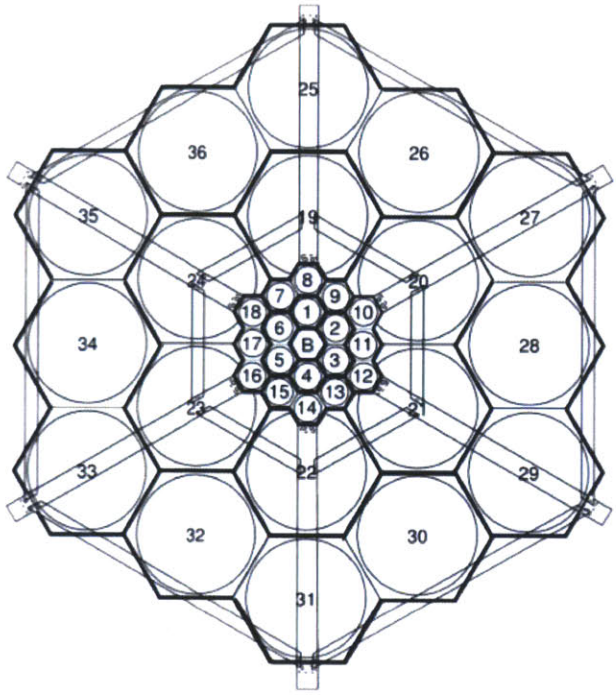

Figure 2-8: The STAR BBC. The inner 18 tiles are used for this analysis. The "B" represents the beam pipe.

neutron peak from peripheral collisions being the paramount concern.

Because the ZDC rate is much lower than the BBC, it serves as a more stable absolute luminosity monitor. The ZDC is also included in the scaler system and is used as a cross check for the relative luminosity. The ZDC Shower Maximum Detector (SMD) provides transverse resolution in the ZDC using the segmentation of the scintillator strips and is used as a local polarimetry monitor and to measure the transverse polarization component.

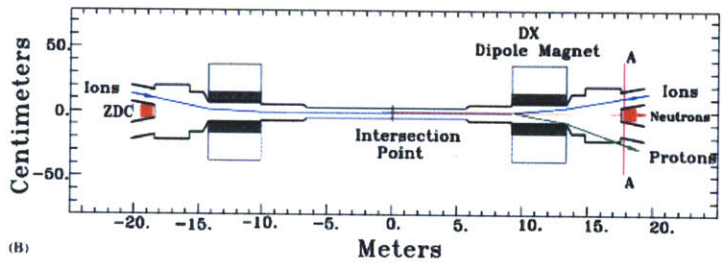

Figure 2-9: The ZDC is positioned past the DX bending magnets so that only neutral particles enter it.

Chapter 3

Jets

A jet is the name physicists have given to the spray of particles produced by the fragmentation and hadronization of quarks and gluons, an effect of the requirement in QCD that stable particles be color singlets. In hadron colliders, the jet cross section is the dominant interaction, which makes jets very effective probes of the QCD processes that are sensitive to gluon polarization. Measurements using jets face two major challenges. First, the effects of non-perturbative processes make the connection between partons and particles ambiguous. Second, because jets are made up of multiple particles, measurement of jets is complicated by detector smearing, escaping particles, and underlying event effects.

3.1 Different Levels of Jets

When studying jets, there are three relevant environments to discuss in relation to jets. Theory calculations typically deal with jets at the perturbative scale, where jets are made up of partons. The calculations represent an understanding of QCD and its predictions. Detectors are designed to measure the results of particle collisions. Jets from a detector are made up of detector quantities like tracks and energy depositions. Monte Carlo simulation packages can simulate jets at both of these levels and at an intermediate level, after fragmentation and hadronization of partons, but before detector effects have been applied. At this level, jets are made up of particles that

would be stable within the dimensions of the detector.

The theoretical calculations dealt with in this analysis extend only to next to leading order (NLO), which contain $\mathcal{O}(\alpha_s)$ corrections to the LO or tree level diagrams. They did not include the effects of any of the long-range processes such as fragmentation and hadronization nor any effects due to the fact that the initial state partons were actually constituents of larger hadrons.

In contrast, the Monte Carlo simulation packages used in this analysis contain only LO calculations of the cross sections for hard interactions. They also contain models for the long-range processes that govern fragmentation, hadronization and interactions between partons within a hadron. For this reason, the partons in NLO calculations and those in LO Monte Carlo generators must be compared with caution. Monte Carlo simulations also include detector simulation. When the detector behavior in simulation is validated against the real behavior in data, analyses in a full simulation can be compared to actual data.

Jet measurements generally aim to provide results at the particle level. The rationale is that the effect of detectors on the observable has been removed, so similar measurements from different experiments can be compared. At the same time, effects that arise from physical processes that are not understood fundamentally, such as fragmentation and hadronization, are not included as corrections. Theoretical calculations are done at the parton level and have corrections for these long-range effects applied. Thus, the results of Monte Carlo simulations are used to bridge the gap between the NLO theoretical calculations and actual jet measurements by correcting both to the particle level.

3.2 Theoretical Background

The need to be able to define jets in the different environments described above motivates the study of different jet definitions and their effects on different analyses [31]. This issue was first tackled in 1990 by a group of theorists and experimentalists who came up with the Snowmass accord [32]. The properties that they came up with

for jet definitions are:

1. Simple to implement in an experimental analysis;

2. Simple to implement in the theoretical calculation;

3. Defined at any order of perturbation theory;

4. Yields finite cross sections at any order of perturbation theory;

5. Yields a cross section that is relatively insensitive to hadronization.

There are two major classes of jet finding algorithms. The first class consists of cone algorithms. These algorithms sum up the energy in a cone of fixed radius, with the idea fragmentation and hadronization have minimal effects on the energy distribution in an event. Variations on this algorithm suggest different ways to decide where to put the cones and what to do when cones overlap.

One major concern about the use of cone algorithms is the violation of infrared and collinear safety, which prevent items 4 and 5 of the Snowmass accord from being satisfied. Collinear unsafety means that if there is a collinear splitting, the number of final state jets is modified. Infrared unsafety enters if the emission of a soft gluon causes the final number of jets to change. Changes like using split-merge to separate overlapping cones and adding midpoint seeds help delay the unsafeties to higher orders in perturbative calculations.

The other class of algorithms is made up of sequential recombination jet algorithms. These algorithms combine particles in sequence according to some distance measure that varies for each algorithm. The algorithms mostly begin by combining the pair of particles with the lowest of the distance measures and repeating until all pairs are above some threshold. These algorithms are generally infrared and collinear safe.

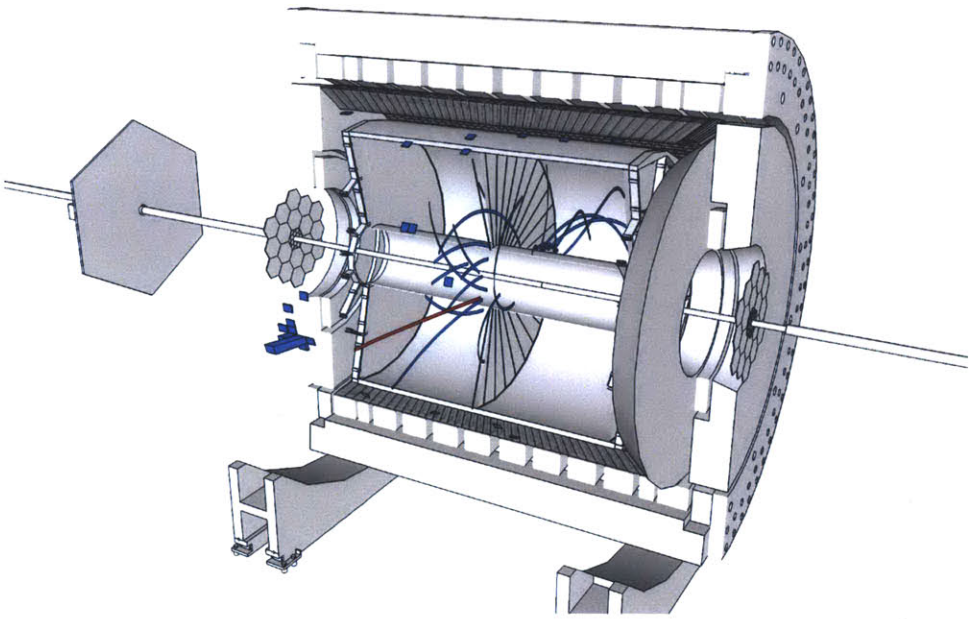

Figure 3-1: An event display of a dijet event taken during Run 9, displaying tracks reconstructed in the TPC and energy depositions measured in the BEMC.

3.3 Jet Finding in STAR

STAR used a midpoint cone jet finding algorithm with split-merge that was developed at CDF [33]. This algorithm is a member of a class of algorithms that iterate over all of the particles within a circle of radius R from seed particles. In STAR, the threshold to be used as a seed was 500 MeV. Additional particles were added if they were above the association threshold, which is 100 MeV for STAR, and they were within $r = \sqrt{\Delta\eta^2 + \Delta\phi^2} < R$ from the energy weighted center of the jet, where R was the cone radius. In STAR, R = 0.4 or 0.7 depending on the acceptance of the BEMC for the relevant data period. Particles were added and removed from jets iteratively until the jets stabilize.

The midpoint approach added additional seeds at the midpoints between stable jets after a phase of jet finding. Stable jets were then found around each midpoint seed. This additional step added some additional measure of infrared safety (in fact, up to one more order in a perturbative calculation) to the algorithm.

Determining whether overlapping jets should be split or merged was the final step

in the algorithm. If the energy in the overlap region was greater than the split-merge fraction of the smaller jet, the two jets were merged. In STAR, this fraction was set to 0.5. Otherwise, the two jets were split and particles were assigned to the nearest jet. Jet directions were recalculated once at the end of the step.

Jet finding on a list of particles was straightforward, but some additional considerations were made when jet finding on detector level quantities. In particular, quality assurance cuts were applied and corrections were made to the jets. First, events needed to have a vertex with positive rank for jet finding to begin. The vertex finder gave vertices positive rank if they were more likely to be from an actual event, not pile-up.

Then additional constraints were applied to each of the particles used in the jet finding, which were actually tracks in the TPC and energy deposits in the BEMC. The following cuts were applied to BEMC energy deposits:

- Tower status is good (status == 1)
- Tower energy > 0
- Tower ADC - pedestal > 4 and Tower ADC - pedestal > 3× pedestal RMS

The following cuts were applied to TPC reconstructed tracks:

- Number of hits on track > 12
- Radius of last hit > 125 cm
- Track flag >= 0
- 0 < Track χ^2 < 4
- Track DCA to vertex < 3 cm
- Track $|\eta| < 2.5$
- An additional p_T dependent minimum DCA cut

A particle that creates a track in the TPC could also deposit energy in the BEMC. To avoid double counting, a subtraction scheme was applied to the energy of the BEMC particles if a track points to that tower. Up until 2006, the energy of a minimum-ionizing particle (MIP) was subtracted from the tower energy. In 2009, this method was changed to subtract all of the momentum from the TPC track from the tower energy. In both cases, the particle was removed from the BEMC list if the subtracted energy becomes negative.

After the lists of particles from each detector were finalized, they were converted to four-vectors. The four-vectors from the BEMC were determined by the location of the tower, the energy measured in the tower, and an assumption that the particle was a photon. For the TPC, the four-vectors were determined by the three dimensional momentum vector and assumption the particle was a charged pion.

It was from this list of four-vectors that the jet finding algorithm generated lists of jets.

An example PYTHIA record is shown in Table 3.1. In this record, the particles used for partonic jets are highlighted in gray. The particles used for particle jets are highlighted in blue.

Table 3.1: Example PYTHIA Record

I	particle/jet	KS	KF	orig	p_x	p_y	p_z	E	m
1	!p^+!	21	2212	0	0.00000	0.00000	99.99560	100.00000	0.93827
2	!p^+!	21	2212	0	0.00000	0.00000	-99.99560	100.00000	0.93827
3	!d!	21	1	1	-1.50864	2.02009	14.58474	14.80107	0.00000
4	!u!	21	2	2	1.21466	-0.41314	-61.19402	61.20747	0.00000
5	!d!	21	1	3	1.21078	3.64702	13.22794	13.77481	0.00000
6	!u!	21	2	4	1.17036	-0.39807	-58.96224	58.97520	0.00000
7	!d!	21	1	0	2.14311	25.04747	-44.25474	50.89754	0.33000
8	!u!	21	2	0	0.23803	-21.79852	-1.47956	21.85246	0.33000
9	($\overline{u}$) A	12	-2	2	0.20749	-0.41704	-9.89322	9.90967	0.33000
10	(g) I	12	21	3	0.36618	-0.09492	-0.45126	0.58884	0.00000
11	(g) I	12	21	1	0.11885	-1.33513	-0.43094	1.40798	0.00000
12	(g) I	12	21	3	-0.07175	-0.30424	0.21467	0.37920	0.00000
13	(g) I	12	21	3	-2.55621	-3.37858	-0.75372	4.30315	0.00000
14	(g) I	12	21	8	-0.18864	-0.52791	0.22296	0.60332	0.00000
15	(g) I	12	21	8	0.28015	-2.37289	0.04581	2.38981	0.00000
16	(u) V	11	2	8	-0.26682	-16.76198	-1.63300	16.84668	0.33000
17	(d) A	12	1	1	-0.00064	-0.68987	38.29117	38.29880	0.33000
18	(uu_1) V	11	2203	1	-0.17363	-0.56039	33.51318	33.51831	0.00000
19	($\overline{d}$) A	12	-1	1	0.26921	-0.02301	8.29558	8.29998	0.00000
20	(g) I	12	21	1	0.23627	0.02580	2.43265	2.44423	0.00000
21	(g) I	12	21	1	0.29594	0.47155	0.36986	0.66838	0.00000
22	(g) I	12	21	1	0.42829	0.09688	-0.09720	0.44974	0.00000
23	(g) I	12	21	2	0.21751	0.37795	-0.31508	0.53799	0.00000

I	particle/jet	KS	KF	orig	p_x	p_y	p_z	E	m
24	(g) I	12	21	1	-0.41180	0.56904	-0.03519	0.70330	0.00000
25	(g) I	12	21	1	-0.62070	-0.20756	-1.17007	1.34067	0.00000
26	(g) I	12	21	2	-0.11687	-0.82769	-0.22985	0.86692	0.00000
27	(u) V	11	2	2	-0.68972	-0.24080	0.12012	0.81057	0.33000
28	(u) A	12	2	2	-0.08989	0.26247	-0.45758	0.53512	0.00000
29	(ud_0) V	11	2101	2	-0.02135	0.19076	-21.71191	21.71275	0.00000
30	($\overline{u}$) A	12	-2	2	0.08579	0.58229	-0.89200	1.11847	0.33000
31	(g) I	12	21	2	0.53059	0.10127	-0.82883	0.98931	0.00000
32	(g) I	12	21	2	0.02229	0.08316	-0.47646	0.48418	0.00000
33	(g) I	12	21	7	-0.10704	2.83568	-4.26654	5.12405	0.00000
34	(g) I	12	21	7	0.57982	10.20918	-18.26852	20.93567	0.00000
35	(d) V	11	1	7	1.67669	11.93599	-21.59463	24.73290	0.33000
36	(cluster)	11	91	17	-0.17428	-1.25027	71.80434	71.81711	0.49049
37	(Δ^+)	11	2214	36	0.06202	-1.25703	77.66993	77.68881	1.16200
38	($\overline{d}$) A	12	-1	19	0.10191	-0.00871	3.14037	3.14203	0.00000
39	(g) I	12	21	20	0.16728	0.01826	1.72228	1.73048	0.00000
40	(g) I	12	21	21	0.29594	0.47155	0.36986	0.66838	0.00000
41	(g) I	12	21	22	0.42829	0.09688	-0.09720	0.44974	0.00000
42	(g) I	12	21	23	0.21751	0.37795	-0.31508	0.53799	0.00000
43	(g) I	12	21	24	-0.41180	0.56904	-0.03519	0.70330	0.00000
44	(g) I	12	21	25	-0.62070	-0.20756	-1.17007	1.34067	0.00000
45	(g) I	12	21	26	-0.11687	-0.82769	-0.22985	0.86692	0.00000
46	(u) V	11	2	27	-0.68972	-0.24080	0.12012	0.81057	0.33000
47	(cluster)	11	91	28	-0.11124	0.45324	-22.16948	22.24787	1.80665
48	π^+	1	211	47	-0.16393	-0.17901	-0.78648	0.83483	0.13957
49	n^0	1	2112	47	0.05269	0.63225	-21.38300	21.41304	0.93957
50	(string)	11	92	9	-2.11076	-25.19269	-12.67870	36.42865	22.96019
51	(ω)	11	223	50	0.24656	-0.45914	-5.57125	5.65066	0.78706
52	(K^{*-})	11	-323	50	-0.08679	-0.37067	-2.66543	2.78997	0.73107
53	K^+	1	321	50	0.14875	0.06541	-0.61606	0.80597	0.49360
54	π^0	1	111	50	0.09596	-0.17276	-1.48582	1.50497	0.13498
55	(ω)	11	223	50	0.03157	-0.95306	0.03391	1.23591	0.78549
56	π^0	1	111	50	-0.96288	-1.53775	-0.68966	1.94568	0.13498
57	η	1	221	50	-0.46707	-1.41130	0.10811	1.58786	0.54745
58	(ω)	11	223	50	-0.22527	-1.05754	-0.20267	1.34952	0.78166
59	(ω)	11	223	50	-0.84173	-4.39253	-0.23531	4.55579	0.83489
60	π^0	1	111	50	0.26116	-3.96823	-0.41778	4.00098	0.13498
61	π^-	1	-211	50	-0.41748	-6.35512	-0.34159	6.37950	0.13957
62	π^+	1	211	50	0.10646	-4.58000	-0.59514	4.62184	0.13957
63	(string)	11	92	30	2.78814	25.74756	-46.32698	53.38458	5.74575
64	(ρ^-)	11	-213	63	0.01695	1.34942	-1.99058	2.52540	0.77072
65	($\overline{K}^0$)	11	-311	63	0.22333	0.76224	-2.90694	3.05432	0.49767
66	(K^0)	11	311	63	1.01369	8.41128	-14.36303	16.68297	0.49767
67	π^+	1	211	63	0.38912	2.96072	-4.52249	5.42122	0.13957
68	(ρ^-)	11	-213	63	1.14506	12.26391	-22.54395	25.70068	0.76197
69	n^0	1	2112	37	0.01537	-0.80611	55.26575	55.27962	0.93957
70	π^+	1	211	37	0.04665	-0.45092	22.40417	22.40919	0.13957
71	(string)	11	92	38	-0.62815	0.24892	3.50523	10.25008	9.60838
72	(ρ^0)	11	113	71	0.34033	0.12881	2.48261	2.62114	0.75800
73	(ω)	11	223	71	0.35160	0.52124	1.95581	2.20075	0.78918
74	(ρ^+)	11	213	71	0.05148	0.08388	0.36898	0.91642	0.83306
75	(ω)	11	223	71	-0.13377	-0.32913	0.04755	0.85295	0.77398
76	π^0	1	111	71	-0.06705	0.91581	-0.46649	1.03877	0.13498
77	π^-	1	-211	71	0.05585	-0.40653	-0.33059	0.54512	0.13957
78	(ω)	11	223	71	-0.69611	-0.09420	-0.70094	1.26941	0.79160
79	π^+	1	211	71	-0.53048	-0.57097	0.14829	0.80553	0.13957
80	γ	1	22	51	-0.20556	-0.39013	-2.02280	2.07031	0.00000
81	π^0	1	111	51	0.45211	-0.06901	-3.54845	3.58035	0.13498
82	($\overline{K}^0$)	11	-311	52	-0.13559	-0.31569	-1.55620	1.66957	0.49767
83	π^-	1	-211	52	0.04881	-0.05498	-1.10923	1.12040	0.13957

I	particle/jet	KS	KF	orig	p_x	p_y	p_z	E	m
84	π^-	1	-211	55	0.18758	-0.09124	0.04573	0.25511	0.13957
85	π^+	1	211	55	0.09324	-0.45406	-0.00161	0.48410	0.13957
86	π^0	1	111	55	-0.24924	-0.40776	-0.01021	0.49670	0.13498
87	π^-	1	-211	58	-0.26469	-0.19415	-0.10741	0.37252	0.13957
88	π^+	1	211	58	-0.10285	-0.38015	0.08276	0.42593	0.13957
89	π^0	1	111	58	0.14227	-0.48325	-0.17802	0.55107	0.13498
90	π^+	1	211	59	-0.41069	-2.87813	-0.11288	2.91282	0.13957
91	π^-	1	-211	59	-0.38220	-0.97084	-0.21170	1.07374	0.13957
92	π^0	1	111	59	-0.04884	-0.54356	0.08927	0.56924	0.13498
93	π^-	1	-211	64	0.25094	0.37062	-1.01144	1.11482	0.13957
94	π^0	1	111	64	-0.23399	0.97880	-0.97914	1.41058	0.13498
95	K_s^0	1	310	65	0.22333	0.76224	-2.90694	3.05432	0.49767
96	K_s^0	1	310	66	1.01369	8.41128	-14.36303	16.68297	0.49767
97	π^-	1	-211	68	0.28156	6.81462	-12.45541	14.20123	0.13957
98	π^0	1	111	68	0.86350	5.44929	-10.08854	11.49944	0.13498
99	π^-	1	-211	72	0.46571	-0.04242	2.13818	2.19317	0.13957
100	π^+	1	211	72	-0.12539	0.17123	0.34443	0.42797	0.13957
101	π^+	1	211	73	-0.11632	-0.02606	0.42091	0.45919	0.13957
102	π^-	1	-211	73	0.31290	0.15346	0.78005	0.86569	0.13957
103	π^0	1	111	73	0.15501	0.39384	0.75485	0.87588	0.13498
104	π^+	1	211	74	-0.02546	0.42675	0.12119	0.46575	0.13957
105	π^0	1	111	74	0.07694	-0.34286	0.24779	0.45066	0.13498
106	π^+	1	211	75	-0.14094	0.07327	-0.01496	0.21198	0.13957
107	π^-	1	-211	75	-0.02386	-0.38512	-0.10439	0.42340	0.13957
108	π^0	1	111	75	0.03103	-0.01728	0.16691	0.21757	0.13498
109	π^+	1	211	78	-0.38065	0.10279	-0.40252	0.58048	0.13957
110	π^-	1	-211	78	-0.35709	-0.13767	-0.06916	0.41319	0.13957
111	π^0	1	111	78	0.04163	-0.05932	-0.22925	0.27573	0.13498
112	K_L^0	1	130	82	-0.13559	-0.31569	-1.55620	1.66957	0.49767

Chapter 4

Simulation

The previous chapter motivates the need to consider jets at three different stages in their formation. To calculate the effects of the transitions between these three stages, it was necessary to simulate proton-proton collisions in a model of the STAR detector. The event generator used for this work was PYTHIA, which uses leading order (LO) calculations [34]. The STAR detector and material interactions were simulated using a software package based on GEANT3 [35], developed by STAR called STARSIM [36].

4.1 Event Generation

High-energy collisions provide a wonderful testing ground for the calculations of perturbative Quantum Chromodynamics. Interactions between particles can be explained at a very simple level using Feynman diagrams like the one shown in Fig. 1-7. As calculations extend to higher orders, the number and complexity of diagrams increase. What an event generator does is separate the complicated problem of colliding two particles and producing outgoing, final state particles into simpler components. Event generators, PYTHIA in particular, use Monte Carlo methods to sample from the distributions of relevant variables to provide realistic output. Though they are an extremely powerful tool, event generators need to be validated against data to check for bugs in the software or for actual physics disagreements.

4.1.1 PYTHIA

The event generator known as PYTHIA has its origins in attempts to explain hadronization in e^+e^- collisions at PETRA in the late seventies. Development of the Lund string model [37] led to the creation of an event generator called JETSET [38]. Later, a parton shower description was added to JETSET to improve simulation of multi-jet events.

As interest in hadron colliders increased, the need to be able to model initial state interactions increased, along with a need for understanding underlying event and minimum bias events. Underlying event is the term given for the effects of interactions between the constituents of the hadrons other than those that take part in the hard interaction. The number of subprocesses in hadron collisions is also substantially higher than in e^+e^- collisions. These needs motivated the development of PYTHIA.

JETSET and PYTHIA were formally merged in PYTHIA version 6.1. Later versions include additional models of beyond the Standard Model physics. PYTHIA version 6.4 was used in this work.

In the PYTHIA methodology, two partons are selected from the initial protons by sampling experimentally measured parton distribution functions. The matrix elements for the hard interaction are calculated to LO using pQCD, meaning there are two input partons and two output partons. PYTHIA then relies on the string fragmentation model to describe fragmentation and hadronization. The use of the parton distributions and the fragmentation model represent PYTHIA's way of modeling the modifications of the LO hard cross section by soft processes and higher order corrections.

4.1.2 Tuning PYTHIA

The procedure for finding the optimal combination of parameter values used in the PYTHIA event generation is called tuning. Tuning is primarily needed to correctly model the effects of underlying event and infrared physics, which are not easily described in pQCD. These effects are of considerable importance in hadron collisions.

There are two strategies for tuning event generators to data.

The most widely used tunes from CDF were developed by Rick Field [39] using studies of underlying event data. This method looked for jets in CDF events. The leading jet defined the "toward" region from $-2\pi/3 < \Phi < 2\pi/3$ and the "away" region was defined opposite to that region. The remaining space between the toward and away regions was defined as the "transverse" region. Measurements of charged particle multiplicities, p_T distributions, E_T distributions and others were compared from CDF Run 2 data and PYTHIA simulations. The tune that best described the data was CDF Tune A, which has subsequently been used in a variety of analyses at multiple experiments, including this work.

A more recent work by Peter Skands [40] makes use of factorization to use different sets of experimental data to tune different sets of parameters resulting in a new set of tunes named Perugia. This work used LEP data to tune the final state radiation and hadronization parameters. Initial state radiation and primordial k_T were tuned using Drell-Yan p_T spectra from CDF and D0, which had a $\sqrt{s} = 1800$ GeV. Charged particle distributions from CDF and E735 were used for the tuning of underlying event, beam remnant, and color reconnection parameters. The energy scaling of the parameters was tested using charged particle multiplicities from CDF and UA5, which cover the range 200 GeV to 1800 GeV. The Perugia set of tunes made use of the Professor [41] automated tuning tool to find some of the parameters. The Pro-pT0 tune used in this work was a result of the Perugia analysis.

4.2 STAR Simulation Framework

The STAR simulation software can be divided into two primary components. The first part deals with the generation of events according to physical distributions and the simulation of the interactions of the resulting particles with the detector. The second deals with the simulation of the behavior of the detector in response to the energy depositions that result from the first part.

The STAR Software and Computing team has developed STARSIM, which in-

tegrates PYTHIA event generation with detector simulation using GEANT3 routines. The STAR detector geometry is described by the Advanced Geometry Interface (AGI) language, which is an object-oriented extension to FORTRAN designed for use with GEANT. STARSIM takes the particle lists provided by PYTHIA and determines where the particles interact with the detector and what amounts of energy are deposited in each detector volume. A list of these deposits in the form of a GEANT table is saved to a file in the STARSIM output format (FZD), which also includes the particle table.

The second stage of the simulation software converts the list of energy deposits into energies or ADC values in the appropriate detector element and outputs a MuDst file that is identical to those produced during the processing real data. In fact, the software used for data production, a Big Full Chain (BFC), has been developed for use in simulation mode. The most significant effort is spent on converting energy deposits in the TPC gas volume into hits in the TPC readout, but non-trivial amounts of work are required to make sure that, for instance, the behavior of the calorimeters is consistent between data and simulation.

An important recent advancement in the STAR simulation framework was the introduction of filtering [42]. One major hurdle in the production of simulation is that it takes a long time to obtain a comparable amount of simulation events to data events because the amount of CPU time needed to create a simulation event is about a factor of 10 higher than for data. This problem can be overcome for specific analyses by cutting certain events before they go through the most time intensive-simulation steps.

A new STAR base class was written for each of the two parts of the simulation framework. The workflow of the framework including filters is shown in Fig. 4-1. The StMcFilter class is the basis for filters written to run in STARSIM. It allows a filter to skip an event immediately (1) after the PYTHIA event is generated, (2) after the vertex for the event is generated according to a user input distribution, and (3) after interactions between the particles and all of the detector elements have been simulated. Generally, it is most effective to apply a filter at (1) or (2) because detector interactions are the most expensive part of the computation. The StFilterMaker class

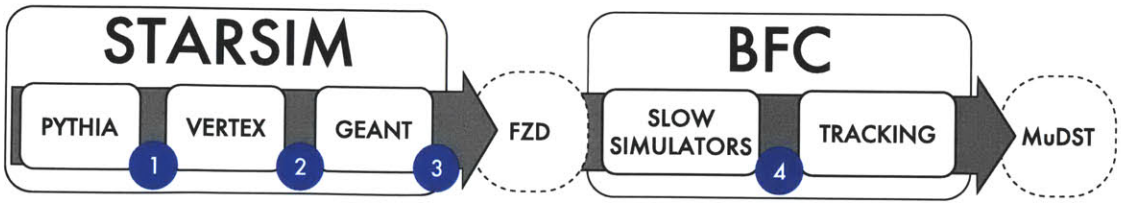

Figure 4-1: The STAR simulation framework with the locations in which filters can be inserted. Steps 1, 2, and 3 are implemented in STARSIM using StMcFilter and step 4 is implemented in BFC using StFilterMaker.

is the basis for filters that reside in BFC. This class is designed to be inserted in the chain after makers that produce information that the filter needs, but before any additional, generally slower, makers are needed. This class is most effectively used when the filter makes a decision before any sort of TPC reconstruction is done.

4.3 Simulation Productions

4.3.1 2005 Simulation

The simulations used for the 2005 cross section analysis were produced at the RACF using the SL05f library. The specific productions with the values used for CKIN(3) and CKIN(4) are described in Table 4.1. The PYTHIA parameters CKIN(3) and CKIN(4) set the minimum and maximum, respectively, p_T of the hard interaction in the frame of the two interacting partons. This frame does not coincide with lab frame. Some the productions had additional phase space cuts to increase the number of dijets present. From the table, it should be evident that the range of luminosities varies widely across the partonic p_T bins. This simulation was produced prior to the implementation of the filtering framework.

4.3.2 2009 Simulation

The simulations used for the 2009 asymmetry analysis were produced at the Clemson Palmetto cluster using the SL10i library using cloud computing resources. This exercise is described in more detail in Appendix C. The specific productions are detailed

Table 4.1: 2005 Dijet Simulation Productions

Production	N_{events}	σ (pb)	**CKIN(3)**	**CKIN(4)**
rcf1228	395703	3.90×10^5	15	25
rcf1229	396767	1.02×10^4	25	35
rcf1230	100000	5.31×10^2	35	-
rcf1270	120000	2.86×10^1	45	55
rcf1271	120000	1.45×10^0	55	65
rcf1224	422116	1.37×10^8	5	7
rcf1233	592384	3.15×10^8	4	5
rcf1232	398837	1.30×10^9	3	4
rcf1312	542000	2.58×10^6	7	9
rcf1313	746200	1.90×10^6	9	11
rcf1314	116000	1.07×10^5	11	15
rcf1315	420000	5.70×10^5	11	15
rcf1316	158000	2.58×10^5	11	15

Table 4.2: 2009 Dijet Simulation Productions

Production	N_{events}	σ (pb)	**CKIN(3)**	**CKIN(4)**
grid10040	8.109×10^9	8.831×10^9	2	3
grid10041	1.295×10^9	1.434×10^9	3	4
grid10042	3.723×10^8	3.723×10^8	4	5
grid10043	1.398×10^8	1.398×10^8	5	7
grid10044	2.296×10^7	2.107×10^7	7	9
grid10045	5.510×10^6	5.073×10^6	9	11
grid10046	2.224×10^6	2.150×10^6	11	15
grid10047	3.888×10^5	4.642×10^5	15	25
grid10048	1.074×10^4	1.037×10^4	25	100

in Table 4.2 and made use of the filtering framework. A STARSIM filter was used for partonic p_T between 2 and 9 GeV and a BFC filter was used between 2 and 15 GeV. Because filtering was used, a consistent luminosity was achieved across all partonic p_T bins.

Chapter 5

Cross Section

5.1 Data Set

The proton-proton data used in this analysis were taken during the 2005 STAR run and were produced using the P05if library. A run list of 805 runs was used making 2.27 pb^{-1} [43] available. The dijets were reconstructed only from events that satisfied the Barrel Jet Patch Threshold 2 (BJP2) trigger (id 96233), which had an E_T threshold of 6.4 GeV. Minimum bias (MB) data (id 96011) were used to measure the time bin acceptance. The reconstruction algorithm did not find any dijets in the minimum bias data with the available statistics.

5.2 Measurement

The formula used to calculate the 2005 dijet cross was

$$\frac{d\sigma_i}{dM_i} = \frac{1}{\Delta M_i}\frac{1}{L}\frac{1}{A_{vert}}\frac{1}{\epsilon_i^{reco,vert}}\sum_j \alpha_{ij}\epsilon_j^{misreco}\frac{1}{\epsilon_j^{trig}}J_{j,reco}^{trig}, \tag{5.1}$$

where $\frac{d\sigma_i}{dM_i}$ was the differential cross section integrated over bin i, ΔM_i was the bin width, L was the sampled integrated luminosity, A_{vert} was the trigger timebin acceptance correction, $\epsilon_i^{reco,vert}$ was the unfolded dijet reconstruction and vertex reconstruction efficiency, α_{ij} was the unfolding matrix, $\epsilon_j^{misreco}$ was the misreconstruction

efficiency for dijets, ϵ_j^{trig} was the reconstructed dijet trigger efficiency, and $J_{j,reco}^{trig}$ was the reconstructed triggered dijet yield in the j^{th} bin of reconstructed invariant mass. How each one of these was calculated or measured is explained in subsequent sections. A discussion of where this formula comes from can be found in Appendix D.

Reconstructed Data Dijets

The reconstructed dijets were taken from the BJP2 triggered data from the 2005 proton-proton data set. These data had a nominal E_T threshold of 6.4 GeV, which corresponds to a DSM ADC threshold of 83 [44] summed over a 1.0 by 1.0 (in $\eta - \phi$) patch of BEMC towers. The threshold corresponds to a calculation using ideal gains calculated assuming the full scale of the towers was at 30 GeV.

The BJP2 trigger had a minimum bias trigger requirement, which was a requirement on the time separation of signals above threshold in the east and west Beam Beam Counters (BBC). The BBC coincidence signal was divided into time bins according to the time difference between the east and west siganls. Only events that fell in BBC time bins 7 and 8 were used in this analysis to an additional software trigger requirement was that the JP had a calibrated, reconstructed E_T that was greater than 8.5 GeV so that triggered events would be above the trigger turn-on (Fig. 5-1).

Jetfinding was performed on a list of four vectors that correspond to particles observed in the detector. During the 2005 run, the Time Projection Chamber (TPC) provided charged track reconstruction over the pseudorapidity range $-1.3 < \eta < 1.3$ and the Barrel Electromagnetic Calorimeter (BEMC) provided electromagnetic energy measurement over the pseudorapidity range $0 < \eta < 1$ (at this time only the west barrel had been commissioned).

Jets were reconstructed using an iterative cone with midpoint seeds and split-merge jetfinding algorithm [45]. The cone radius was $R = 0.4$ with a minimum seed energy of 0.5 GeV and a minimum associated particle energy of 0.1 GeV. The split-merge fraction for the algorithm was set to 0.5. Tracks from the TPC and energy depositions from the BEMC were used as the input particles to the algorithm. Energy depositions in the BEMC were corrected for MIP depositions prior to jetfinding by

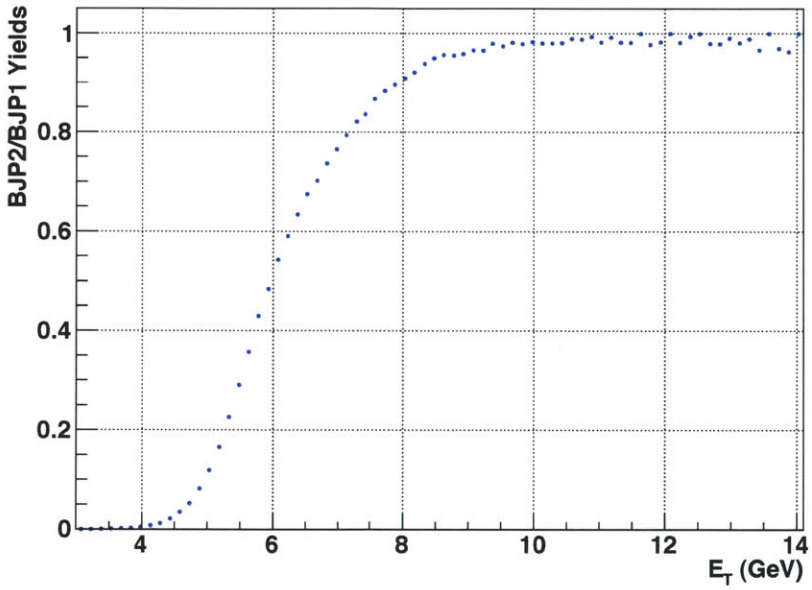

Figure 5-1: The trigger turn-on for the BJP2 trigger as a function of reconstructed Jet Patch E_T. The plateau value is at 0.95. This analysis used a cut at 8.5 GeV to be above the turn-on.

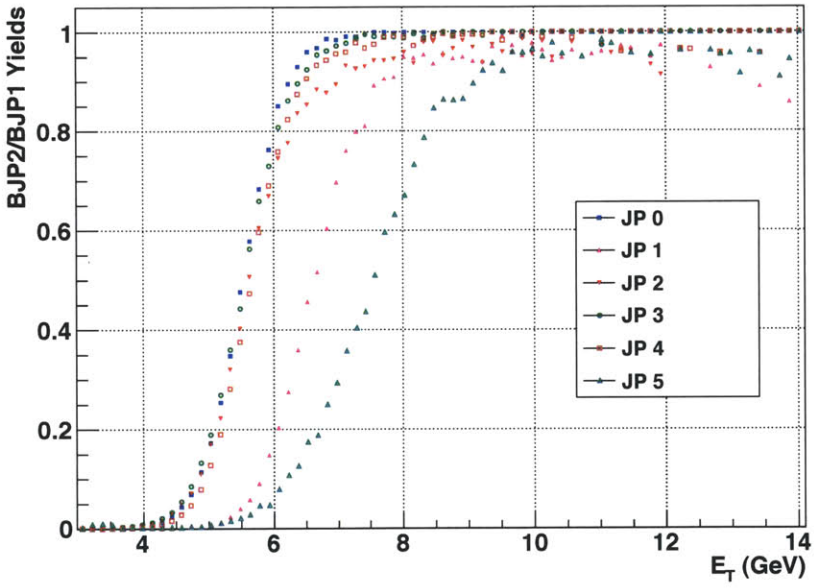

Figure 5-2: The trigger turn-on for each jet patch for BJP2. The threshold varied from patch to patch due to the difference between the ideal calibration used for the trigger threshold and the actual calibration calculated later.

subtracting the MIP energy from any tower that had a track projected to it. The MIP subtracted was calculated according to the pseudorapidity dependent function [46]

$$E_{MIP} = 0.261 * (1 + 0.056 * \eta^2) * cosh\eta \text{ (GeV)}. \quad (5.2)$$

All tracks from the TPCs were assumed to be $\pi^{\pm}$ and BEMC energy depositions were assumed to be photons for the purpose of specifying the mass of each particle.

After jetfinding was finished, events with two or more jets and a reconstructed vertex were examined for dijet candidates using the following algorithm.

1. Remove all jets with jet axis outside the acceptance: $0.2 < \eta_{detector} < 0.8$.

2. Choose the two jets with the highest p_T.

3. Check the two jet axes are within the acceptance: $-0.05 < \eta_{particle} < 0.95$ and $|\Delta\eta_{particle}| < 0.5$.

4. Check that the two jet axes are back to back: $|\Delta\phi| > 2.0$.

5. Apply the asymmetric jet p_T cut: $max(p_{T1}, p_{T2}) > 10$ (GeV/c) and $max(p_{T1}, p_{T2}) > 7$ (GeV/c).

6. Apply geometric trigger condition: one of the jets points to the fired JP and has $0.1 < f_{Neutral} < 0.8$. Here $f_{Neutral}$ is the neutral energy fraction of the jet.

7. Calculate the invariant mass of the two jets and increment histogram.

The invariant mass can be calculated according to

$$M = \sqrt{E_1 E_2 (1 - cos\psi)}, \quad (5.3)$$

where E_i are the jet energies and ψ is the opening angle between them.

The purpose of the asymmetric cut was to improve the stability of NLO calculations, which will be compared to this measurement [47].

Table 5.1: Raw Dijet Yields

Mass	$J^{trig}_{j,reco}$
20 - 24.25	2470
24.25 - 30.01	3326
30.01 - 37.90	2427
37.90 - 48.83	1073
48.83 - 64.15	312
64.15 - 85.92	35
85.92 - 117.29	0

Reconstructed Simulation Dijets

The simulation sample used for calculating the correction factors is described in Section 4.3.1 and the specific productions are outlined in Table 4.1.

Events in the MC sample were reweighted based on their vertex to have a distribution that more accurately reflects the data vertex distribution for dijet candidates in time bins 7 and 8 (Fig. 5-5). This weight was calculated by parameterizing the ratio of the two vertex distributions and fixing the normalization so that the reweighted distribution would have the same integral as before.

Before using the MC based corrections, agreement between the reconstructed dijets at the detector level from the data and the simulation chain was verified (see Fig. 5-4). The MC distribution was normalized to have the same integral as the data distribution over the invariant mass range 20 - 86 GeV. The same normalization factor was then applied the MC η_{34} and $cos\theta^*$ distributions.

5.2.1 Reconstructed Dijet Trigger Efficiency

The trigger efficiency was calculated by comparing the simulation reconstructed dijet spectrum that passed the BJP2 trigger with all reconstructed dijets according to the formula

$$\epsilon^{trig}_j = \frac{J^{trig}_{reco,j}}{J_{reco,j}}, \tag{5.4}$$

where ϵ^{trig}_j was the trigger efficiency in the j^{th} reconstructed dijet bin, $J^{trig}_{reco,j}$ was the dijet yield in the j^{th} reconstructed dijet bin with all trigger requirements applied,

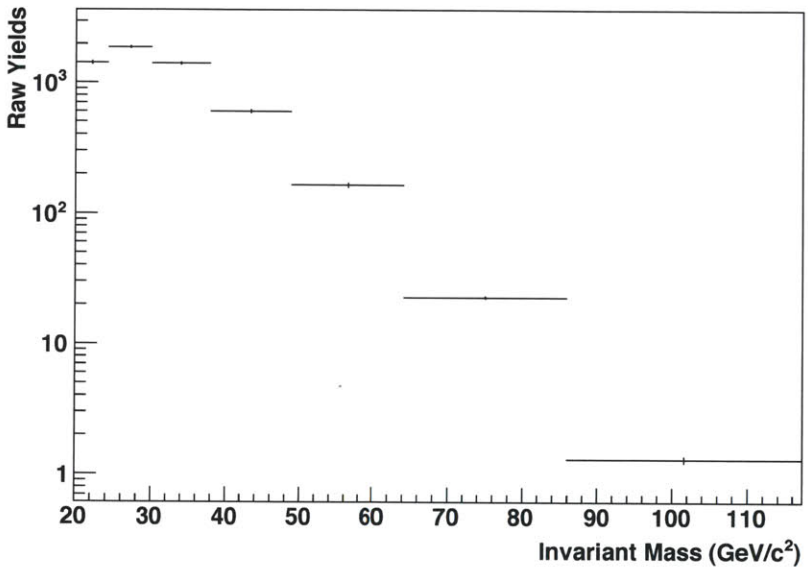

Figure 5-3: The raw yields from the simulation sample after passing all of the same cuts as the data raw yields. The events were reweighted based on their vertex to match the data vertex distribution. The events from different partonic p_T bins were added using the cross section weights, so these yields are scaled by those weights.

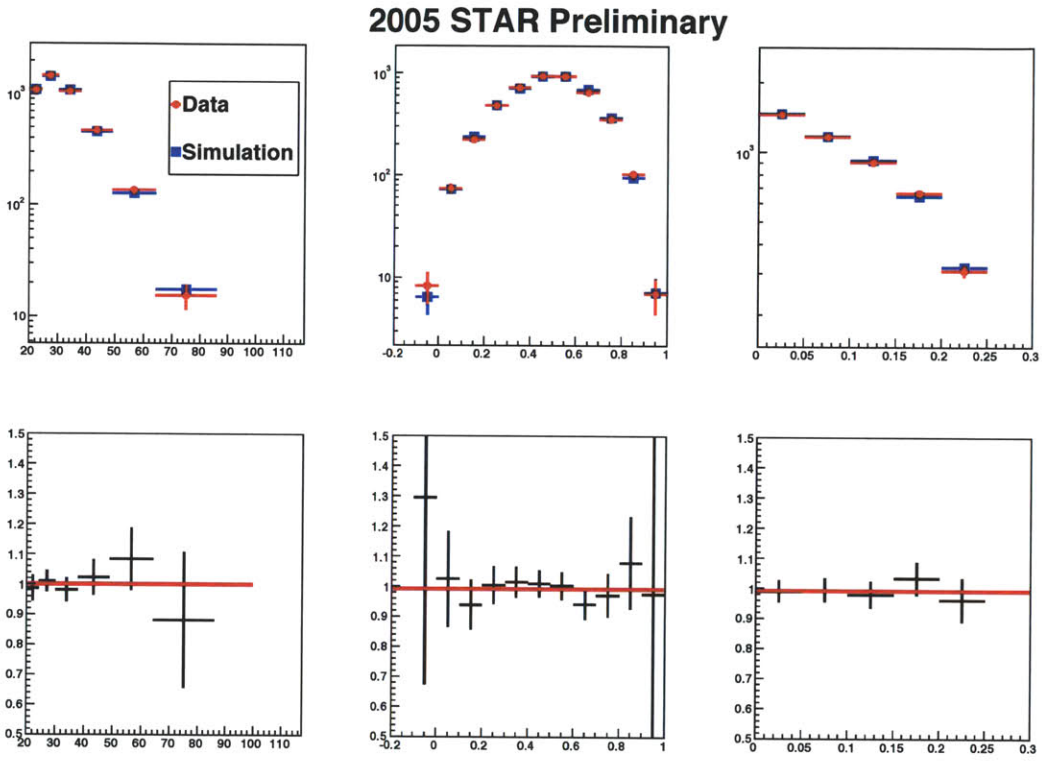

Figure 5-4: The figure shows the comparison of reconstructed dijet distributions in data and simulation after all the same cuts are applied. Data are red in the figures and simulations are blue.

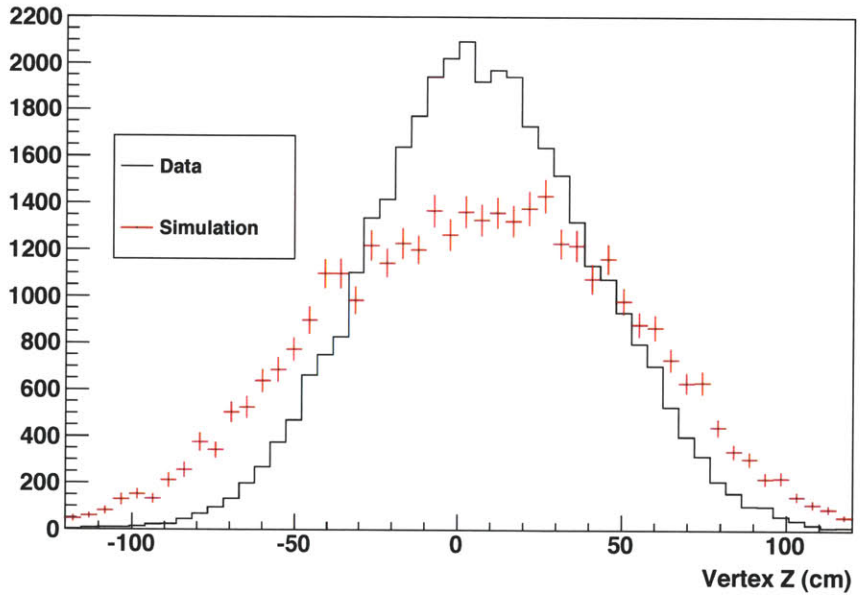

Figure 5-5: The vertex distribution for dijet events in data (within time bins 7 and 8) varies from the distribution for simulation, so a reweighting was applied based on the ratio of the distributions.

Table 5.2: Trigger Efficiency

Mass	ϵ_j^{trig}
20 - 24.25	0.16
24.25 - 30.01	0.32
30.01 - 37.90	0.52
37.90 - 48.83	0.71
48.83 - 64.15	0.86
64.15 - 85.92	0.92
85.92 - 117.29	0.97

and $J_{reco,j}$ was the dijet yield in the j^{th} reconstructed dijet bin without any trigger conditions applied. In this case, the trigger included the BJP2 trigger simulator, the additional offline threshold of 8.5 GeV, and the geometric trigger. This correction was applied prior to unfolding so that trigger effects were removed.

5.2.2 Misreconstruction Efficiency

The misreconstruction efficiency $\epsilon_j^{misreco}$ took into account how many dijets in reconstructed bin j were not associated with a particle level dijet. This efficiency was calculated in simulation according to the formula

$$\epsilon_j^{misreco} = \frac{J(\text{reconstructed bin j} \mid \text{any particle bin})}{J(\text{reconstructed bin j})}, \tag{5.5}$$

where J(reconstructed bin j | any particle bin) was the reconstructed dijet yield in bin j when there was a dijet at the particle level in any particle bin and J(reconstructed bin j was the total reconstructed dijet yield in bin j. Events might not have dijets at the reconstructed and the particle level if, for instance, one of the particle jets did not pass the jet p_T cuts, but both reconstructed jets did. The values calculated for this correction are presented in Table 5.3.

Table 5.3: Misreconstruction Efficiency

Mass	$\epsilon_j^{misreco}$
20 - 24.25	0.73
24.25 - 30.01	0.90
30.01 - 37.90	0.96
37.90 - 48.83	0.97
48.83 - 64.15	0.98
64.15 - 85.92	0.99
85.92 - 117.29	0.99

5.2.3 Unfolding Matrix

The purpose of unfolding was to take the reconstructed dijet spectrum to the particle dijet spectrum by correcting for detector effects. There were a number of effects that were implicitly addressed in this step. Examples include the double counting of electron energy, lost neutral hadrons, energy leakage in towers, missing tracks, and others. The individual impact of each of these effects was not quantified. An unfolding matrix A described how to undo the detector effects on a reconstructed invariant mass spectrum. The method used in this analysis was based on the method known in the literature as the Bayes unfolding method [48].

There were a couple of reasons that an unfolding method was used in this analysis. The detector smearing results in significant contribution to unfolded bins from the off-diagonal components. Using an unfolding method allowed for a statistical understanding of the correction factors. Furthermore, an unfolding method allowed the measurement to be extended to bins where the most significant contributions could be from other bins.

Reasons explaining the advantages of the Bayes unfolding method over other methods are described in [48], with the most pertinent reproduced here:

- It is theoretically well grounded.
- The domain of definition of the reconstructed values may differ from that of the true values.
- It can take into account any source of smearing or migration.

- Even in the case of total ignorance about the true distribution, satisfactory results can be obtained (See Appendix E).

- It does not require matrix inversion.

- It provides the correlation matrix of the results.

The method here differed slightly from the method in [48]. In this analysis, efficiencies were factored out of the unfolding matrix M. Therefore, the matrix definition and uncertainties were slightly different. No iteration was used in this analysis because the agreement between the Monte Carlo and data is so good (see Fig. 5-4).

Typically, matrix unfolding techniques define a transfer matrix H that relates the true spectrum $\mathbf{y}$ to the observed spectrum $\mathbf{x}$ according to

$$\mathbf{x} = H\mathbf{y} \tag{5.6}$$

$$\mathbf{y} = H^{-1}\mathbf{x}. \tag{5.7}$$

The inverse transfer matrix is required to correct the reconstructed distribution to the particle distribution, but inverting any moderately sized matrix (which is needed for this measurement) is computationally intensive and prone to errors. The Bayes unfolding method used here instead avoided the matrix inversion problem by calculating the unfolding matrix directly from the MC information. Using the simulation sample described in Section 5.1, events where a dijet was found at both the particle and reconstructed level were used to populate the matrix.

This matrix A (since it is not the true inverse of the transfer matrix) could be calculated according to

$$\alpha_{ij} = \frac{J(\text{particle bin i, reconstructed bin j})}{J_{j,reco}}, \tag{5.8}$$

where α_{ij} was an element of the matrix, J(particle bin i, reconstructed bin j) was the number of dijets found in reconstructed bin j and in particle bin i in the simulation

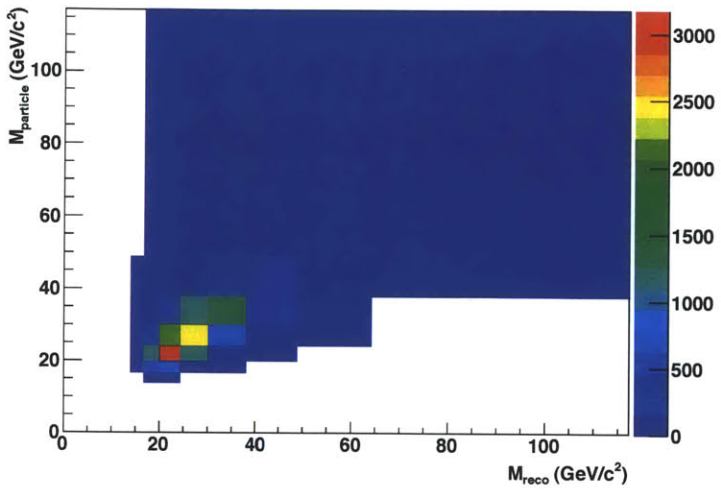

Figure 5-6: The relation between M_{reco} and $M_{particle}$ was used to determine the unfolding matrix. This histogram shows the unnormalized contributions of each bin in detector invariant mass to each bin in particle invariant mass.

sample, and $J_{j,reco}$ was the yield of dijets found in recontructed bin j for the same simulation. This normalization was determined by requiring that the integral of the particle and reconstructed spectra were the same.

The matrix α used for this analysis is given in Table 5.4. The same bins were chosen to be the same for both the reconstructed and the particle spectra, but this choice was not required in general. This method did not bias the shape of the particle distribution away from the trigger turn on (See Appendix E).

5.2.4 Particle Dijet and Vertex Reconstruction Efficiency

This efficiency in Eq. (5.9) told how often an event with a particle dijet will have a reconstructed dijet and a reconstructed vertex from the Pileup Proof Vertex Finder (PPV). It was assumed that this efficiency was independent of vertex in our time bins of interest. In practice, the reconstructed efficiency and the vertex efficiency

Table 5.4: Unfolding Matrix

M_{true} \ M_{reco}	-10.0	0.0	11.57	13.89	16.67	20.0	24.25	30.01	37.90	48.83	64.15	85.92	117.29	163.15
-10.0 - 0.0	0	0	0	0	0	0	0	0	0	0	0	0	0	0
0.0 - 11.57	0	0	0	0	0	0	0	0	0	0	0	0	0	0
11.57 - 13.89	0	0	0	0	0	0	0	0	0	0	0	0	0	0
13.89 - 16.67	0	0	0	0	0	0	0	0	0	0	0	0	0	0
16.67 - 20.0	0	0	0	0.43	0.23	0.11	0.03	0	0	0	0	0	0	0
20.0 - 24.25	0	0	0	0.46	0.55	0.48	0.23	0.03	0	0	0	0	0	0
24.25 - 30.01	0	0	0	0.11	0.20	0.33	0.47	0.28	0.03	0	0	0	0	0
30.01 - 37.90	0	0	0	0	0.02	0.07	0.24	0.52	0.32	0.03	0	0	0	0
37.90 - 48.83	0	0	0	0	0	0	0.03	0.15	0.54	0.38	0.01	0	0	0
48.83 - 64.15	0	0	0	0	0	0	0	0.01	0.10	0.53	0.48	0.05	0.38	0.59
64.15 - 85.92	0	0	0	0	0	0	0	0	0	0.06	0.48	0.62	0.27	0.39
85.92 - 117.29	0	0	0	0	0	0	0	0	0	0	0.02	0.34	0.34	0.02
117.29 - 163.15	0	0	0	0	0	0	0	0	0	0	0	0	0.02	0
163.15 - 600	0	0	0	0	0	0	0	0	0	0	0	0	0	0

Table 5.5: Vertex and Reconstruction Efficiency

Mass	$\epsilon_i^{reco,vert}$
20 - 24.25	0.09
24.25 - 30.01	0.20
30.01 - 37.90	0.31
37.90 - 48.83	0.36
48.83 - 64.15	0.40
64.15 - 85.92	0.38
85.92 - 117.29	0.30

were calculated according to the formula

$$\epsilon_i^{reco,vert} = \frac{J(\text{any reconstructed bin, reconstructed vertex} \mid \text{particle bin i})}{J(\text{particle bin i})}, \quad (5.9)$$

where $\epsilon_i^{reco,vert}$ was the vertex and reconstruction efficiency for the i^{th} particle bin, J(particle bin i, any reconstructed bin, reconstructed vertex) was the dijet yield in the i^{th} particle bin that corresponded to a reconstructed dijet in any reconstructed bin and a reconstructed vertex, and $J_{i,particle}$ was the dijet yield in the i^{th} particle bin. This efficiency was calculated using the simulation sample.

5.2.5 Trigger Time Bin Acceptance Correction

A cut was placed on BBC time bin to keep events near the center of the detector. The cut on time bin was applied instead of a cut on reconstructed vertex to try to disentangle the acceptance from the vertex reconstruction efficiency. The basic idea was that the analysis should include only events that happened near the center of the detector to reduce extreme acceptance effects. Physics, however, should be independent of vertex z, so an acceptance should be used to correct the cross section. Vertex reconstruction efficiency definitely depended on vertex z and probably on invariant mass, so these effects were removed by having separate acceptance and vertex reconstruction efficiency corrections.

This factor needed to be included to account for the fact that luminosity was calculated based on the full vertex distribution.

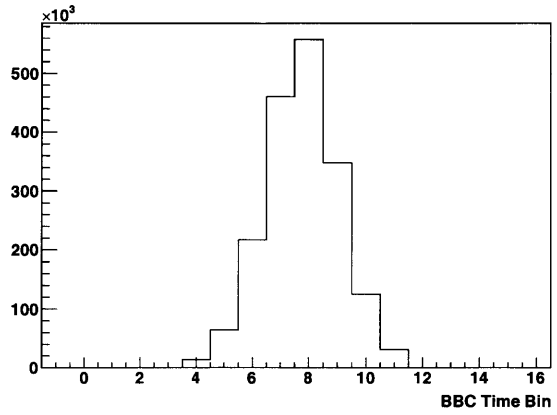

Figure 5-7: The BBC time bin distribution for the minimum bias trigger.

This factor quantified the acceptance of the time bin cut. There was a total of 1.82×10^6 MB events with 1.02×10^6 events in time bins 7 or 8, resulting in an acceptance of 0.56 (see Fig. 5-7), which was calculated as a ratio of those two numbers according to the formula

$$A_{vert} = \frac{N_{MB}(\text{time bins 7 and 8})}{N_{MB}(\text{all time bins})}. \tag{5.10}$$

5.2.6 Integrated Luminosity

The integrated luminosity for the run list used was 2.27 pb^{-1}, which was calculated according to the formula:

$$\int \mathcal{L} = \frac{N_{MB}^{recorded} \cdot \langle PS_{MB} \rangle}{\sigma_{MB}}, \tag{5.11}$$

where $\int \mathcal{L}$ was the integrated luminosity, $N_{MB}^{recorded}$ was the total number of recorded MB events, $\langle PS_{MB} \rangle$ was the luminosity weighted average prescale over the data set, and σ_{MB} was the MB cross section. This value corresponded to a total of 1.8×10^6 minimum bias triggered events with an average prescale of 32,612 for this period. The

cross section for the minimum bias trigger was $\sigma_{BBC} = 26.1 \pm 0.2(\text{syst}) \pm 1.8(\text{stat})\text{mb}$ [49].

5.3 Dijet Statistical Uncertainties

Besides the usual statistical uncertainties, this measurement was affected by the finite Monte Carlo statistics used in calculating the correction factors. These effects were included in the statistical uncertainties on the measurement. Though the statistical uncertainties for the multiple correction factors were correlated, they have been added for each correction. This procedure resulted in a slight overestimation of the uncertainties.

The unfolding matrix introduced the need to take special care in propagating the statistical uncertainties. Recall that

$$J_i^{particle} \propto \sum_j \alpha_{ij} J_j^{reco}. \tag{5.12}$$

Assuming infinite simulation statistics and using a diagonal covariance matrix V for J_j^{reco}, the elements of the covariance matrix of $J_i^{particle}$ V' could be calculated according to

$$V'_{ij} = \sum_p \sum_q \alpha_{pj} \sqrt{V_{pp} V_{qq}} \alpha_{qi}, \tag{5.13}$$

where α_{ij} was the unfolding matrix element and $V_{ij} = \delta_{ij}\sigma_i\sigma_j$ were the elements of the covariance matrix of the reconstructed dijets.

However, the Monte Carlo statistics were finite, so there was an additional contribution to V' to account for the uncertainty in the matrix elements α_{ij} that could be described by

$$V'_{ij} = \sum_p \sum_q \alpha_{pj} \sqrt{V_{pp} V_{qq}} \alpha_{qi} + V_{jj} * \sigma^2_{\alpha_{ij}}, \tag{5.14}$$

where $\sigma_{\alpha_{ij}}$ is the uncertainty on the unfolding matrix element α_{ij} due to the limited Monte Carlo statistics.

A comparison of the statistical uncertainties is provided in Table 5.6. The frac-

Table 5.6: Expected statistical uncertainties compared with actual statistical uncertainties

Mass	Equivalent Counts (N)	$\frac{1}{\sqrt{N}}$	Fractional Statistical Uncertainty
20 - 24.25	186809.5	0.0023	0.049
24.25 - 30.01	92327.1	0.0033	0.037
30.01 - 37.90	33695.3	0.0054	0.035
37.90 - 48.83	9486.9	0.010	0.047
48.83 - 64.15	1895.5	0.023	0.062
64.15 - 85.92	216.2	0.068	0.12
85.92 - 117.29	5.92	0.41	0.48

tional statistical uncertainties were compared using the calculated statistical uncertainty for this measurement and the expected statistical uncertainty due to the equivalent counts in each bin. In all bins the actual uncertainty exceeded the expected uncertainty, which was expected because of contributions from limited Monte Carlo statistics.

5.4 Dijet Systematic Uncertainties

This section outlines the systematic uncertainties that are accounted for in the 2005 dijet cross section measurement. The formula that was used to calculate the dijet cross section is explained in section 5.2.

5.4.1 Normalization Uncertainty

The luminosity had an uncertainty of 8% which introduces an overall normalization uncertainty on the cross section [49]. See section 5.2.6.

5.4.2 Vertex Acceptance Uncertainty

The vertex acceptance correction was calculated using minimum bias events based on the assumption that earlier corrections removed trigger dependencies. However, there was a noticeable difference (see Fig. 5-8) between the time bin distributions

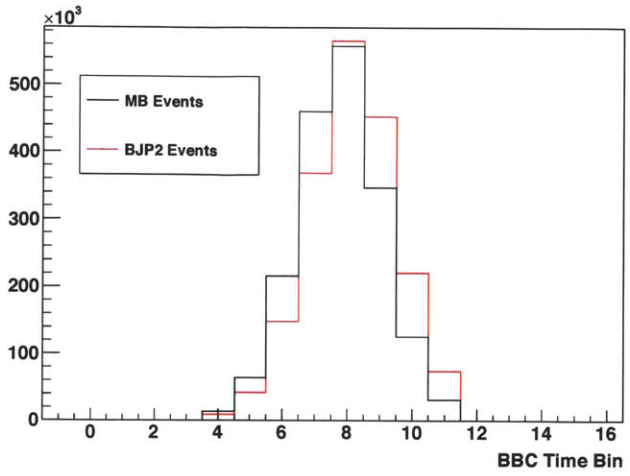

Figure 5-8: The BBC time bin distributions for the minimum bias trigger (black) and the BJP2 trigger (red) were noticeably different. The BJP2 distribution has been rescaled for comparison.

for different triggers due to the fact that the BJP2 trigger only fired based on electromagnetic energy depositions in the West half of the BEMC. It was impossible to determine if this bias had been corrected for using the data available. To assess this bias, there would need to be a significant sample of minimum bias events that had dijets reconstructed. This sample could be used to correct or check the time bin distribution for the BJP2 events.

This systematic was calculated by comparing the vertex acceptance for each of the two triggers. This difference was 6%, which was taken to be the normalization uncertainty due to the acceptance correction.

5.4.3 Reconstructed Dijet Trigger Efficiency Uncertainty

The systematic uncertainty due to the reconstructed dijet trigger efficiency uncertainty was the uncertainty in how well the plateau of the reconstructed dijet trigger efficiency agreed with data. Since there was not a way to do this with this data

because of the lack of proper triggers and statistics, it was only verified that the data were taken well above the trigger turn-on region (See Section 5.2). The uncertainty here was included in the treatment of the BEMC energy scale uncertainty.

There was another systematic uncertainty that was related to the trigger, which was how well the location of the trigger turn-on curve can be constrainted. This was called the trigger efficiency turn-on uncertainty. This uncertainty was mainly due to the BEMC energy scale uncertainty and was treated in the section on the BEMC energy scale uncertainty.

5.4.4 Jet Energy Scale Uncertainty

The systematic uncertainties that were included in the calculation of the Jet Energy Scale (JES) uncertainty were the BEMC energy scale uncertainty, the BEMC efficiency uncertainty, the track momentum scale uncertainty, the track finding efficiency uncertainty and the uncertainty in the calculation of the hadronic response of the BEMC. Each of these uncertainties is detailed in the following subsections.

BEMC Energy Scale Uncertainty

Because of the way the unfolding and trigger efficiency corrections were calculated, namely that they rely on the STAR Monte Carlo, there were actually two energy scales and therefore two uncertainties that were present in this analysis: the experimental BEMC energy scale uncertainty (ExBES uncertainty) and the Monte Carlo BEMC energy scale uncertainty (McBES uncertainty). For the part of the analysis chain where each of these energy scales enters, see Fig. 5-9. For more information about what was exactly incorporated in each scale, see Appendix B for a model of the BEMC simulation chain.

Before the proper method to incorporate these two uncertainties into this analysis is discussed, the calculation of each is outlined. The ExBES and its uncertainty were calculated in [50] and was found to be 4.8%. In all previous analyses, the McBES has been assumed to be equivalent to the ExBES. Furthermore, the McBES uncertainty

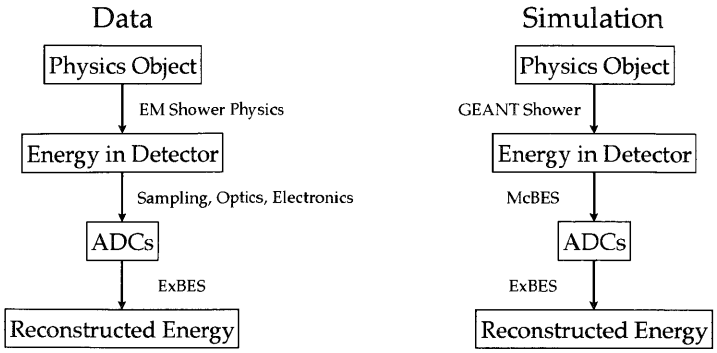

Figure 5-9: A graphic showing where the two BEMC energy scales, the ExBES and the McBES, were used in calculation involving simulated data or real data.

has never been given a quantitative estimate and was always assumed to be zero and contribute nothing to the uncertainty of a measurement. Therefore as a first estimate of the McBES uncertainty, it has been assumed to be equal to the ExBES uncertainty.

With an estimate of the McBES uncertainty, the question of how to vary it in relation to the ExBES uncertainty arises. Because it has not been studied before and there was no knowledge of the correlation between the two scales, the McBES scale has been varied in an uncorrelated manner with the ExBES scale. In the future a study will hopefully be done that will estimate the McBES uncertainty as well as its correlation with the ExBES since this method most likely overestimated the uncertainty due to the McBES. A better estimate would likely be to vary the ExBES and McBES energy scales in a completely anti-correlated fashion because many of the simulation calculations and our measurements have been found to be in agreement. But until the agreement between the ExBES and McBES and their correlation, is established quantitatively, this should not be done and was not done in this analysis.

To determine the contribution of these two uncertainties to the total uncertainty, they were varied independently. The ExBES, as calculated in [50], was a maximum

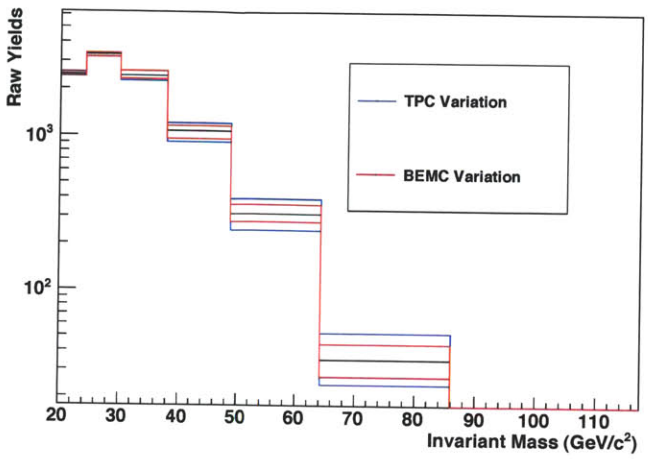

Figure 5-10: The black curve on this figure displays the raw data dijet yields. The red curves were produced by recalculating the yields using calibration tables that were shifted high and low. The blue curves were produced by shifting the charged energies in each jet high and low.

extent uncertainty and because the McBES was being taken as equal to the ExBES, it was also a maximum extent uncertainty. This means that for both the McBES gains and ExBES gains there were three different sets: the nominal 2005 BTOW gains, the low variation of the nominal gains and the high variation of the nominal gains.

Three simulation samples were then produced, where in each sample the McBES gains were set to one of the three gains sets. The simulation for each McBES gain set was then reconstructed using a one of the three ExBES gains sets and run through jet finding. This led to 9 different samples. For each sample, a new trigger uncertainty was calculated because the variation of the McBES gains affected the triggering. The uncertainty on the yield due to the BEMC energy scale was then calculated on a bin-by-bin basis where in each bin, the upper bound of the BEMC energy scale uncertainty was taken to be the largest value out of the 9 results and the lower bound of the BEMC energy scale uncertainty was taken to be the smallest value out of the 9 results.

BEMC Efficiency Uncertainty

A status table was used in the simulator to model the dead areas of the detector. For technical reasons, a single status table was chosen that best reflects the average state of the detector during the run. Variations in the different status tables were about 1%. These variations were assumed to introduce a 1% uncertainty in the neutral energy scale of the jets.

BEMC Hadronic Response Uncertainty

The BEMC hadronic response uncertainty related the amount of energy deposited by charged hadrons in the BEMC to the charged energy fraction of the jets. Approximately 20% of the energy of charged hadrons was deposited in the BEMC [51]. The uncertainty on the amount of energy these showers deposited was on average 10%. The track finding efficiency of the TPC at mid-rapidity was 87%, which was calculated by embedding tracks in jets in proton-proton data events [52]. Making some assumptions about the flatness of these distributions, a calculation yielded an uncertainty of 2.3% on the charged energy of the jet.

TPC Momentum Scale Uncertainty

The overall TPC momentum scale uncertainty was 1% [53].

TPC Tracking Efficiency Uncertainty

The uncertainty on the TPC track finding efficiency was approximately 5% and seemed to have no dependence on p_T or jet energy [52]. Therefore, it contributed 5% to the uncertainty on the charged energy scale.

The effects of the BEMC hadronic response uncertainty, the TPC momentum scale uncertainty, and the track finding were combined in quadrature to get the total effect of 5.6% for the charged energy of the jets. To measure the uncertainty due to these effects, each jet had its charged energy shifted up and down by 5.6%. Since this also affected the trigger efficiency, new trigger efficiencies were calculated for these two

Table 5.7: Energy Uncertainty Contributions

Mass	BEMC+	BEMC-	TPC+	TPC-	Total+	Total-
20 - 24.25	0.0021	0.0075	0.51	0.24	0.51	0.24
24.25 - 30.01	0.062	0.051	0.32	0.21	0.33	0.21
30.01 - 37.90	0.11	0.10	0.25	0.18	0.27	0.21
37.90 - 48.83	0.16	0.14	0.21	0.15	0.26	0.21
48.83 - 64.15	0.23	0.19	0.20	0.13	0.31	0.23
64.15 - 85.92	0.34	0.24	0.23	0.16	0.40	0.29
85.92 - 117.29	0.41	0.28	0.26	0.20	0.48	0.34

Table 5.8: Beam Background Uncertainty

Mass	Beam Uncertainty
20 - 24.25	3.8×10^{-3}
24.25 - 30.01	1.9×10^{-3}
30.01 - 37.90	3.3×10^{-3}
37.90 - 48.83	4.6×10^{-3}
48.83 - 64.15	1.5×10^{-4}
64.15 - 85.92	3.7×10^{-4}
85.92 - 117.29	1.7×10^{-3}

states in the simulation. The contribution to the total jet energy scale uncertainty was the difference between each of these distributions and the nominal measurement after being passed through the reconstruction chain.

5.4.5 Beam Background Uncertainty

Beam interactions could cause the reconstruction of background jets. The effect of this phenomenon was reduced by requiring the trigger jet to have a neutral energy fraction $0.1 < f_{neutral} < 0.8$. The amount of background contamination was tested by varying this cut. The maximum difference observed was when the cut was changed to $0.0 < f_{neutral} < 0.9$, so the difference between this distribution and the measurement defined the uncertainty. The effect was found to be below the 0.5% level in all bins.

5.5 Theory Calculation

The dijet theory calculation code was written by Daniel de Florian [54]. It was updated to match the same dijet definition as used in the present algorithm. The PDF used was MRST2004 (NLO) [55]. The code used a midpoint cone jetfinding algorithm to find jets at the parton level.

5.6 Hadronization and Underlying Event Correction

The purpose of applying a hadronization and underlying event correction was to correct theory from the parton level to the particle level. Theoretical calculations included only the hard process between interacting partons, not long-range processes that explain transitions between hadrons and partons. Non-perturbative models were used to describe hadronization, which could result in energy flow out of the jet cone. Similarly, interactions between the remaining partons from the incoming protons could result in energy entering jet cones. The hadronization and underlying event correction was included separately from the theory because it was heavily dependent on the Monte Carlo method used to calculate it. The correction was applied to theory to minimize the model dependence of the measurement.

The hadronization and underlying event correction was calculated using a high statistics PYTHIA sample with 'CDF Tune A' [56]. The simulation production used for this calculation is described in Table 5.9.

To calculate the correction, the STAR jetfinding software was applied to partons after parton branching occurred and after hadronization in each event. It's important to recognize that the partonic dijets were not exactly analogous to the dijets found in the theory calculation because those were calculated at NLO. This could be the source of some discrepancy in the data/theory comparison. The corrected theory dijet yield in the i^{th} bin $J_{i,particle}$ was calculated according to

$$J_{i,particle} = \frac{1}{\epsilon_i} \sum_j \beta_{ij} f_j^{reco} J_{j,partonic}, \tag{5.15}$$

where ϵ_i was the efficiency for particle dijet reconstruction, β_{ij} was the transfer matrix element, f_j was the jetfinding efficiency in the j^{th} partonic mass bin, and $J_{j,partonic}$ was the yield in that bin. These corrections are listed in Tables 5.11 and 5.12.

The efficiency ϵ_i was calculated according to

$$\epsilon_i = \frac{J_{i,particle}(\text{recontructed in any partonic bin})}{J_{i,particle}}, \tag{5.16}$$

where $J_{i,particle}$(recontructed in any partonic bin) was the yield in the i^{th} particle bin of dijets that had a reconstructed dijet in any partonic bin and $J_{i,particle}$ was the dijet yield in the i^{th} particle bin.

The efficiency f_j was calculated according to

$$f_j = \frac{J_{j,partonic}(\text{recontructed in any particle bin})}{J_{j,partonic}}, \tag{5.17}$$

where $J_{j,partonic}$(recontructed in any particle bin) was the yield in the j^{th} partonic bin of dijets that had a reconstructed dijet in any particle bin and $J_{j,partonic}$ was the dijet yield in the j^{th} partonic bin.

The transfer matrix element β_{ij} was calculated according to

$$\beta_{ij} = \frac{J(\text{partonic bin } j, \text{ particle bin } i)}{J_{j,partonic}}, \tag{5.18}$$

where J(partonic bin j, particle bin i) was the number of dijets found in partonic bin j and particle bin i and $J_{j,partonic}$ was the dijet yield in partonic mass bin j.

An example PYTHIA record shown in Table 3.1 shows which partons were used during jetfinding at the parton level. In the record, particles 5 and 6 were the partons that scatter, and particles 7 and 8 were the outgoing partons. Therefore, any parton with that had 3, 4, 5, 6, 7, or 8 as a parent covered parton branching, ISR, and FSR.

Table 5.9: Hadronization and Underlying Event Simulations

CKIN(3)	CKIN(4)	N_{events}	σ
3	4	3.6×10^7	1.30
4	5	2.4×10^7	3.15×10^{-1}
5	6	1.96×10^7	1.36×10^{-1}
7	9	1.715×10^7	2.30×10^{-2}
9	11	3.33×10^7	5.51×10^{-3}
11	15	3.07×10^7	2.23×10^{-3}
15	25	2.3×10^7	3.90×10^{-4}
25	35	8.25×10^6	1.02×10^{-5}
35	45	2.0×10^5	4.99×10^{-7}
45	55	2.0×10^5	2.86×10^{-8}
55	-	1.0×10^4	1.51×10^{-9}

Table 5.10: Particle Reconstruction Efficiency for Hadronization/UE Correction

Mass	ϵ
20 - 24.25	0.560581
24.25 - 30.01	0.69563
30.01 - 37.90	0.765394
37.90 - 48.83	0.814482
48.83 - 64.15	0.855162
64.15 - 85.92	0.751126
85.92 - 117.29	0.920749

Table 5.11: Reconstruction Efficiency for Hadronization/UE Correction

Mass	f^{reco}
20 - 24.25	0.313781
24.25 - 30.01	0.588591
30.01 - 37.90	0.733255
37.90 - 48.83	0.829004
48.83 - 64.15	0.89755
64.15 - 85.92	0.935441
85.92 - 117.29	0.947768

Table 5.12: Transfer Matrix for Hadronization/UE Correction

Mass	0.0	11.57	13.89	16.67	20.0	24.25	30.01	37.90	48.83	64.15	85.92	117.29	163.15
0.0 - 11.57	0	0	0	0	0	0	0	0	0	0	0	0	0
11.57 - 13.89	0	0	0	0	0	0	0	0	0	0	0	0	0
13.89 - 16.67	0	0	0.08	0.66	0.23	0.028	0.0019	5.7e-05	1.1e-05	0	0	0	0
16.67 - 20.0	0	0	0.0051	0.41	0.51	0.075	0.0036	0.00012	2.8e-06	5.4e-07	0	0	0
20.0 - 24.25	0	0	0.00081	0.23	0.6	0.15	0.013	0.00057	1.3e-05	8.7e-08	4.7e-09	0	0
24.25 - 30.01	0	0	8e-05	0.056	0.42	0.45	0.07	0.005	0.00026	1.6e-06	1.8e-08	0	0
30.01 - 37.90	0	0	1.3e-05	0.016	0.097	0.39	0.46	0.043	0.0023	0.00011	9.4e-07	0	0
37.90 - 48.83	0	0	3.3e-05	0.0083	0.043	0.092	0.35	0.48	0.026	0.00088	1.7e-05	4.7e-08	0
48.83 - 64.15	0	0	0	0.0039	0.038	0.052	0.1	0.31	0.48	0.013	0.00016	2.1e-07	0
64.15 - 85.92	0	0	0	0.0018	0.0057	0.037	0.08	0.14	0.28	0.46	0.0048	1e-05	0
85.92 - 117.29	0	0	0	0	0	0.00081	0.036	0.19	0.2	0.25	0.32	0.00065	0
117.29 - 163.15	0	0	0	0	0	0	0	0.1	0.33	0.25	0.23	0.09	0
163.15 - 600	0	0	0	0	0	0	0	0.45	0.23	0.078	0.13	0.11	0

Table 5.13: Data points and Uncertainties

M (GeV/c^2)	$\frac{d\sigma_i}{dM}$ (pb/GeV/c^2) $\pm$ stat - sys + sys
20 - 24.25	$(1.94 \pm 0.095 - 0.52 + 0.55) \times 10^4$
24.25 - 30.01	$(7.06 \pm 0.26 - 1.28 + 1.64) \times 10^3$
30.01 - 37.90	$(1.88 \pm 0.067 - 0.36 + 0.46) \times 10^3$
37.90 - 48.83	$(3.83 \pm 0.18 - 0.79 + 0.96) \times 10^2$
48.83 - 64.15	$(5.45 \pm 0.34 - 1.23 + 1.64) \times 10^1$
64.15 - 85.92	$(4.37 \pm 0.53 - 1.27 + 1.77) \times 10^0$
85.92 - 117.29	$(8.32 \pm 4.02 - 2.84 + 3.99) \times 10^{-2}$

5.7 Results

The dijet cross section has been measured from the 2005 proton-proton data set at STAR. The comparison with a theory calculation produced by de Florian and corrected for hadronization and underlying event contamination using PYTHIA as shown in Fig. 5-11 is consistent with results measured in STAR during later years. The agreement between data and theory is not very good. However, an analysis of 2006 data with a higher acceptance showed a substantial cone radius dependence in the data/theory agreement (see Fig. 5-12) [4]. This study showed that the best agreement between data and theory occurs between R = 0.6 and R = 0.7. The results for the R = 0.4 cone radius are consistent between the 2005 and 2006 analyses.

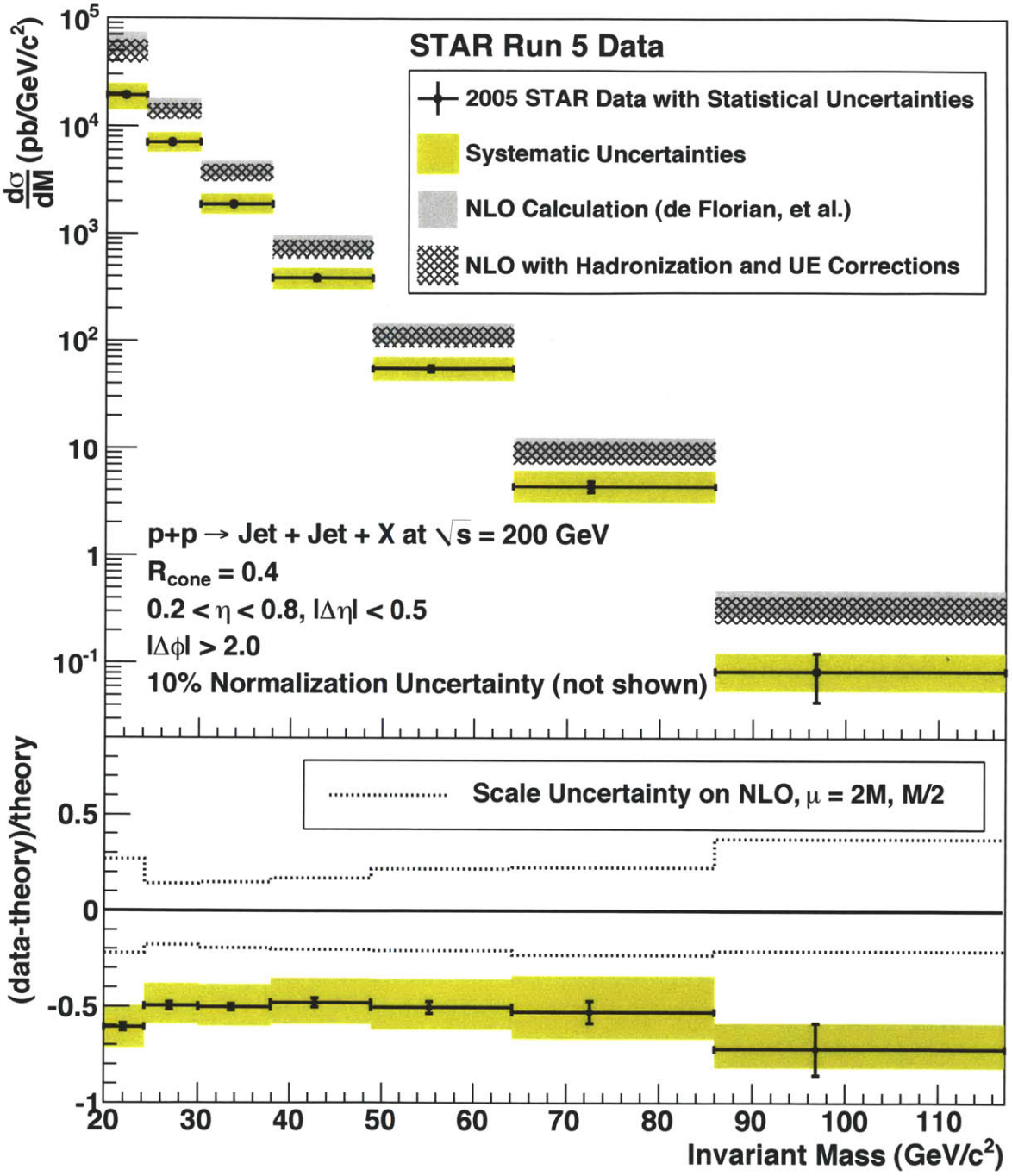

Figure 5-11: The 2005 Dijet Cross Section. The uncertainty bars represent the statistical uncertainties on the measurement including the uncertainties due to the finite statistics in the Monte Carlo sample. The yellow bands carry the uncertainties in the jet energy scale. The top plot shows the value of the cross section and the bottom plot shows the comparison to theory.

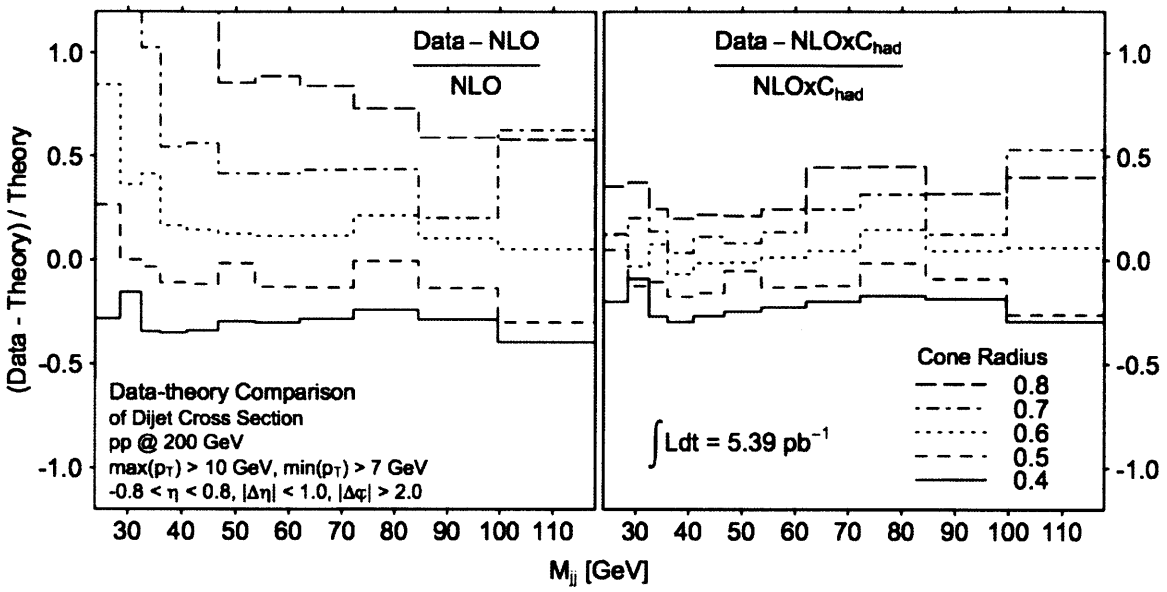

Figure 5-12: A comparison between theory and data for different cone radiuses with the hadronization and underlying event correction included shows significant cone radius dependence. This comparison was calculated using 2006 data in another analysis [4].

Chapter 6

Asymmetry

6.1 Data Set

The proton-proton data used in this analysis were taken during the 2009 STAR run and were produced using the SL10c library. A run list of 470 "golden" runs making up 10.6 pb^{-1} was used in this analysis, which amounted to 33.6 million events. This runlist included quality analysis of various jet variables [57], as well as quality analysis of scalers used for relative luminosity measurements [58]. The trigger was the L2JetHigh trigger (trigger IDs 240650-240652), which was a level 2 trigger that fed off the JP1 trigger. The JP1 threshold was 5.5 GeV and the L2JetHigh trigger looked for a 6 GeV jet opposite a 3 GeV jet.

6.2 Measurement

The formula used to calculate the asymmetry is

$$A_{LL,j} = \frac{\sum_k \sum_i P_{B,i} P_{Y,i} \alpha_{jk} (N_{i,k}^{++} + N_{i,k}^{--}) - \sum_k \sum_i P_{B,i} P_{Y,i} R_i \beta_{jk} (N_{i,k}^{+-} + N_{i,k}^{-+})}{\sum_k \sum_i P_{B,i}^2 P_{Y,i}^2 \alpha_{jk} (N_{i,k}^{++} + N_{10,i,k}^{--}) + \sum_k \sum_i P_{B,i,j}^2 P_{Y,i,j}^2 R_i \beta_{jk} (N_{i,k}^{+-} + N_{i,k}^{-+})}, \tag{6.1}$$

where $A_{LL,j}$ is the value of the asymmetry in the j^{th} bin of particle invariant mass, $P_{B,i}$ and $P_{Y,i}$ are the blue and yellow beam polarizations for run i, R_i is the relative luminosity for the same run, α_{jk} and β_{jk} are the spin dependent unfolding matrices,

and $N_{i,k}$ are the spin dependent yields in the k^{th} reconstructed invariant mass bin from run i.

Reconstructed Data Dijets

As in 2005, jets were reconstructed using an iterative cone with midpoint seeds and split-merge jet-finding algorithm. The cone radius was $R = 0.7$ with a minimum seed energy of 0.5 GeV and a minimum associated particle energy of 0.1 GeV. The split-merge fraction was again 0.5. In 2009, a subtraction scheme to avoid double counting of energy used a 100% subtraction scheme, meaning that 100% of the energy of a track was subtracted from the energy of the tower that the track intersected. Tower energies were then zero-suppressed after these subtractions were performed.

After jetfinding, events with two or more jets and a reconstructed vertex were examined for dijet candidates using the following algorithm for the full acceptance analysis. The analyses using different regions of phase space had different pseudorapidity acceptances for the pair of jets.

1. Remove events with $|z_{vertex}| > 80cm$.
2. Remove all jets with jet axis outside the acceptance: $-0.7 < \eta_{detector} < 0.7$.
3. Remove all jets with jet axis outside the acceptance: $-0.8 < \eta_{true} < 0.8$.
4. Remove all jets with a BEMC energy fraction outside of the range $0.05 < f_{BEMC} < 0.95$.
5. Choose the two jets with the highest p_T.
6. Check that $|\Delta\eta_{particle}| < 1.0$.
7. Check that the two jet axes are back to back: $|\Delta\phi| > 2.0$.
8. Apply the asymmetric jet p_T cut: $max(p_{T1}, p_{T2}) > 10$ (GeV/c) and $max(p_{T1}, p_{T2}) > 7$ (GeV/c).
9. Calculate the invariant mass of the two jets and increment histogram.

Table 6.1: Raw Dijet Yields for full acceptance analysis

Mass	N^{++}	N^{--}	N^{+-}	N^{-+}
20.0 - 30.0	389586.0	390418.0	384162.0	382411.0
30.0 - 40.0	105868.0	106531.0	104691.0	104276.0
40.0 - 50.0	21009.0	20776.0	20506.0	20495.0
50.0 - 60.0	4642.0	4497.0	4484.0	4512.0
60.0 - 70.0	1170.0	1142.0	1127.0	1075.0
70.0 - 80.0	314.0	292.0	306.0	295.0
80.0 - 100.0	120.0	107.0	111.0	104.0

Reconstructed Simulation Dijets

The simulation sample used for calculating the correction factors is described in Section 4.3.2 and the specific productions are outlined in Table 4.2. These events were reweighted so that the simulation dijet vertex distribution would match the data dijet vertex distribution for the same pseudorapidity acceptance.

The simulation went through exactly the same analysis as the data and very good agreement was seen between the dijet distributions for data and simulation (Fig. 6-1). This agreement motivated the use of the simulation for calculating the unfolding matrix and correction factors. The small discrepancies between the data and simulation in the η_{34} distribution were explained by additional pileup tracks that entered at higher luminosities. Figure 6-2 shows the difference between the data simulation comparison when the data were selected for being part of a high or low luminosity run.

6.2.1 Polarization

The polarizations for the blue and yellow beams were measured a few times during each fill using the CNI polarimeters, which were discussed in Chapter 2. These measurements had their absolute scale set by the Hydrogen-Jet polarimeter. The RHIC polarimetry group released the values for each fill, and these numbers were used in this analysis. The measurement technique is discussed in detail in [59].

The measurement of polarization and intensity profiles was done using the CNI

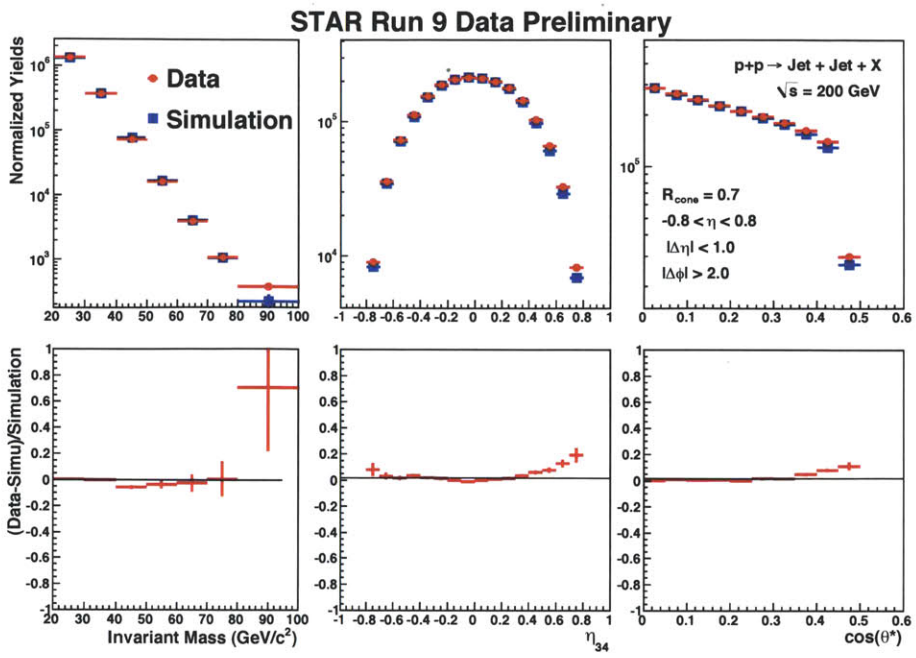

Figure 6-1: Agreement between the data and simulation for the 2009 analysis is good.

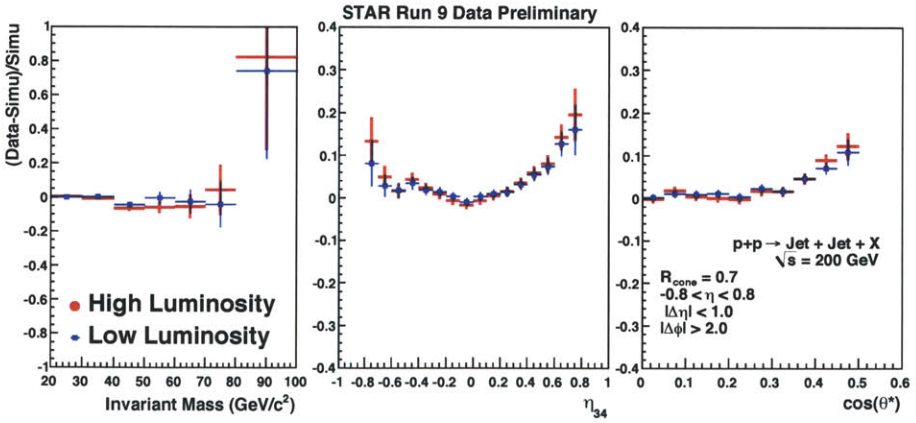

Figure 6-2: The difference in the data/simulation agreement between high and low luminosity data confirms that the small discrepancy in the η_{34} distribution was caused by pileup tracks, which entered more as luminosity increases.

Table 6.2: Run 9 200 GeV Polarizations and Uncertainties

	Polarization	**Total Uncertainty** $(d\delta P/P)$
Blue	59%	4.7%
Yellow	59%	4.7%
Combined	-	8.8%

polarimeters in scanning mode in both transverse directions. Using these profiles, the average polarization could be calculated according to the relation:

$$\langle P \rangle = \frac{P_{max}}{\sqrt{1+R}}, \tag{6.2}$$

where P_{max} was the maximum polarization measured in the profile and $R = (\sigma_I/\sigma_P)^2$, which was the squared ratio of the intensity profile width and the polarization profile width. These profiles were assumed to have gaussian shapes.

R could be extracted from measurements of the polarization and intensity using the relation

$$\frac{P}{P_{max}} = (\frac{I}{I_{max}})^R, \tag{6.3}$$

where P and I were specific measurements of the polarization and intensity. This method allowed the extraction of R without knowledge of the target position.

Multiple measurements per fill were averaged together using the luminosity profile measured for that fill. Figure 6-3 shows the values for $\langle P \rangle$ measured for the fills in Run 9. Systematic uncertainties for these measurements were limited by the understanding of the rate-dependent effects that were observed in the extraction of R at higher luminosities. This understanding also limited the ability to calculate the polarization decay time, which was used to calculate the average polarization over a fill. The overall uncertainties are described in Table 6.2.

6.2.2 Relative Luminosity

Ignorance of the difference between luminosities for like-sign bunch crossings relative to unlike-sign bunch crossings could result in the measurement of a false asymmetry.

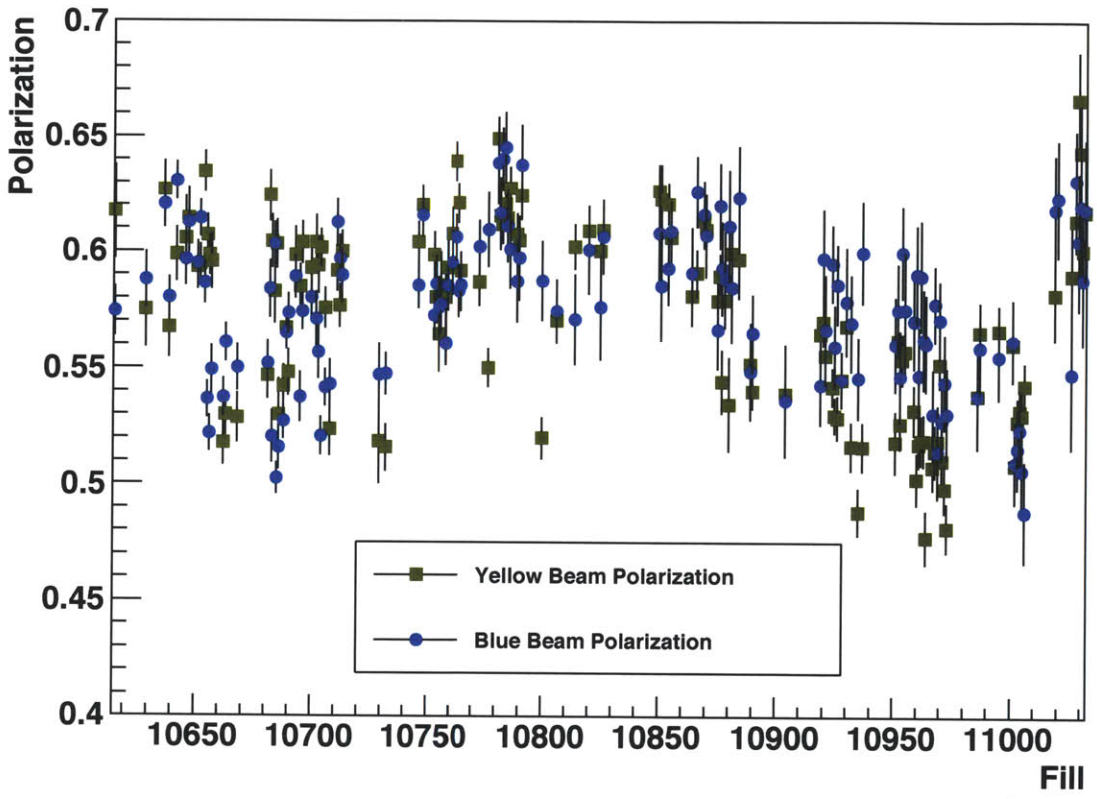

Figure 6-3: The polarizations for the blue and yellow beams as a function of fill with statistical uncertainties included.

Table 6.3: Relative Luminosity Definitions

$$R_1 = \frac{N^{++}+N^{+-}}{N^{-+}+N^{--}} \qquad R_4 = \frac{N^{++}}{N^{--}}$$
$$R_2 = \frac{N^{++}+N^{-+}}{N^{+-}+N^{--}} \qquad R_5 = \frac{N^{+-}}{N^{--}}$$
$$R_3 = \frac{N^{-+}+N^{+-}}{N^{++}+N^{--}} \qquad R_6 = \frac{N^{-+}}{N^{--}}$$

Luminosities for each bunch crossing were measured using a system of FPGAs called the scaler boards. These boards recorded the counts for a number of detectors, of which the BBC and ZDC were used for this analysis. The ability of the scaler boards to record pulses at the RHIC clock frequency allowed separation of signals from these detectors into the correct bunch crossing.

There were six ratios of the four possible spin states that were useful for measuring the double longitudinal spin asymmetry and various other asymmetries that were used as cross checks. These ratios are defined in Table 6.3.

The number of hard-scattering events in each spin state should be used to calculate the different relative luminosities. This results from taking the number of coincidences recorded in the scalers and correcting for the number of multiple collisions and accidental coincidences that likely occurred. A coincidence was when both the east and west detector modules were triggered within a time window. If it was caused by two different singles events triggering the two detectors in time, it was called an accidental. If it was actually more than one event that would have caused a coincidence, it was called a multiple. The accidentals correction reduced the overall coincidence rate, but the multiples correction increased it.

Using the information recorded in the scalers, the corrected coincidence rate could be calculated from the following relation:

$$\frac{N_{corr}}{N_{BC}} = -\ln(1 - \frac{N_{EW} - \frac{N_E N_W}{N_{BC}}}{N_{BC} + N_{EW} - N_E - N_W}), \tag{6.4}$$

where N_{corr} was the corrected number of coincidences, N_{BC} was the number of bunch crossings, N_{EW} was the number of recorded coincidences, and $N_{E(W)}$ was the number of single triggers recorded in the east (west) module of the detector. Both the rates

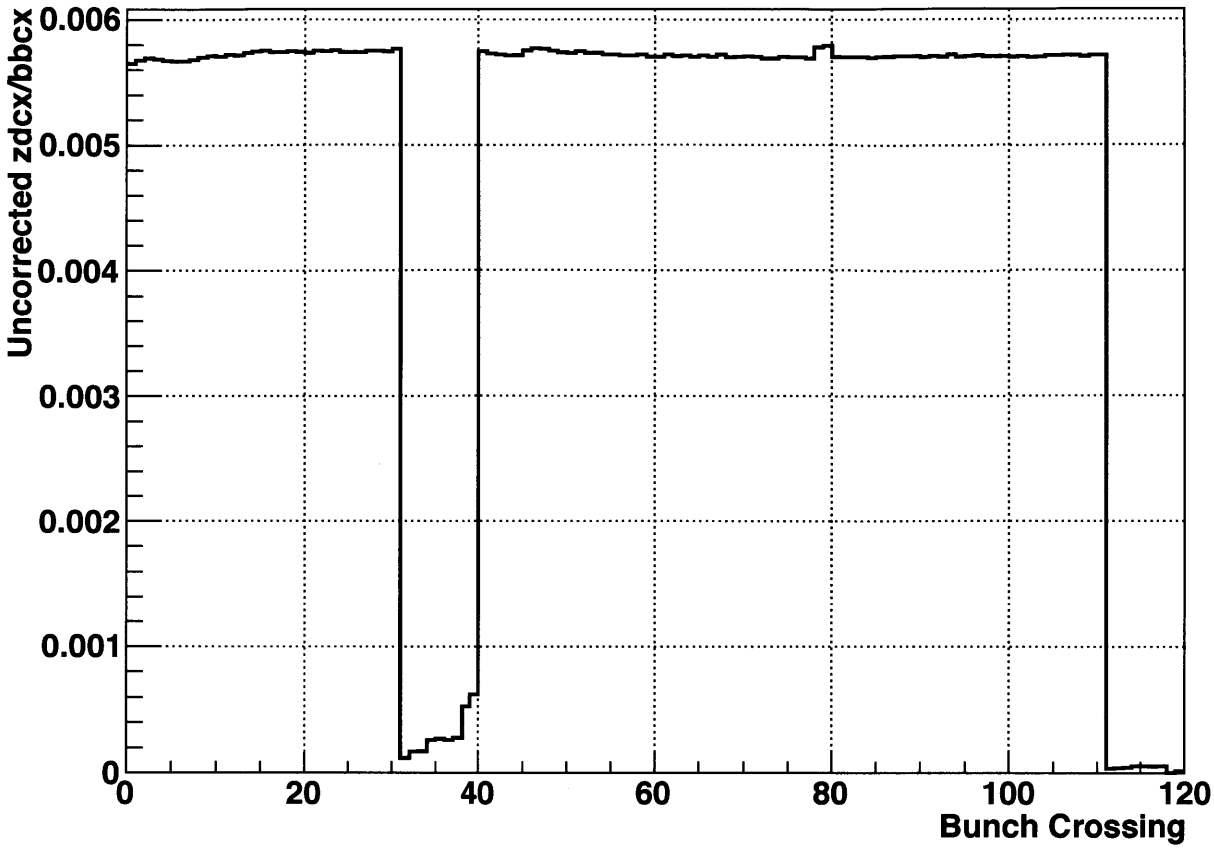

Figure 6-4: The ratio of the ZDC coincidence rate to the BBC coincidence rate before any corrections were applied as a function of bunch crossing.

from the ZDC and the BBC were corrected using the same scheme. A similar formula was used to correct the singles rates for modules of both detectors. Figure 6-4 shows the ratio of the ZDC coincidence rate to the BBC coincidence rate as a function of bunch crossing averaged over the entire run before the corrections were applied. After the corrections were applied in Figure 6-5, the ratio was much smoother. This figure also shows the two abort gaps (bunch crossings 31 to 39 and 111 to 119). The growing structure in the first abort gap shows that there was some beam background in those bunches.

The BBC coincidence rate was much higher than the ZDC rate, which can be seen from Fig. 6-4, so the statistical uncertainty on the relative luminosities calculated with its rates were much better. The average values and statistical uncertainties can

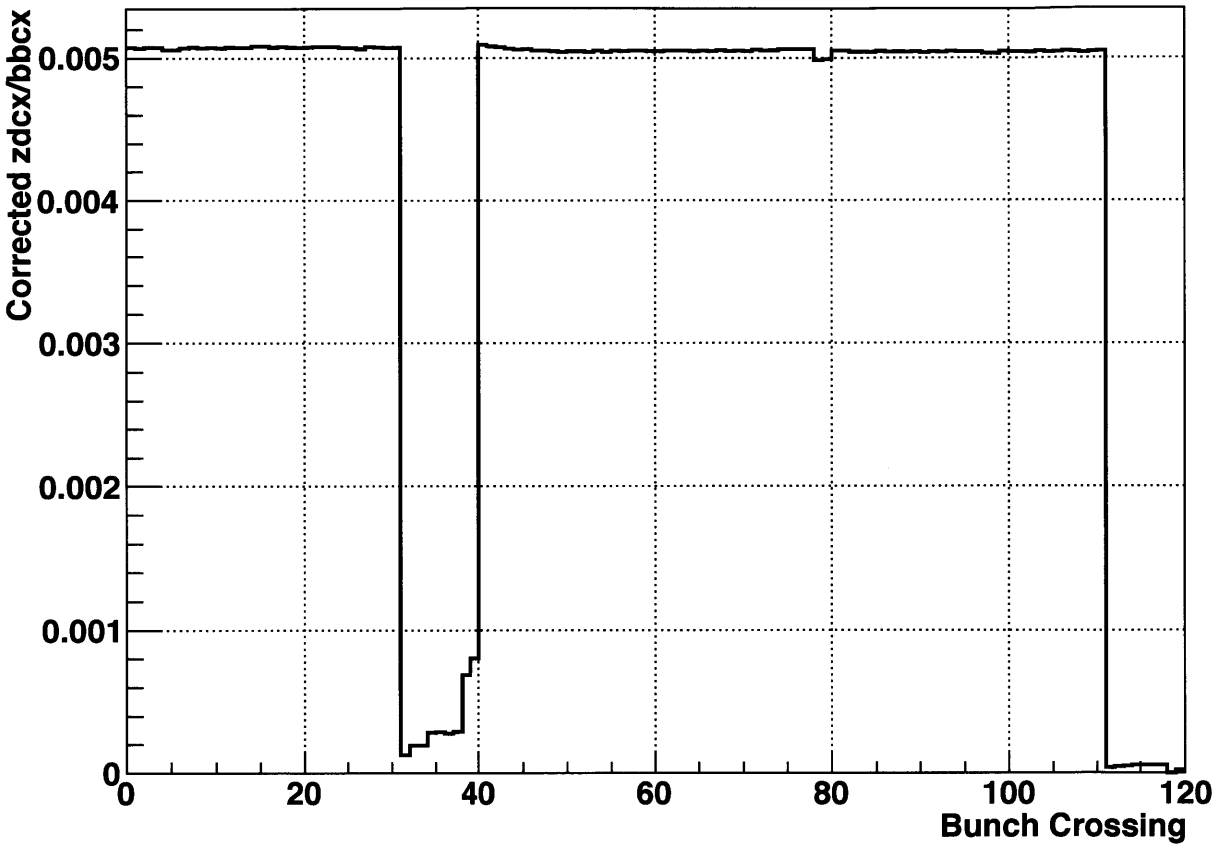

Figure 6-5: The ratio of the ZDC coincidence rate to the BBC coincidence rate after being corrected for the singles and multiples rates as a function of bunch crossing.

Table 6.4: Relative Luminosities and Uncertainties

Label	Mean value	Statistical Uncertainty	Systematic Uncertainty ($\delta R/R$)
R_1	1.003	9.62×10^{-5}	9.6×10^{-5}
R_2	0.995	9.54×10^{-5}	-7.4×10^{-6}
R_3	1.005	9.62×10^{-5}	1.7×10^{-4}
R_4	0.998	1.35×10^{-4}	8.3×10^{-5}
R_5	1.000	1.36×10^{-4}	-8.0×10^{-5}
R_6	0.992	1.35×10^{-4}	1.9×10^{-4}

Table 6.5: Bunch Crossings Removed from Analysis

Bunch Crossings	Reason for Removal
20, 60	Kicker bunches
31-39, 111-119	Abort gaps
78, 79, 80	Strange rate structure

be found in Table 6.4.

To understand the systematic uncertainty on the relative luminosities, the values of all six numbers were compared against the values calculated using the ZDC. The relative luminosities could be calculated using any of the corrected or uncorrected scaler quantities for each detector, and comparisons were made between many of these possibilities to understand various effects. The detailed studies are explained in [58].

The systematic analysis of the relative luminosity found systematic uncertainties approximately the same size as the statistical uncertainties (Table 6.4), a substantial improvement over previous years. The source of the improvement was the discovery that the ZDC west singles rate had a spin dependence, which would likely result in a spin dependence of the coincidence rate. The ZDC east rate was shown to have no spin dependence, so the systematic uncertainties were calculated by comparing relative luminosities from this rate and the BBC coincidence rate. The details can be found in [58]. A number of bunch crossings were removed from the analysis as a result of these studies (Table 6.5).

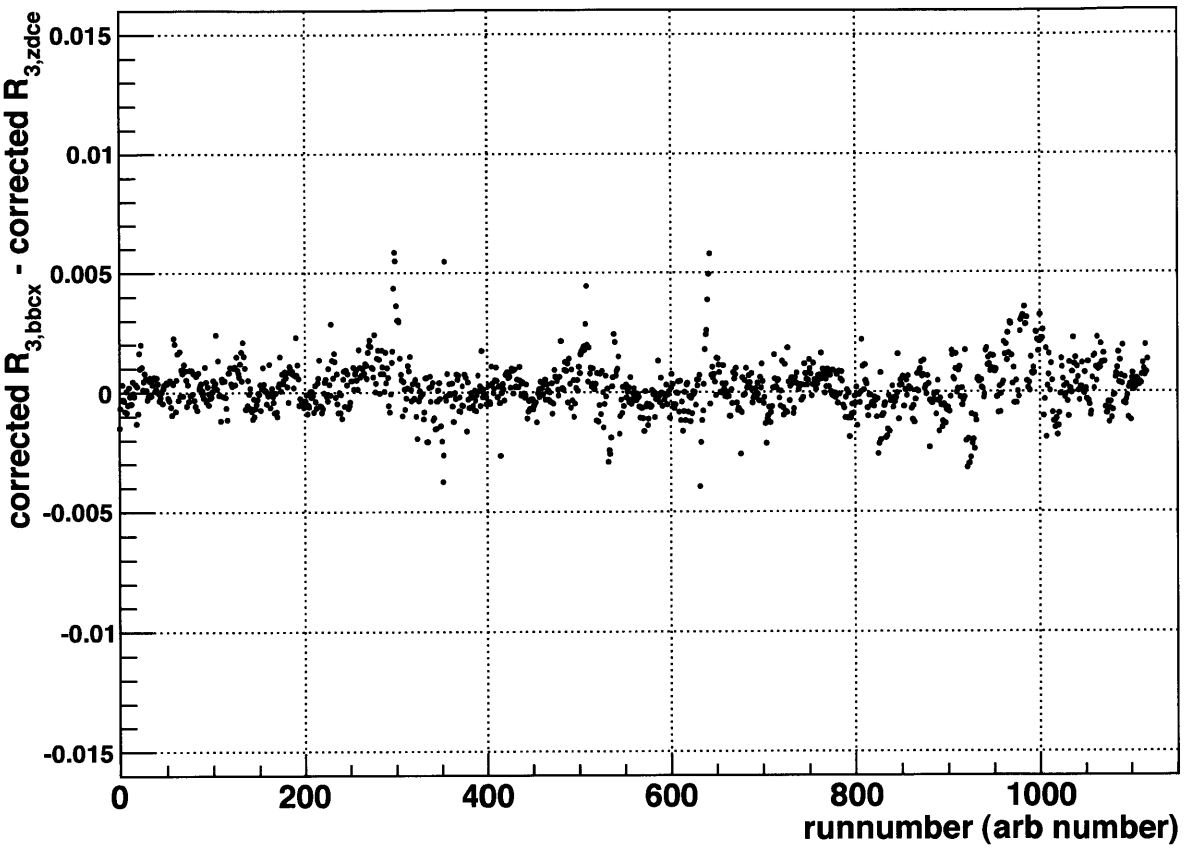

Figure 6-6: The difference between the R_3 values calculated using the BBC coincidence scaler and the ZDC East scaler shows very good agreement.

6.2.3 Unfolding Matrix

As in the cross section analysis, the unfolding matrix contained information about detector resolution in the analysis. Unlike for the cross section, this term in Eq. 6.1 also contained the information about the various efficiencies. The sum over matrix elements could be rewritten as

$$\sum_k \alpha_{jk} = \sum_k \frac{1}{\epsilon_j^{reco}} \widehat{\alpha}_{jk} \epsilon_k^{misreco}, \tag{6.5}$$

where ϵ_j^{reco} was the combined trigger, vertex, and reconstruction efficiency, $\widehat{\alpha}_{jk}$ was the unfolding matrix, and $\epsilon_k^{misreco}$ was the misreconstruction efficiency. In this prescription, the unfolding matrix was determined using events that had a detector level dijet that also satisfied the trigger and a particle level dijet. This differed from the cross section analysis, which did not require the trigger on the detector level dijet when the unfolding matrix was calculated. This change reduced the overall number of efficiencies that were calculated. The values for the misreconstruction efficiency in each bin can be found in Table 6.6 and the values for the reconstruction efficiency can be found in Table 6.8.

The two matrices α and β in Eq. 6.1 were for the like sign and unlike sign spin states, respectively. The details of separating the simulation into spin sorted yields is discussed in detail in Appendix F. The purpose of this separation was to remove one source of systematic uncertainty: the fact that the different gluon polarization scenarios come with different effects on the trigger uncertainty. Separate unfolding matrices could be calculated for each of the theory scenarios and used when the data was compared to the specific A_{LL} calculations. The values of the summed unfolding matrix can be seen in Table 6.7. However, in the plots shown here, the unpolarized unfolding matrix was used, with a systematic uncertainty assigned to the scenario differences for display purposes.

Table 6.6: Misreconstruction Efficiency

Mass	$\epsilon_k^{misreco}$
20.0 - 30.0	0.89
30.0 - 40.0	0.95
40.0 - 50.0	0.97
50.0 - 60.0	0.98
60.0 - 70.0	0.99
70.0 - 80.0	1.00
80.0 - 100.0	0.92

6.3 Statistical Uncertainties

We could calculate the diagonal values of the covariance matrix (excluding statistical uncertainties on the matrix elements):

$$\begin{aligned}
U_j &= \sum_k \sum_i P_{B,i} P_{Y,i} \alpha_{jk} (N_{5,i,k} + N_{10,i,k}) - \sum_k \sum_i P_{B,i} P_{Y,i} R_i \beta_{jk} (N_{6,i,k} + N_{9,i,k}) \\
D_j &= \sum_k \sum_i P_{B,i}^2 P_{Y,i}^2 \alpha_{jk} (N_{5,i,k} + N_{10,i,k}) + \sum_k \sum_i P_{B,i,j}^2 P_{Y,i,j}^2 R_i \beta_{jk} (N_{6,i,k} + N_{9,i,k}) \\
\sigma_{A_{LL,j}}^2 &= \sum_k \sum_i \left(\frac{D_j P_{B,i} P_{Y,i} \alpha_{jk} - U_j P_{B,i}^2 P_{Y,i}^2 \alpha_{jk}}{D_j^2}\right)^2 (N_{5,i,k} + N_{10,i,k}) \\
&\quad + \sum_k \sum_i \left(R_i \frac{D_j P_{B,i} P_{Y,i} \beta_{jk} - U_j P_{B,i}^2 P_{Y,i}^2 \beta_{jk}}{D_j^2}\right)^2 (N_{6,i,k} + N_{9,i,k})
\end{aligned} \tag{6.6}$$

However, there was not any way to calculate the full covariance matrix for A_{LL} in closed form. It was instead possible to calculate the covariance matrix using a Monte Carlo method. Recall

$$\begin{aligned}
cov(\mathbf{X}) &= \langle (\mathbf{X} - \langle \mathbf{X} \rangle)(\mathbf{X} - \langle \mathbf{X} \rangle)^T \rangle \\
cov(\mathbf{X})_{ij} &= \langle (X_i - \mu_i)(X_j - \mu_j) \rangle
\end{aligned} \tag{6.7}$$

Given the statistical uncertainties for each $N_{5(,6,9,10),i,k}$, the statistical uncertainties on each R_i, and the statistical uncertainties on each $P_{B(Y),i}$, it was possible to generate a large number of $\{A_{LL,j}\}$, which could be used to calculate the covariance. To do this calculation, the analysis was run 1,000 times, sampling against the data in each bin

Table 6.7: Unfolding Matrix

M_{reco}	-10.0	0.0	10.0	15.0	20.0	30.0	40.0	50.0	60.0	70.0	80.0	100.0	165.0
) - 0.0	0.00	0.00	0.00	0.00	0.00	0.00	0.00	0.00	0.00	0.00	0.00	0.00	0.00
- 10.0	0.00	0.00	0.00	0.00	0.00	0.00	0.00	0.00	0.00	0.00	0.00	0.00	0.00
- 15.0	0.00	0.00	0.00	0.00	0.00	0.00	0.00	0.00	0.00	0.00	0.00	0.00	0.00
- 20.0	0.00	0.00	0.00	0.13	0.01	0.00	0.00	0.00	0.00	0.00	0.00	0.00	0.00
- 30.0	0.00	0.00	0.00	0.84	0.73	0.07	0.00	0.00	0.00	0.00	0.00	0.00	0.00
- 40.0	0.00	0.00	0.00	0.03	0.25	0.69	0.09	0.01	0.00	0.01	0.00	0.00	0.00
- 50.0	0.00	0.00	0.00	0.00	0.01	0.22	0.65	0.10	0.01	0.00	0.00	0.00	0.00
- 60.0	0.00	0.00	0.00	0.00	0.00	0.02	0.23	0.61	0.13	0.01	0.00	0.00	0.00
- 70.0	0.00	0.00	0.00	0.00	0.00	0.00	0.02	0.24	0.55	0.11	0.00	0.00	0.00
- 80.0	0.00	0.00	0.00	0.00	0.00	0.00	0.00	0.04	0.24	0.55	0.09	0.00	0.00
- 100.0	0.00	0.00	0.00	0.00	0.00	0.00	0.00	0.00	0.05	0.32	0.91	0.27	0.00
- 165.0	0.00	0.00	0.00	0.00	0.00	0.00	0.00	0.00	0.01	0.00	0.00	0.73	0.00
- 600.0	0.00	0.00	0.00	0.00	0.00	0.00	0.00	0.00	0.00	0.00	0.00	0.00	0.00

Table 6.8: Reconstruction Efficiency

Mass	ϵ_j^{reco}
20.0 - 30.0	0.03
30.0 - 40.0	0.15
40.0 - 50.0	0.27
50.0 - 60.0	0.31
60.0 - 70.0	0.31
70.0 - 80.0	0.30
80.0 - 100.0	0.21

for each run, the relative luminosities, the polarizations, and the counts in the matrix used for the unfolding to generate the complete covariance matrix in a manner that took all of the correlations across runs and fills into account consistently.

6.4 Systematic Uncertainties

The systematic uncertainty techniques used here were very similar to those used in the cross section analysis. The main sources of uncertainty were the polarization, the relative luminosity, any transverse asymmetry, and jet energy scale uncertainties. The polarization uncertainty, which is annotated in Table 6.2 as the combined uncertainty, introduced an overall scale uncertainty in the asymmetry.

The relative luminosity systematic uncertainty introduced a false asymmetry in the limit that $A_{LL} = 0$, but since that condition did not hold in all bins, the effect of the relative luminosity systematic uncertainty was calculated by moving all of the relative luminosities up and down before running the analysis. Each bin of A_{LL} was then compared with the nominal value to find the value used for this uncertainty.

False asymmetries could also enter if there was a spin dependence of the jet trigger or in the BBC trigger used to calculate the relative luminosities. To check that dependence, a variety of additional asymmetries were calculated. Those asymmetries are described in Table 6.9. Note that the relative luminosities are defined in Table 6.3. The values of each of these asymmetries were consistent with zero before (Fig. 6-7) and after (Fig. 6-8) unfolding, which led to the conclusion that the spin dependence

Table 6.9: Description of False Asymmetries

Asymmetry	Formula	Description
A_{yb}	$\frac{\sum P_Y((N^{++}+N^{+-})-R_1(N^{-+}+N^{--}))}{\sum P_Y^2((N^{++}+N^{+-})+R_1(N^{-+}+N^{--}))}$	Yellow Beam single spin asymmetry
A_{bb}	$\frac{\sum P_B((N^{++}+N^{-+})-R_2(N^{+-}+N^{--}))}{\sum P_B^2((N^{++}+N^{-+})+R_2(N^{+-}+N^{--}))}$	Blue Beam single spin asymmetry
A_{ls}	$\frac{\sum P_Y P_B(N^{++}-R_4N^{--})}{\sum P_Y^2 P_B^2(N^{++}+R_4N^{--})}$	Like-sign asymmetry
A_{us}	$\frac{\sum P_Y P_B(R_6N^{+-}-R_5N^{-+})}{\sum P_Y^2 P_B^2(R_6N^{+-}+R_5N^{-+})}$	Unlike-sign asymmetry

of the L2 jet and BBC triggers contributed negligible false asymmetries.

Because the polarization of proton beams was not perfectly longitudinal, which means there was a small transverse component, there was sensitivity to transverse physics. To account for the possibility of non-longitudinal physics shifting A_{LL}, a systematic uncertainty was assigned to the non-longitudinal polarization of the beam. The value of the systematic uncertainty was 0.025 times the value of A_{LL} in each bin, which was a scaling to the average ratio of transverse polarization to longitudinal polarization over the run.

To account for the jet energy scale uncertainties, different unfolding matrices, which contain all of the information about the effects of the jet energy scale, were calculated for different sources of uncertainty.

The BEMC introduced uncertainty from the overall scale uncertainty and the uncertainty in the simulation model of transverse shower effects. The magnitude of these effects were both 2% on the energy calculated for a given volume. The value for the energy scale uncertainty was calculated as part of the BEMC calibration (Appendix A) and the value for the simulation comes from studies of π^0 mass reconstruction in data and simulation [60]. The treatment was the same as for the cross section; the corresponding status tables were varied independently, resulting in eight possible unfolding matrices. Each was used to calculate a new set of A_{LL} values and the most extreme were used for this contribution of the systematic uncertainty.

The TPC introduced uncertainty from the overall scale uncertainty and the track finding efficiency. From studies of the BEMC calibration (Appendix A), it was determined that there is a larger than usual scale uncertainty in the TPC of approximately

2%, which was needed to explain the difference between the behavior of different charged electrons. The standard track finding efficiency uncertainty of 5% was used, which was well documented from previous years. To account for these effects, a procedure completely analogous to the treatment of the BEMC uncertainties was used. Both effects were varied independently, resulting in eight new unfolding matrices. Again, each was used to calculate a new set of A_{LL} values and the most extreme were used for this contribution of the systematic uncertainty.

For the purposes of visual comparison, a systematic uncertainty was assigned to the asymmetry to account for the differences in unfolding caused using an unpolarized unfolding matrix instead of the various polarized unfolding matrices. This uncertainty was assessed by generating simulated data from various theory scenarios and comparing the result from unfolding using the unpolarized matrix and using the polarized matrices calculated for that scenario. The differences in the unfolding for three scenarios can be seen in Fig. 6-9. The largest difference in each bin in each direction from zero was used as the uncertainty.

All of these effects were combined in quadrature. The contributions and totals are shown in Table 6.10.

6.5 Theory Calculation

Code for the theory calculations of the various theory scenarios was provided by de Florian. Changes were again made to match the binning and various acceptances used in this analysis. The code produced a polarized and unpolarized cross section, the ratio of which is A_{LL}. Some theory scenarios were not available in the NLO code and had to be generated using PYTHIA weighting.

6.6 Results

Figure 6-10 shows the longitudinal double spin asymmetry for the Run 9 data set using the full acceptance of the STAR detector. The data points with statistical

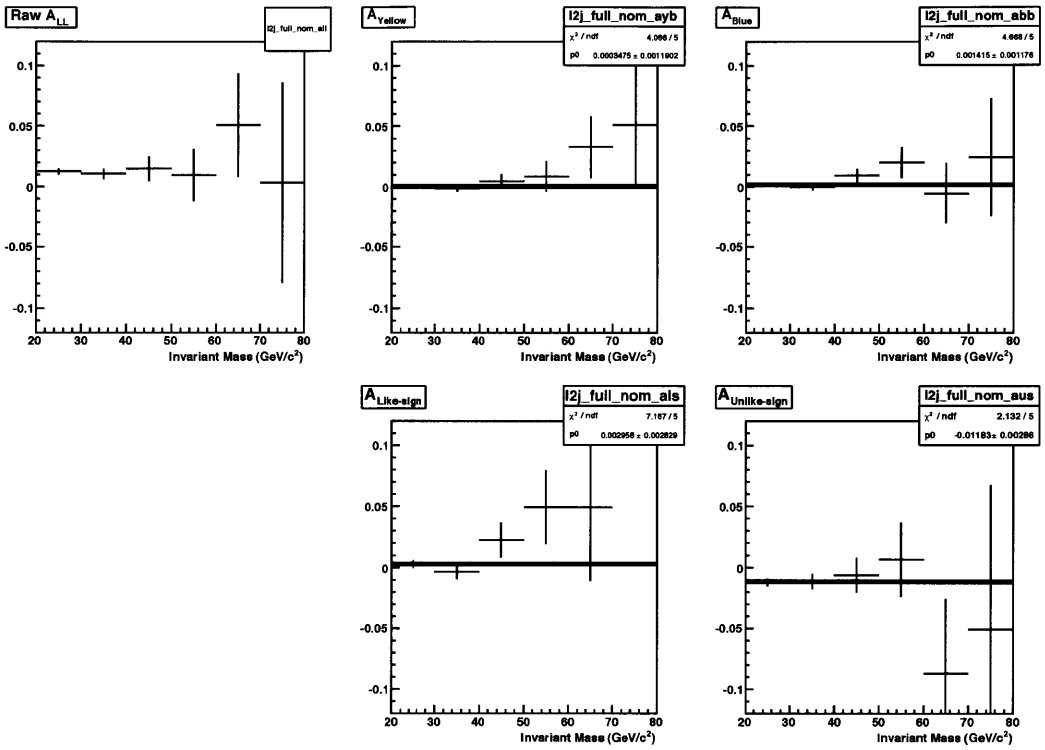

Figure 6-7: The so-called false asymmetries were consistent with zero, which improved confidence that there was no spin dependent effect in the triggering and relative luminosity calculations.

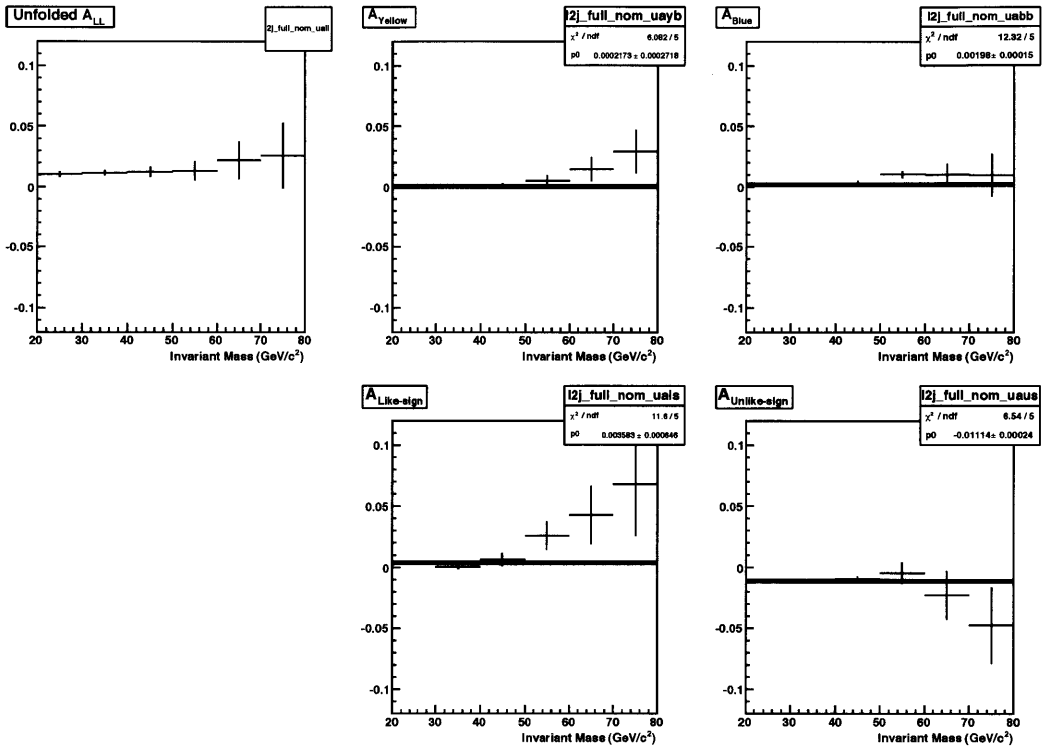

Figure 6-8: The false asymmetries remained consistent with zero, perhaps even improving consistency, after unfolding, which improved confidence that the procedure did not bias the asymmetry calculation.

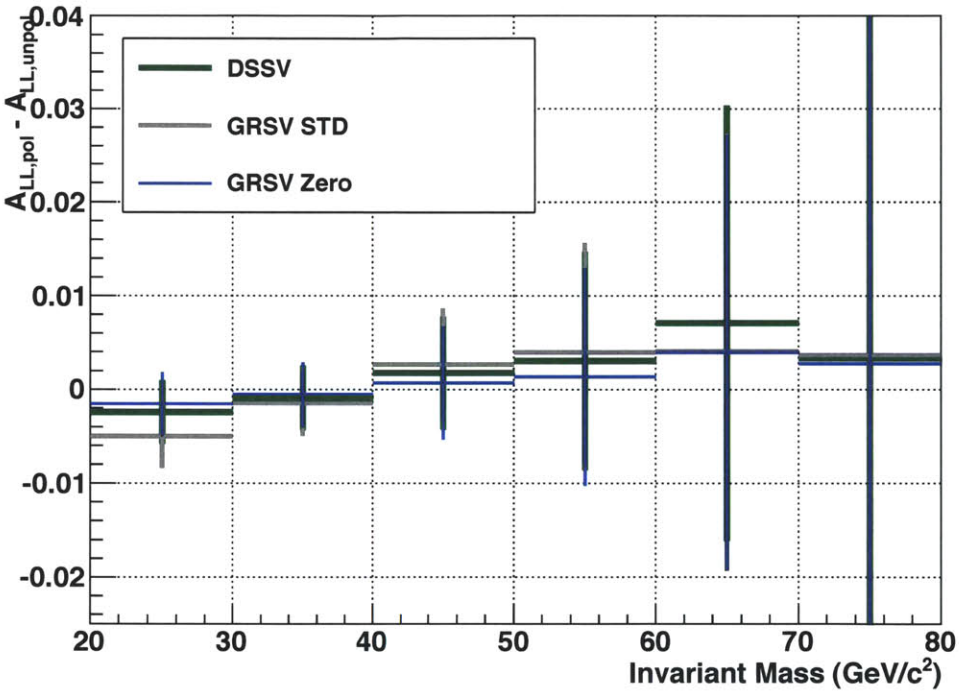

Figure 6-9: Comparisons of the unpolarized unfolding with the polarized unfolding for different theory scenarios were used to calculate an uncertainty for visual comparison between the asymmetry and multiple theory curves.

Table 6.10: Systematic Uncertainty Contributions

Mass	**BEMC+**	**BEMC-**	**TPC+**	**TPC-**	**Non-Long.**	**Rel. Lumi. +**	**Rel. Lumi -**	**Total+**	**Total-**
20.0 - 30.0	3.96e-04	1.48e-04	7.14e-05	6.54e-04	2.57e-04	2.43e-04	2.43e-04	5.36e-04	7.59e-04
30.0 - 40.0	2.24e-05	8.01e-04	7.37e-05	2.60e-04	2.88e-04	2.43e-04	2.43e-04	3.84e-04	9.23e-04
40.0 - 50.0	2.19e-05	5.00e-04	4.04e-04	4.53e-04	3.03e-04	2.42e-04	2.43e-04	5.61e-04	7.78e-04
50.0 - 60.0	4.41e-03	0.00e+00	5.56e-03	0.00e+00	3.26e-04	2.42e-04	2.43e-04	7.11e-03	4.06e-04
60.0 - 70.0	4.58e-03	0.00e+00	8.04e-03	0.00e+00	5.45e-04	2.42e-04	2.42e-04	9.27e-03	5.96e-04
70.0 - 80.0	0.00e+00	1.60e-02	9.26e-03	1.80e-02	6.39e-04	2.42e-04	2.42e-04	9.28e-03	2.42e-02
80.0 - 100.0	0.00e+00	2.63e-02	0.00e+00	2.82e-02	8.26e-04	2.43e-04	2.43e-04	8.61e-04	3.86e-02

uncertainties in black have been unfolded to account for detector effects in the reconstruction of the dijet invariant mass. The yellow uncertainty bands represent the systematic uncertainties. The gray curve represents the expected asymmetry calculated using the best fit for $\Delta g(x)$ from DIS data, known as GRSV std. The green curve represents the expectations from a fit that included the first RHIC data, DSSV. Finally, the magenta curve represents the DNS scenario.

Since different detector acceptances constrain the leading order parton kinematics (Figure 6-11 shows where the data samples $x_1 - x_2$ space), additional analysis has been performed by dividing the dijet sample into two sets:

1. Dijets with both jets falling in the same half of the BEMC acceptance (east barrel - east barrel and west barrel - west barrel),

2. Dijets with the two jets falling in opposite halves of the BEMC acceptance (east barrel - west barrel).

Figure 6-10 shows the longitudinal double spin asymmetry for these two acceptances. Again the data with statistical uncertainties are shown in black and the systematic uncertainties are in yellow. DSSV and GRSV std are shown in green and gray, respectively, with their scale uncertainties. A calculation from GS-C is shown in pink, which was generated using a Monte Carlo generator with asymmetry weights.

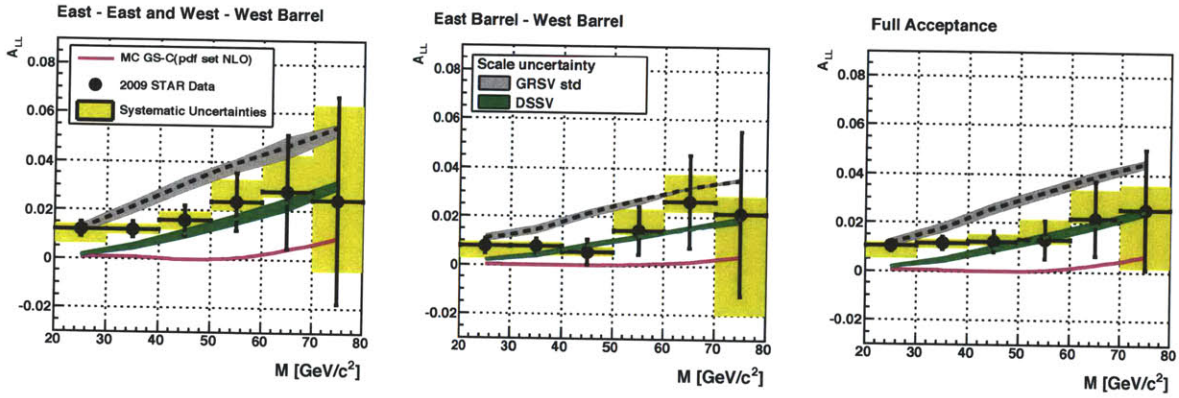

Figure 6-10: The final longitudinal double spin asymmetry with comparisons to various theory scenarios including statistical and systematic uncertainties. The difference panels are the different acceptances: same side jets on the left, opposites side jets in the middle, and the full acceptance on the right.

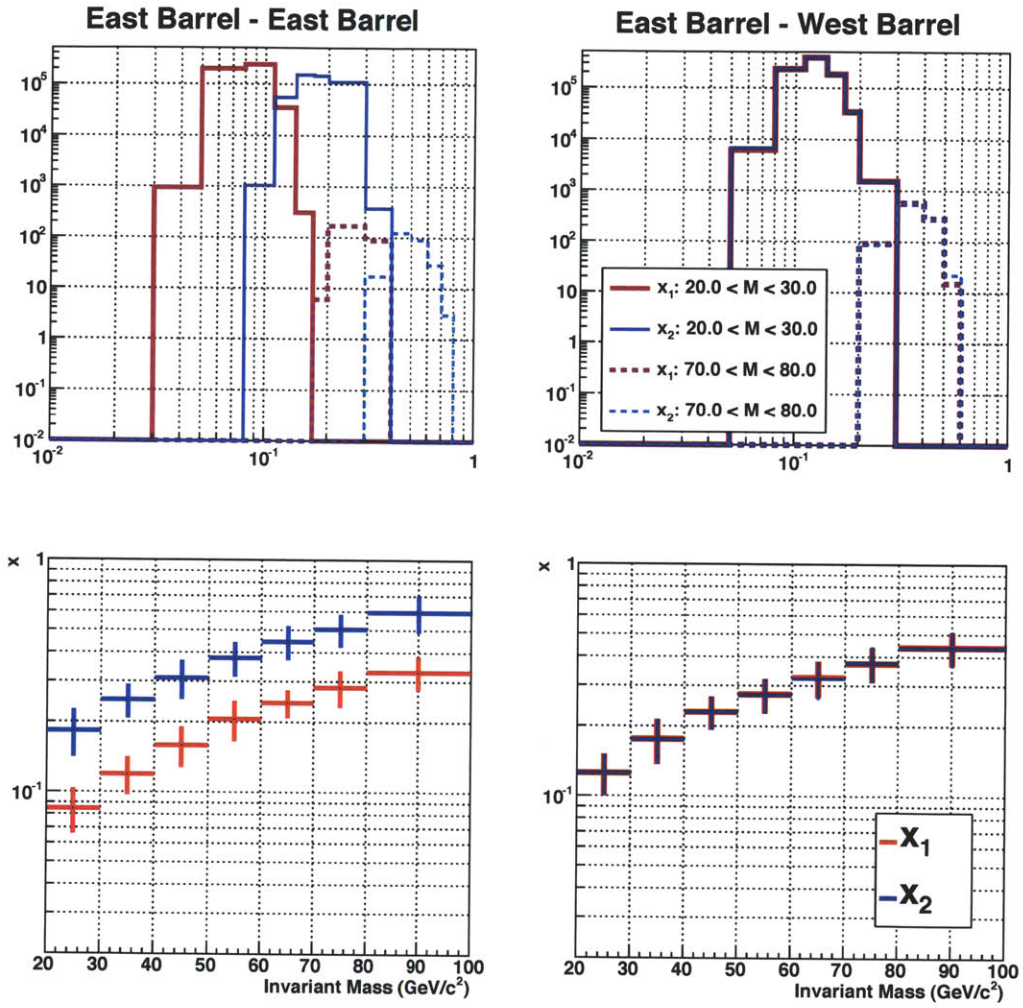

Figure 6-11: The leading order sensitivity to the parton kinematics (in the form of Bjorken-x) is different for the various mid-rapidity acceptances, which allows constraints to be placed on the shape of $\Delta g(x)$. The left two panels show distributions for dijets with both jets on the east side of the BEMC and the right two panels show distributions for one jet on each side of the BEMC. The top panels show the x_1 and x_2 distributions for two mass bins and the the bottom panels show the mean and RMS of the x_1 and x_2 distributions for each bin.

Chapter 7

Conclusions

Despite early hopes that data from RHIC would reveal a large gluon contribution to the proton spin, recent results have found that the gluon polarization is small in the Bjorken-x region accessible at RHIC. The range of fits from GRSV [13], which were made before any RHIC data was taken, covered the range of $-1.8 < \Delta G < 1.9$. The best fit from DIS data from GRSV suggested $\Delta G \sim 0.4$. Under the fit obtained from DSSV, which included RHIC results for the first time, $\Delta G \sim -0.08$ and suggests an asymmetry similar to GRSV "zero," which leads to $\Delta G \sim 0.1$. The GS-C scenario proposed by Gehrmann and Stirling [61] is notable for producing a low A_{LL} in the RHIC sensitivity region, but a nonetheless large overall $\Delta G = 1.02$.

Comparison of the results of this thesis to standard theory scenarios suggests a preference for the DSSV result. The GRSV-std and GS-C scenarios are definitively excluded for the first time.

This analysis of dijets provides for the first time constraints on the shape of $\Delta g(x)$. These constraints are vital as the uncertainties on the shape of $\Delta g(x)$ grow substantially as the lower x region is approached. By separating the dijet yields into different acceptances, different areas of initial parton phase space are accessible (Fig. 6-11).

Future work will extend the areas of phase space accessible to STAR by extending the dijet to other calorimeters. The Endcap Electromagnetic Calorimeter (EEMC) covers the pseudorapidity range $1.08 < \eta < 2.0$ and the Forward Meson Spectrometer

(FMS) covers the range $2.5 < \eta < 4.0$. By finding dijets in these detectors, even lower values of x will be accessible, and making dijets in the various combinations of the BEMC, EEMC, and FMS makes mapping $\Delta g(x)$ an exciting possibility.

Recent efforts at RHIC to extend polarized proton collisions to $\sqrt{s} = 500$ GeV present another opportunity for extending the x regime in which $\Delta g(x)$ can be explored. Recalling from Chap 1 that the reconstructed Bjorken-x values are proportional to $1/\sqrt{s}$, this region is extended by a factor of 2.5. However, most theory scenarios predict smaller asymmetries in this x range.

In the farther future, a polarized electron-ion collider (EIC) will probe a wider range of gluon kinematics with higher precision [62]. Plans are already underway to design the accelerator and develop the technologies needed to deliver the luminosities required for such an experiment and detector development proposals are also being drafted. Experiments at this facility will be able to extend and refine the measurements of this analysis and others to improve the understanding of $\Delta g(x)$.

Given the small values of ΔG suggested by recent RHIC results, it seems natural to look to orbital angular momentum as another source of the proton spin. Though lattice calculations of the up and down quark orbital angular momentum suggest a disappointing cancellation, efforts are underway to find ways to measure Generalized Parton Distributions (GPDs) which should have sensitivity to the total angular momentum of the quarks and gluon [63]. However, since GPDs and lattice calculations are made with respect to a sum rule that does not have an explicit ΔG, it is challenging to reconcile the results of these analyses with the RHIC results. With the many different experiments on the horizon probing different ideas, the field of nucleon spin physics remains an exciting area of study.

Appendix A

Calibration of the BEMC

The Barrel Electromagnetic Calorimeter (BEMC) is the primary device for electromagnetic energy reconstruction in STAR. The physical structure is discussed in Chap. 2. The calibration of the 4800 towers and the characterization of the uncertainty on that calibration for the data taken 2006 and 2009 is discussed in this appendix.

A.1 2006 Methods

The first step in the calibration was to calculate the pedestals for each channel. This took a relatively small amount of data, which made fine time granularity simple to accomplish. Over 100 pedestal tables were generated for the 2006 data set and about 180 tables were made for the 2009 data.

Calibration code then extracted tracks from the entire data set with some minimal quality and momentum cuts. The first round of the calibration targeted tracks that may correspond to MIPs, which were used to find the relative calibration of each tower. The MIP energy deposit had the following functional form, which was determined from test beam data and simulations [46]:

$$MIP = (264 \pm 4_{stat} \pm 13_{sys} MeV) \times (1 + 0.056\eta^2)/\sin\theta. \quad \text{(A.1)}$$

From this relation we expected to see a peak approximately 20 ADCs above pedestal,

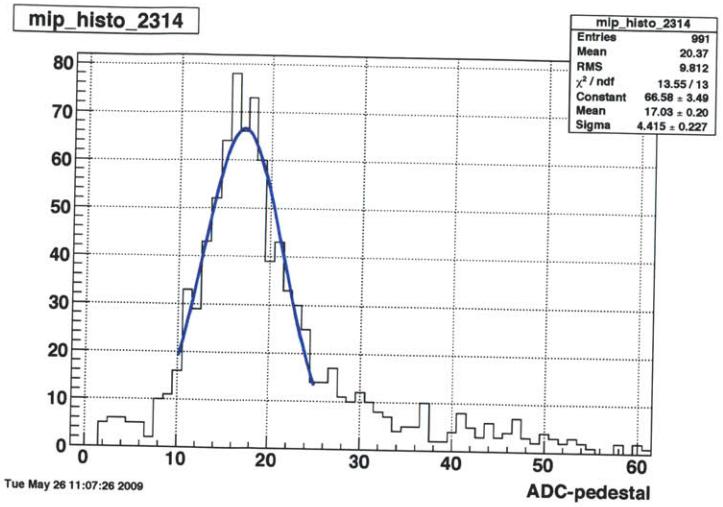

[h]

Figure A-1: The MIP peak for each tower was fit with a gaussian (in blue) and the value of the peak position was used to provide the relative calibration between towers.

shown in Fig. A-1. To find this peak, we looked at tracks with $p > 1$ GeV that entered and exited the same tower. We also required that no other tracks were incident on the same tower and that there was no high energy deposition on neighboring towers. These cuts helped ensure that the only energy in the tower was from the MIP deposition and that most of the MIP energy was in just one tower. In some towers, it was not possible to locate a MIP peak. The cause could be dead PMTs, mapping errors, or other hardware failures.

Once the MIP peak was found, we could calculate a calibration constant for a tower using the MIP energy value in Eq. (A.1) according to

$$C = \frac{0.264}{MIP_{ADC}} \frac{1 + 0.056\eta^2}{\sin\theta} \tag{A.2}$$

where $E = C \times (ADC - ped)$. These preliminary calculations were used to set the scale for comparing all of the towers at a given η. Using these values, we went back through our tracks and look for those that looked like electrons. We could use dE/dx

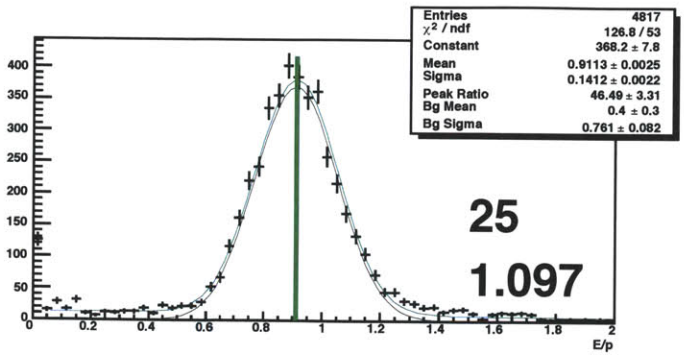

Figure A-2: The electron E/p spectrum for one of the rings showing the correction applied for that ring to the absolute energy scale. This figure has electrons from the entire calibration data sample.

to separate electrons from charged hadrons. Electron tracks were combined in η rings to find the absolute energy scale using E/p.

The cuts on electrons were more stringent than those used for the MIPs. Electron selection was performed using a cut at $nSigmaElectron > -1.0$. Furthermore, $nHits > 10$ was required to improve track quality and $1.5 < p(GeV) < 20$ ensured track momentum did not have any serious uncertainties. Here, the track momentum was taken from the momentum at the vertex. Finally, tracks projections were required to exit the same tower they entered to maximize shower containment in a single tower. There was some shower leakage as a function of distance between the center of the tower and where the track strikes the face. This leakage was corrected using GEANT modeling.

Electrons that struck towers at a given pseudo-rapidity were added together (120 towers in each of 40 rings). For each ring, E/p was fit and the deviation from 1 was considered the correction to the absolute scale for that ring. Corrections were relatively constant at mid-rapidity at 10% (see Fig. A-2), but increased to 45% at $|\eta|$ near 1.0. This variation was attributed to the increased material between the TPC and the front of the calorimeter tiles in this region, which caused showers to begin earlier and allowed some energy to escape capture in the tower. The corrections calculated were then applied to each of the calibration constants calculated for each tower to reach the final calibration for 2006.

The energy in a given tower could thus be described by

$$E = \frac{C_{e^{\pm}}(\eta)}{\sin\theta} \frac{0.264 \times (1 + 0.056 \times \eta^2)}{MIP_{ADC}(softId)} \times (ADC - ped), \tag{A.3}$$

where $C_{e^{\pm}}$ was the correction factor calculated for each η ring and $MIP_{ADC}(softId)$ was the MIP peak location for each tower. It was critical to note that the calibration coefficient was not sensitive to the uncertainty in the MIP energy deposit.

A.2 2006 Uncertainty

To characterize the uncertainty, we examined the effect of a wide range of parameters. After making an analysis on each parameter, we added a condition that would reduce the bias to an insignificant level. After all of these conditions were added, we once again measured the deviation of E/p from 1 and found that to be the bias in the calibration. This procedure resulted in a systematic bias of 1.6%.

We found that the most significant bias was introduced by trigger sculpting in high tower (HT) and high tower trigger patch (HTTP) events. The trigger conditions in these events were thresholds in tower ADCs that must be passed. Near the threshold, this condition selected electrons with high E/p. We compared separately events that had a HT/TP trigger (Fig. A-3(a)) and those that did not (Fig. A-3(b)). This effect introduced an uncertainty of 1.3% and is shown in Fig. A-4.

Discussions held at the BEMC Calibrations Workshop indicated that the momentum from the track's outer helix should be used instead of the momentum at the vertex to account for radiative energy loss. This momentum was used for the uncertainty analysis.

Over the momentum range available in this study, there was evidence that the detector was linear up to approximately 5 GeV/c, as shown in Fig. A-5. Extrapolations to higher energies were challenging in this method as statistics and TPC momentum uncertainties begin.

The GEANT correction used to model the transverse leakage was produced using

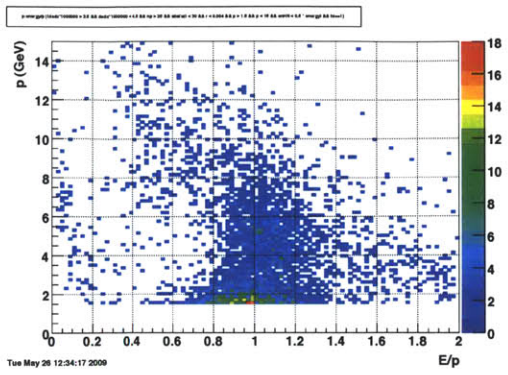

[ht]

(a) HT/TP events

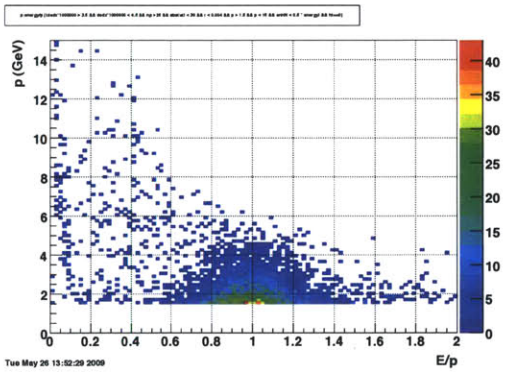

(b) non-HT/TP events

Figure A-3: This plot of track momentum p vs. E/p for electrons from HT/TP events shows that there was a clear momentum dependence of E/p for these electrons. Notice the curve in the spectrum and that it began before the area where the momentum reach of the non-HT/TP events falls off. That dependence had disappeared when we look at electrons for non-HT/TP events. Even though the momentum reach was reduced, the curve had clearly disappeared. These plots only used the restricted data sample.

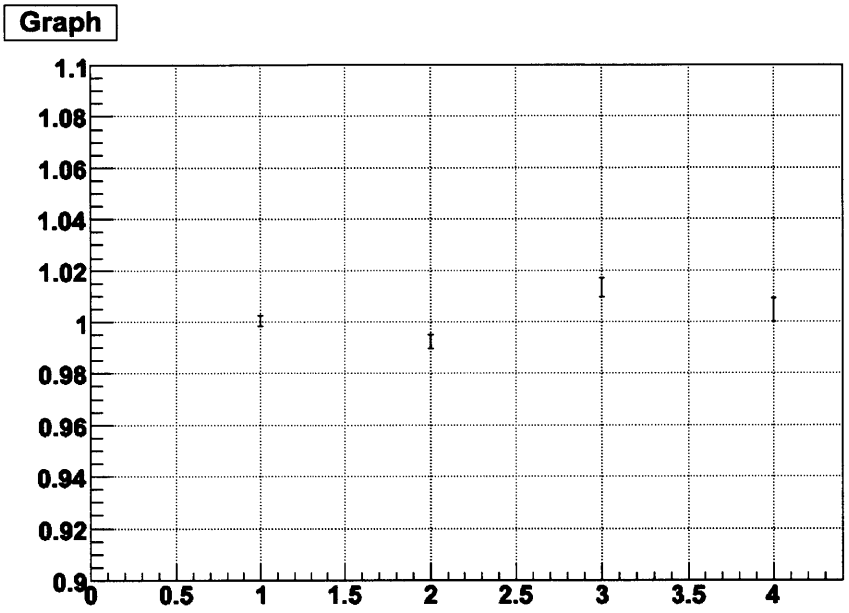

Figure A-4: Four different cut scenarios were looked at after all stringent cuts were applied to determine the systematic uncertainty due to the trigger bias. The y-axis of this plot is E/p and the points represent one of the scenarios. Scenario 1 was all of the electrons after stringent cuts. Scenario 2 was electrons from events that were non-HT/TP triggered. Scenario 3 was electrons from events that were HT/TP triggered. Scenario 4 was electrons from HT/TP events with tracks from the trigger turn-on region ($4.5 < p < 6.5$ GeV/c) removed. The largest difference from here, which corresponded to Scenario 3 defined the uncertainty from the trigger bias at 1.3%.

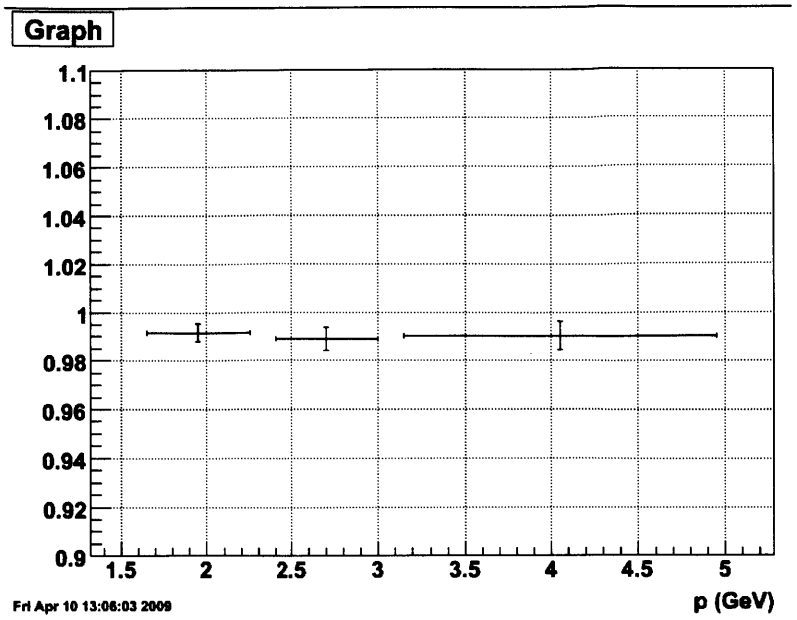

Figure A-5: The non-HT/TP triggered events demonstrate linearity in the detector over the electron momentum range 2 - 5 GeV/c as shown in this plot of E/p vs. momentum.

single particle Monte Carlo data samples. Since the correction had not been tested with data, there was concern this correction might bias the calibration (since the number electrons at a given radius from the center from the tower goes like r^2). We restricted ourselves to $r < 0.004$ and removed use of the GEANT correction. The effect of this change was measured by comparing the peak location to the nominal value of 1. This study was not able to measure a statistically significant effect, so no bias was assigned.

Background contamination had to be correctly modeled to find the peak position accurately. A study of a high background, low electron sample suggested that the best fit to the background in the peak region was a first order polynomial. Fitting to a gaussian plus line was found to produce stable peak positions as the amount of background was allowed in (by varying dE/dx). This effect can be seen in Fig. A-6. In addition, an isolation cut was added to remove additional jet contamination. The energy in the highest neighbor had to be less than 50% of the energy in the tower of interest. The effect of this change was measured by comparing the peak location to

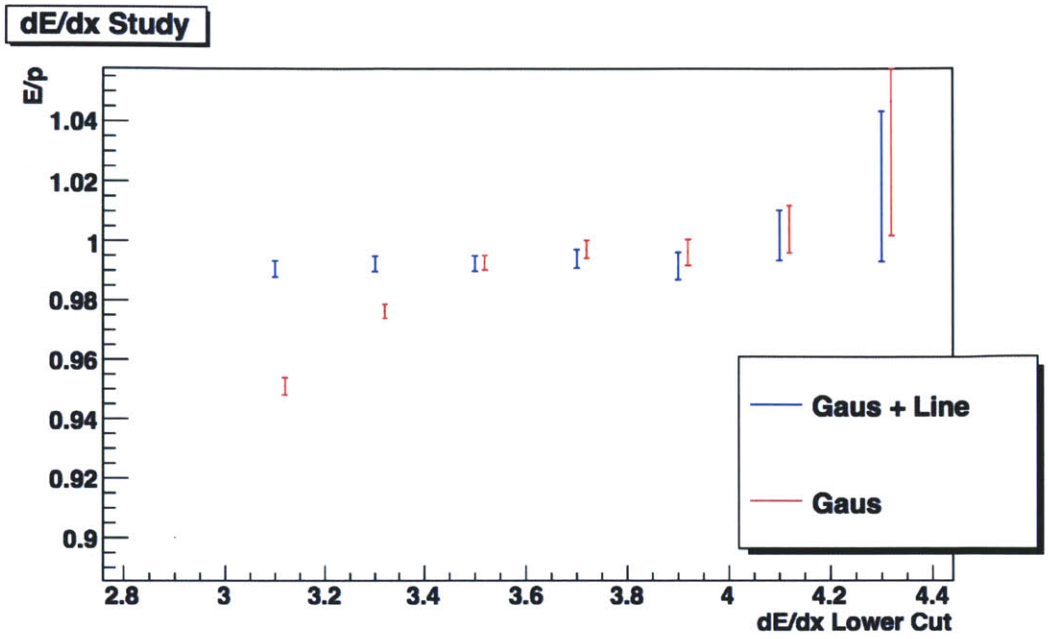

[h]

Figure A-6: As the lower cut on dE/dx was raised (removing more background), we see that the Gaussian + Line model had better stability than just a Gaussian. The lower cut on dE/dx of 3.5 keV/cm used for this study coincides with where the E/p location plateaus for both models.

the nominal value of 1. This study was not able to measure a statistically significant effect, so no bias was assigned.

The E/p for each crate (Fig. A-7) was calculated to investigate the effect of timing. Crate 12 exhibited strange behavior, which corresponds to the anomalous point in the figure. If this crate was removed from the sample, there was no deviation from statistical variation, which was tested by comparing the RMS of the E/p peaks in the crates from the RMS in a sample that was divided into 30 random samples. Five trials of the random divisions were performed and all were compared to the same mean peak position. The effect of the timing was attributed to the deviation of Crate 12 from the mean by taking that deviation and dividing by 15, the number of crates contributing to each eta ring. This contribution was 0.9%.

To measure an pseudo-rapidity dependent bias, we calculated the RMS of the peak position for various numbers of divisions. If there was no systematic effect, the RMS was expected to increase as the $\sqrt{N}$, where N was the number of divisions. This

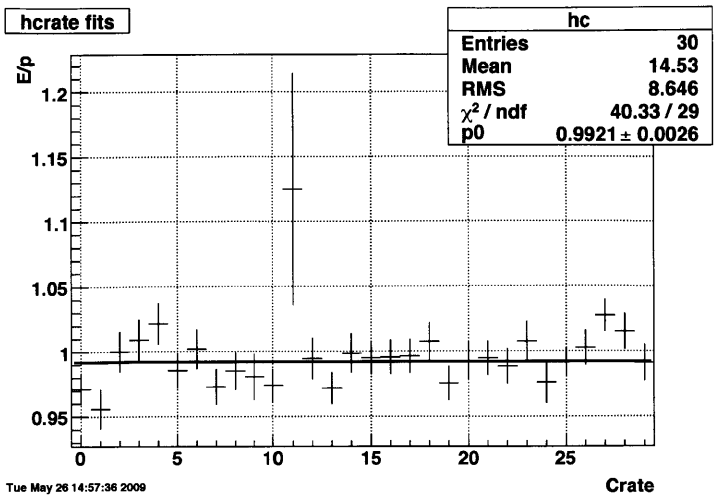

[h]

Figure A-7: Excluding Crate 12, there was no deviation beyond the expected statistical in the scatter of E/p for each crate. The axis here starts from 0 instead of 1. This figure only contains electrons from the restricted sample.

behavior can be readily observed in Fig. A-8, but we also compared to a sample where a systematic shift up of 1% was applied to the center of the barrel ($|\eta| < 0.5$) and a systematic shift down of 1% was applied to the outer barrel. From this calculation, we could conclude there is no significant pseudo-rapidity dependent bias. The maximum systematic consistent with the data is 0.2%, but no uncertainty is assigned, since this was not statistically significant. The rate dependence was measured by binning electrons by the average ZDC coincidence rate for the run they were found in (Fig. A-9). No bias was found after comparing the nominal value of 0.992 for this sample with any statistical significance.

The time dependence was measured by binning the electrons in three time periods, divided at the beginning of day 110 and day 130 (Fig. A-10). The deviation between the peaks in E/p of these periods was less than the bias from other sources. This uncertainty was calculated using all electrons, so the trigger bias is present in this data. For that reason, no contribution to this source was included in the estimate of

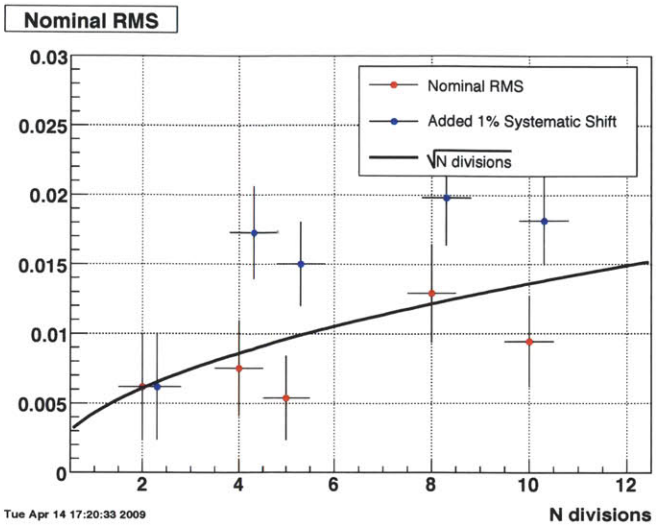

Figure A-8: A comparison between the RMS for different numbers of divisions in pseudo-rapidity and when an additional 1% systematic was introduced shows that there was no pseudo-rapidity dependent systematic uncertainty. This figure only contains electrons from the restricted sample.

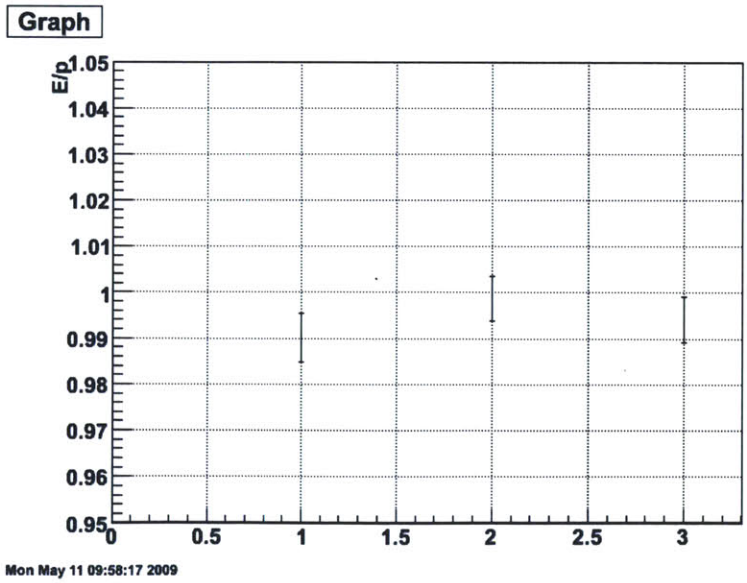

Figure A-9: E/p vs ZDC rate was calculated for the tightened calibration sample. The three points show the E/p peak location for different ranges of ZDC rate, which were chosen to have roughly equal statistics. Point 1 corresponds to 0 - 8000 Hz, 2 corresponds to 8000-10000 Hz and 3 corresponds to 10000-20000 Hz.

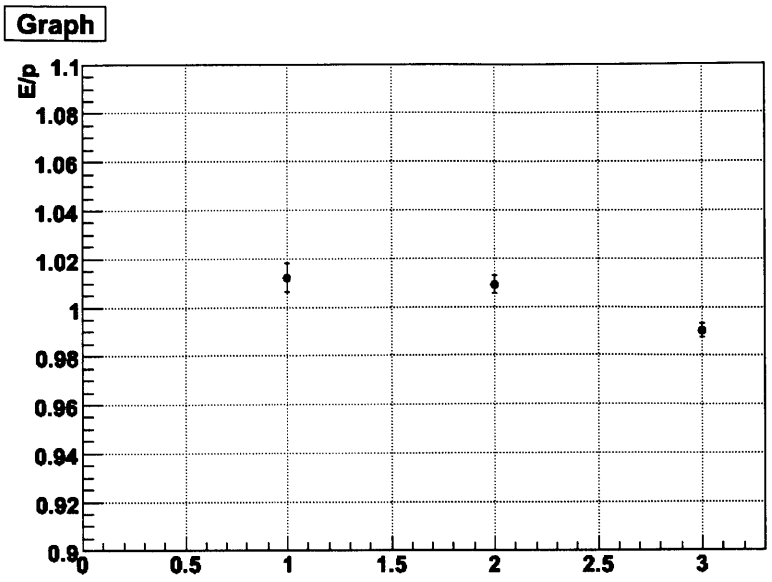

Figure A-10: The entire 2006 calibration electron sample was used to examine the time dependence. The first period was for before day 110. The second period was for between days 110 and 130. The third period was after day 130.

the systematic bias.

The total uncertainty came from adding the 1.3% from the trigger bias and the 0.9% from the crate bias together, resulting in 1.6%.

A.3 Updates to Methods in 2009

Having noticed the causes of several biases in the 2006 calibration, steps were taken to remove the effects of these biases in the 2009 calibration. The most significant bias noted previously was trigger sculpting introduced by high tower (HT) events. In this analysis, any event that had a non-HT trigger was accepted. Electrons in HT events could be accepted if they did not point to a trigger tower. Consequently, the trigger bias is negligible.

To mitigate crate dependencies, the segmentation for the absolute calibration was done in "crate-slices" for the innermost pseudorapidity rings ($|\eta| < 0.95$). A crate-slice consisted of the eight towers in a given crate at the same pseudorapidity. The outermost rings were calibrated by ring, as done previously. This finer division was

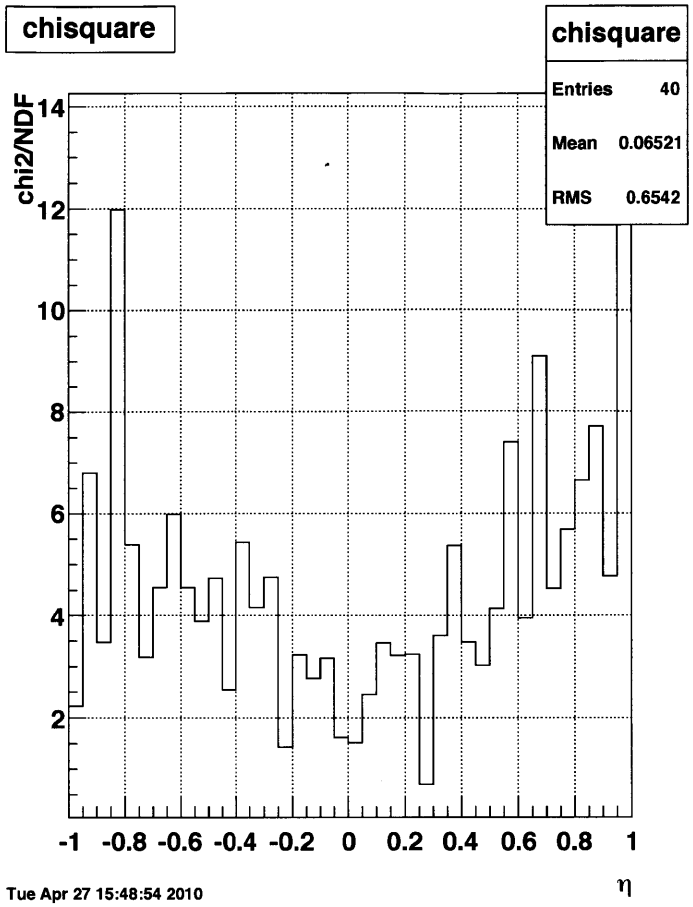

Figure A-11: The distribution of E/p corrections in a given pseudorapidity ring did not have statistical variation, as demonstrated by this plot of χ^2/NDF for the distribution of E/p in each ring.

made possible by the higher statistics available for the calibration.

The change to more bins was motivated by the previously noticed non-statistical variation between different crates. A correction by crate was applied in 2008 for this effect. The need for this additional correction can be removed by directly calibrating the smallest group of towers possible. Figure A-11 shows that the variation in the corrections calculated in this manner cannot be explained by statistical fluctuations alone.

A new GEANT correction was calculated to take into effect energy loss in material between the TPC and the BEMC and the pseudorapidity dependence. The new correction was calculated for each pseudorapidity ring by throwing electrons at several

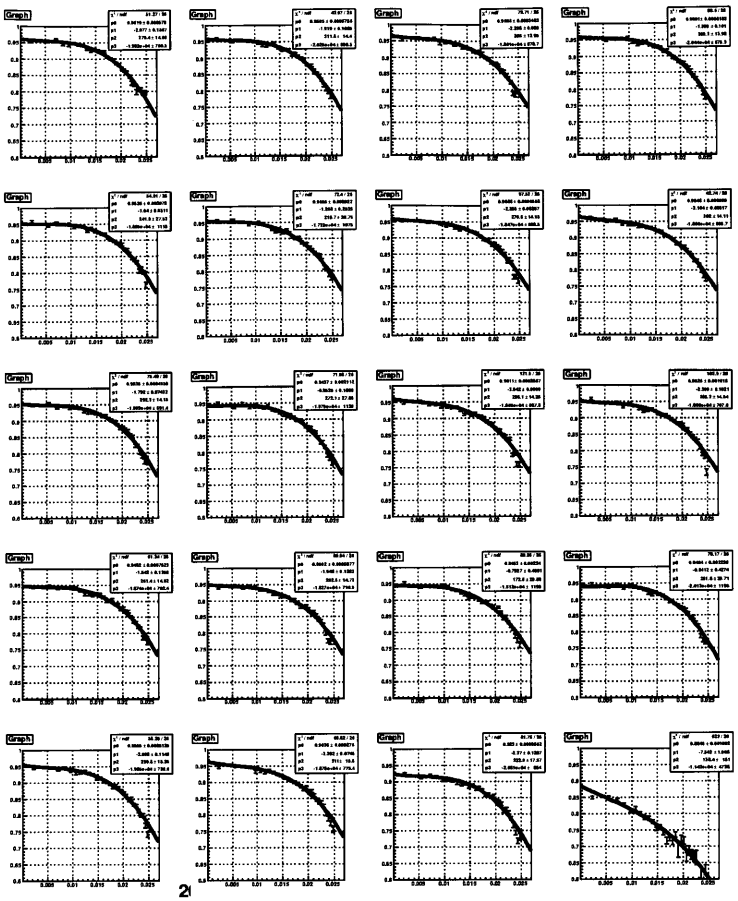

Figure A-12: The GEANT correction for each pseudorapidity ring. This correction multiplies the track momentum of the calibration electron depending on the distance it strikes the tower from its center.

different energies, then calculating the amount of their energy deposited in the tower they struck as a function of $R = \sqrt{(\Delta\phi)^2 + (\Delta\eta)^2}$ from the center of the tower. The energy dependence below 10 GeV was found to be negligible. Since calibration electrons were predominantly in this energy range, no energy dependence was folded into the correction. Figure A-12 shows the twenty correction functions used in each bin along with their parameterizations for a third order polynomial.

A.3.1 PMT Mapping Check

A check of the mapping between PMT base and softId was conducted for the first time at the beginning of Run 9. A set of seven runs were taken, each with a different

set of towers off (determined by the value of softId % 7). The rest of the towers were set to 300V to minimize wear during the test.

Several swaps were identified and fixed. A second set of six runs were taken with higher statistics to confirm some ambiguous swaps from the first set. A total of 44 swaps were made. The list can be found in [64].

A.3.2 HV adjustment

Prior to 2008, the high voltages (HV) were adjusted to improve trigger matching in the outer two η rings on each side. These changes were made in the wrong direction. It was decided to not only fix those rings, but also to improve the the overall uniformity for the entire BEMC and move the mean closer to ideal gains.

Using the calibration calculated from 2008, we adjusted the high voltages according to the formula:

$$\frac{C_{ideal}}{C_{meas}} = \frac{slope_{ideal}}{slope_{meas}} = (\frac{HV_{init}}{HV_{set}})^k, \tag{A.4}$$

where C_{ideal} was the ideal calibration value for a tower, C_{meas} was the calibration constant we measured in 2008, $slope_{ideal}$ was the slope we measured with a new HV setting, $slope_{meas}$ was the slope we measured with the initial HV setting, HV_{init} was the initial HV setting, HV_{set} was the new value, and the constant $k = 10.6$ was measured using LED data.

Run 10066163 was taken at the beginning of Run 9, using the 2008 voltages, corrected for the mapping changes calculated earlier. Run 10066160 was taken using the HV values calculated according to Eq. A.4. After these runs were taken, some additional analysis was carried out by Stephen Trentalange [65], and 81 corrections or other changes were made to the new settings for the final HV settings for Run 9.

Offline calibration confirmed that these new settings improved uniformity and moved the full scale closer to the ideal settings. Figure A-13 shows the comparison between full scale E_T for Run 8 and Run 9. The overall scale for Run 9 has been reduced to 60.6 GeV from 63.8 GeV in Run 8, and the spread of the distribution has been reduced from 5.4 GeV in Run 8 to 3.9 GeV in Run 9. Similar improvements

[h]

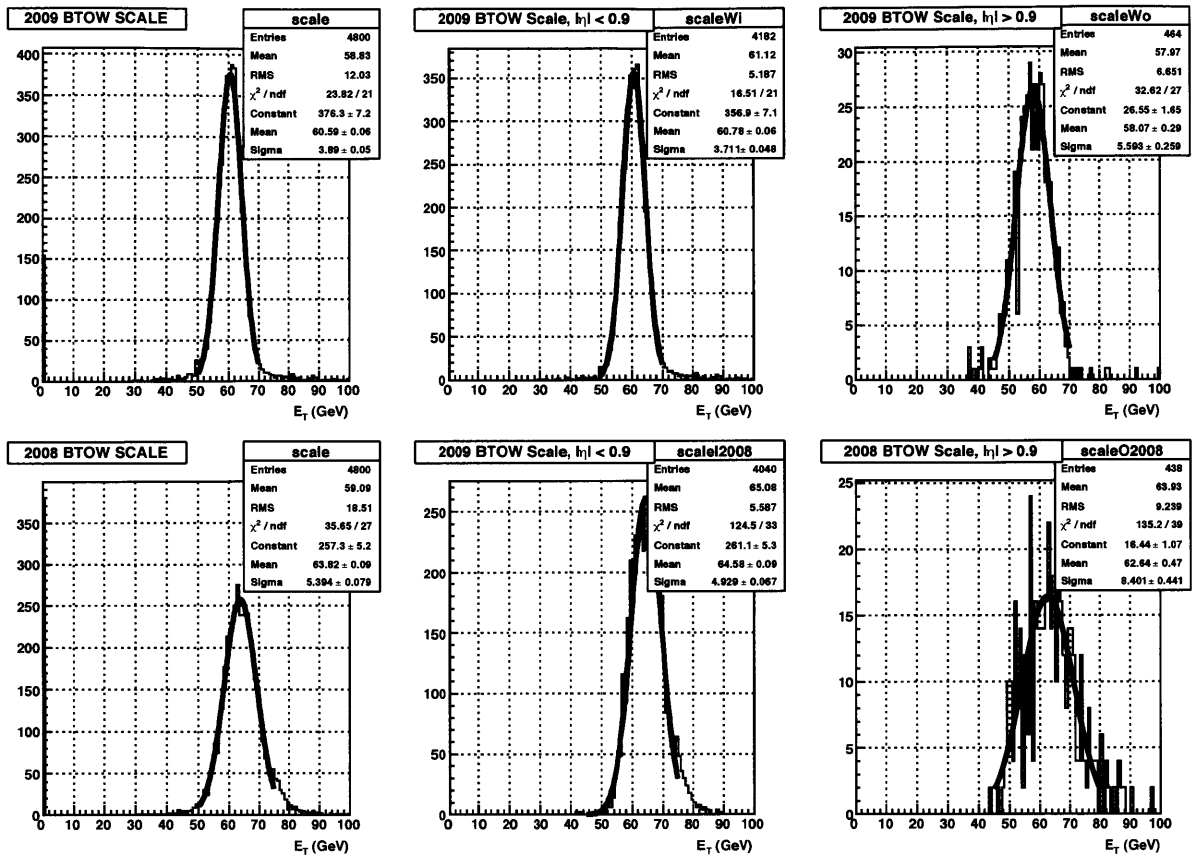

Figure A-13: A comparison of the distribution of full scale E_T for all calibrated towers for run 9 (top) and run 8 (bottom). The left panels show the distributions for all towers, the center panels show the distributions for the towers with $|\eta| < 0.9$, and the right panels show the distributions for the towers with $|\eta| > 0.9$.

were seen separately for the sets of towers with $|\eta| < 0.9$ and $|\eta| > 0.9$.

A.4 2009 Uncertainty

Some biases were noticed over the course of this calibration. One bias was the difference between the calibration calculated for positrons and electrons separately. This difference indicated a bias in the TPC calibration. Similarly, there was a difference when the calibration was done separately for Full Field data and Reversed Full Field data. The uncertainty for these two effects was controlled together by comparing the calibration calculation to the four independent sets made from each charge and each

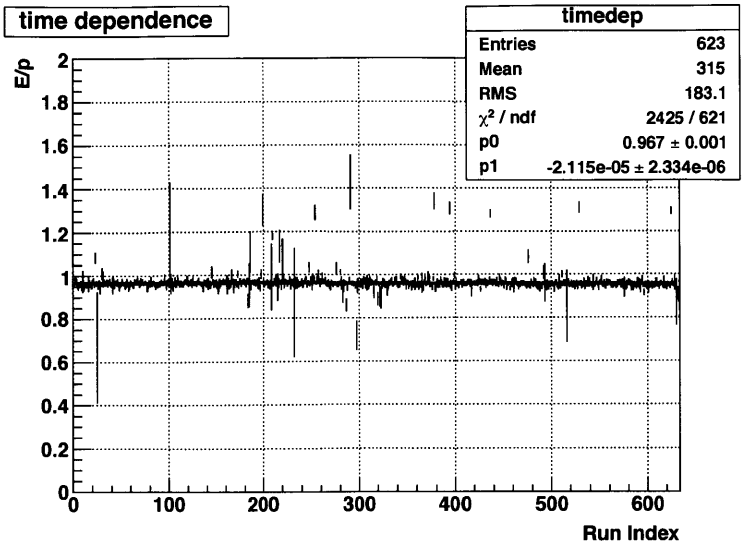

Figure A-14: This figure shows the overall E/p peak location for each run before the calibration is applied as a function of an arbitrary, time-ordered run index. The slope of the best fit is non-zero, but extremely small.

field regime. The mean difference for these four sets from the nominal calibration was calculated, and the maximum selected for the uncertainty. The value was 1.7%, coming from the electrons in Reversed Full Field Data.

The time dependence of the calibration was also checked by calculating the overall constant for each run used in the calibration. With the exception of several outlier points, the time dependence of this calibration is extremely slight. The results of this study are shown in Fig. A-14. The systematic assigned for this effect was 0.005%.

Since a new GEANT correction was used, the dependence of the E/p calculation on $R = \sqrt{(\Delta\phi)^2 + (\Delta\eta)^2}$ was calculated. The shape of this dependence shown in Fig. A-15. There was no physical explanation for why the shape resembles a sinusoid, but the shape was fit to the function $A\sin(bx+c)+D$ and the amplitude A was extracted as an estimate of the uncertainty due to the GEANT correction. This uncertainty was 0.8 %.

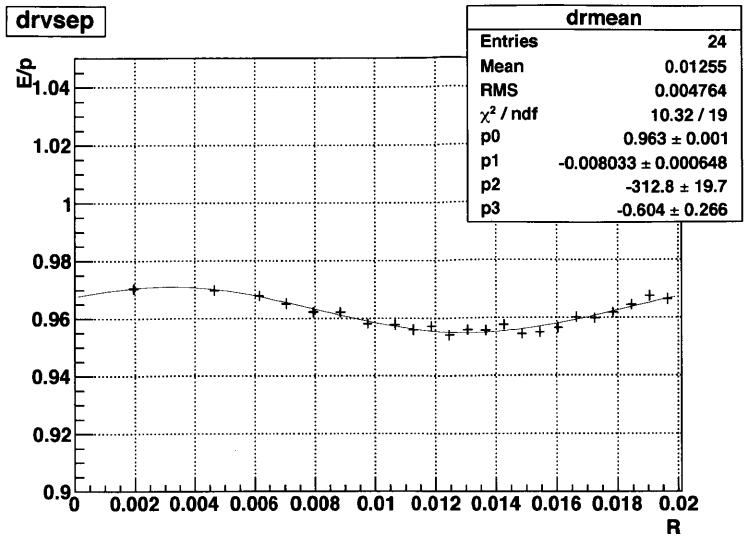

Figure A-15: E/p as a function of $R = \sqrt{(\Delta\phi)^2 + (\Delta\eta)^2}$. The shape of the figure resembles a sinusoid, but there was no obvious physical reason why that should be the case.

A.5 Conclusions

The BEMC was successfully calibrated in-situ using MIPs and electrons in 2006 and 2009. Careful study of systematic effects in 2006 allowed the systematic uncertainty to be reduced from the 2005 value of 4.8% to 1.6%. The contributions to the 2006 value are included in Table A.1. The experiences of 2006 informed the calibration method of 2009, but problems with the TPC calibration limited the systematic uncertainty to a total value of 1.9%. The contributions are included in Table A.2.

Table A.1: 2006 Contributions to Uncertainty

Cause	Bias Calculated	Statistical Significance
Trigger Bias	1.3%	3.7σ
Crate Effect	0.9%	1.4σ
Leakage Correction*	0.037%	0.17σ
Background*	0.036%	0.20σ
Eta Dependence*	0.2%	0.46σ
Rate Dependence*	0.2%	0.40σ
Time Dependence†	1.0%	3.2σ
Total	1.6%	

Table A.2: 2009 Contributions to Uncertainty

Cause	**Bias Calculated**
TPC effects (charge sign and field)	1.7 %
Time Dependence	0.005%
GEANT correction	0.8 %
Total	1.9%

Appendix B

BEMC Simulation Chain Model

In order to explain all of the different energy scales that were present in our understanding of the BEMC and how STAR corrected its data for various effects, a model of the BEMC simulation and analysis chain was developed. For a graphical representation of the model see figure B-1.

In the model envisioned, there was an initial part in which the physics processes were generated in the geometric volume before any of the produced particles have had a chance to interact with any piece of the detector. In the case of this analysis, this was done using PYTHIA or HERWIG and GEANT.

Next, there was a piece that was the relevant GEANT tracking in which the particles are propagated through the detector, interacting at various levels and eventually depositing a portion, if not all, of their energy into detector elements, some active, some inactive. The relevant uncertainties that were present in this portion of the chain are how well the amount of matter and its constitution were known and how well the cross sections for the interaction of various particles in the matter were known.

GEANT reported the energy deposited in the active elements which the STAR slow simulator converted into a reconstructed deposited energy by simulating the sampling fraction and other detector effects. An example of the calculations performed at this level was an estimate of the energy resolution based on photon statistics in the fibers and PMTs. These simulations were based on studies done in the test beam and in data.

[!ht]

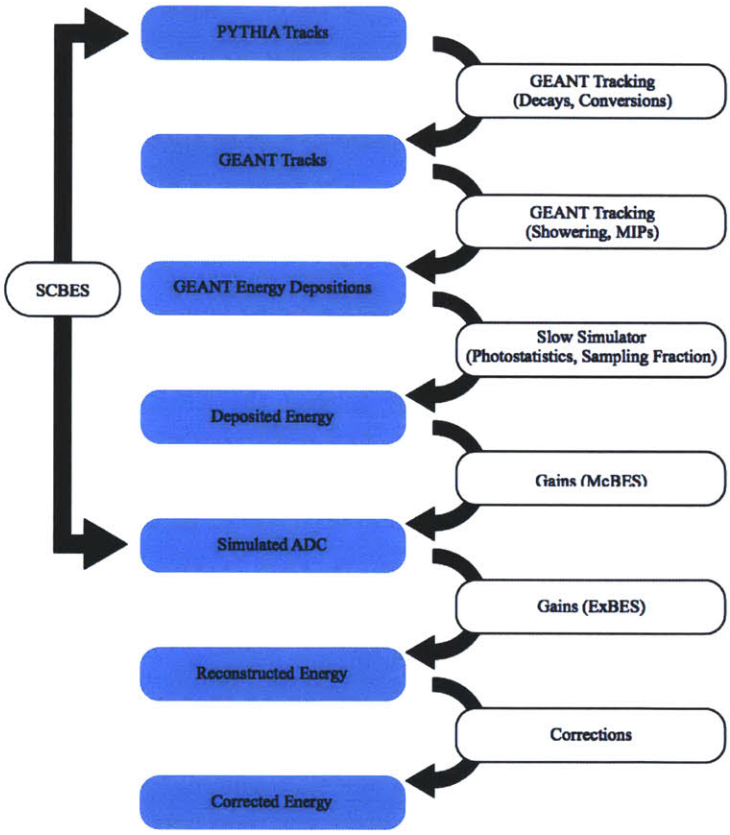

Figure B-1: A model of the BEMC detector simulation chain. It tracks the simulation from the intitial generated physics event, through its interaction with the detector, the characterization of the active elements in the slow simulator and then finally through our calibrations and energy scales to the final reconstructed energy.

Given this amount of reconstructed deposited energy, which ideally represents the true amount of deposited energy of a particle in the BEMC, it was then converted to an ADC value. This conversion of the deposited energy into an ADC value was the Monte Carlo BEMC Energy Scale (McBES). It was really an inverse gain, but for ease of language it will also be termed an energy scale. The entire chain that took a particle of an initial energy to an ADC value was called the Simulation Chain BEMC Energy Scale (SCBES).

Next, the analysis part of the simulation then converted that calculated ADC value to an energy through a gain. This energy scale, the conversion from the ADC to a reconstructed energy, was the Experimental BEMC Energy Scale (ExBES) which was, in general, different from the McBES though it was expected to be highly correlated with it. This energy scale was what is measured in data.

Lastly, a number of corrections should then be applied to the reconstructed energy. These could include possible effects like clustering effects and tower leakage effects depending on how the individual analysis was done.

Appendix C

Cloud Computing for STAR Simulations

To generate the simulations for the 2009 dijet analysis, STAR made use of a cloud computing facility at Clemson University. A Kernel Virtual Machine (KVM) image was generated to STAR specifications and deployed in snapshot mode to 2,000 cores at the facility. The jobs were managed by a tool developed at Clemson called Kestrel and monitored by a custom database interface.

C.1 Virtualization

The modern concepts and definitions surrounding virtualization were developed by Popek and Goldberg [66] in 1974. A virtual machine is defined in the context of a virtual machine monitor (VMM), in which a virtual machine is a resident environment. The term hypervisor is equivalent for most intents and purposes to a VMM in current usage.

There are three properties that a VMM must satisfy: efficiency, resource control, and equivalence [66]. The efficiency requires that the VMM not intervene with the execution of any innocuous instructions by the hardware. Resource control states that a program in a virtual machine must be isolated from direct control of all system resources. Equivalence requires that the execution of a program within a virtual

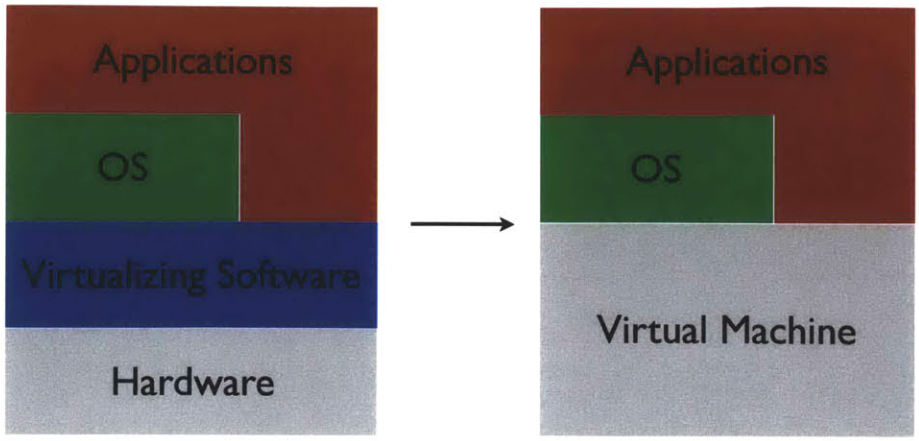

Figure C-1: A diagram depicting how virtual machine monitors interact with hardware, operating systems, and applications in system virtual machines.

machine must be the same as if the program were executing in a regular environment. The only exception to equivalence is that the time of execution of a program can be longer in the virtual machine because there will be occasional interventions of the VMM.

The benefit of virtualization is that it increases flexibility in what kind of software systems can be deployed on a given physical machine [67]. Operating systems, for example, are tied to specific memory systems, I/O system interfaces, and processor instruction sets. VMMs provide a mapping between a the architecture of the real machine and the desired virtual architecture. A system virtual machine translates the instruction set architecture, allowing the use of operating systems on incompatible hardware or even multiple operating systems on the same hardware (see C-1).

Physics analysis software typically requires a fairly tall software stack to run properly and is limited to a certain type of operating system. Installation of an operating system and the accompanying software stack can take anywhere from several hours to days for even an expert user. The creation of a virtual machine image by software experts allows for the effortless proliferation of the analysis environments, which were

previously limited primarily to use on clusters managed by experts. Software from VMware and VirtualBox, for example, make it possible to run virtual machines on personal computers.

C.2 Cloud Computing

The central idea behind cloud computing is to make computing resources like processor cycles and memory use fungible. Cloud subscribers purchase time on machines from service providers. The most common model at the moment is to purchase an instance, which usually has some memory and processor specifications, for a small period of time, typically an hour.

The use of cloud computing allows users to purchase computing resources on demand instead of requiring them to keep resources on standby. This model removes the capital expenditures needed to get a computing cluster online and delegates responsibility for maintenance to the service provider. Use of virtualized environments make it easy for different users to load their personalized systems onto the machines.

STAR has experimented with several different cloud models, including Amazon's EC2, the CondorVM project at the Grid Laboratory of Wisconsin (GLOW), and a project at the Clemson Palmetto cluster. These models all used virtual machines as the worker nodes with a variety of different methods used to manage the cluster.

C.3 Kestrel

Kestrel is a framework for Many Task Computing (MTC) applications designed by Clemson University [68]. The framework uses the Extensible Messaging and Presence Protocol (XMPP), which is the basis of several large instant messaging systems with millions of clients. The system was designed with scalability in mind to overcome the issues that have plagued other Virtual Organization Clusters (VOC).

Resources in XMPP systems identify themselves with a Jabber ID (JID), which are registered with the XMPP server. A benefit of this feature is that Kestrel workers

do not need to be assigned a unique IP address; they can be operated in network address translation (NAT) mode.

There are three types of messages in XMPP, of which Kestrel uses two. Presence notifications are used by worker resources to notify the manager of their status. Chat messages are used for communication of commands or data between agents. The messages use a JavaScript Object Notation (JSON) dictionary to control the workers with a variety of attributes. Workers can inform the manager what attributes they provide using the same system.

A direct feature of the Kestrel implementation is that jobs can be managed using common place chat clients that support XMPP, such as Adium or Pidgin. An XMPP server can continue accepting messages even if the receiving agent is not connected, making persistent presence unnecessary.

C.4 STAR Simulation on the Cloud

A virtual machine image with Scientific Linux 5.3 as the guest operating system was created using KVM. Installation of the STAR software stack, which require a diverse set of external libraries and over 2.5 million lines of custom STAR code, was accomplished using a set of scripts developed to streamline the creation of STAR virtual machines.

Beyond the basic STAR installation, there were several additional applications required to meet the needs of running on the cloud. A version of the STAR database, which contains calibration values and status codes for different running periods, was deployed on the image to help reduce network traffic. Entries not relevant to the time period being simulated were removed, and the database was compressed using myisampack, which together reduced the database size from 25 GB to 0.5 GB. One side effect of the compression is that the database could only be operated in read-only mode, but simulations did not need write privileges.

The Globus toolkit was also installed on the image with myproxy to allow worker nodes to transfer output back to RCF through STAR grid gatekeepers using gridftp.

The decision to use myproxy reduced the security footprint to the single password needed to access the myproxy credential. In the event of a possible breach, the credential on the myproxy server could be deleted to mitigate the threat.

The Kestrel framework allowed jobs to run scripts that were already present in the virtual image. Files could not be transferred along with the job instructions. This limitation was minimized by having each job contact an update server and download updated scripts.

One weakness the cloud and grid applications share is the difficulty in obtaining real time information about the states of currently running jobs. Log files cannot be viewed until they are transferred back to the user in most current setups. To overcome this problem, a custom monitoring system was developed for this simulation.

Each job was set up to send status information at several steps throughout the job using HTTP POST commands with cURL to a database at MIT. Plots generated with this status information were used for online monitoring of the state of the jobs and the virtual cluster.

Using this monitoring system, it was possible to attain a picture of the progress of the simulation and the status of the cluster in real time. For instance, the number of machines available is compared with the number of working machines and the number of idle machines in Figure C-2.

At the end of each job, the MD5 sum of each output file was computed and stored in the log file for comparison after the transfer back to RCF. Approximately 5% of output files were corrupted during the transfer.

The VMs were started on the Clemson cluster using PBS. To avoid the need to distribute the VM image to each node at the beginning of the task, these VMs were started using KVM's snapshot mode. In previous exercises where snapshot mode was not used, it cost several hours to transfer images and boot VMs on approximately 500 nodes. Snapshot mode used the base image over a network connection, and changes were saved to a new file using a copy-on-write strategy. This method also saved disk space on the physical nodes, which had only 2.5 GB per processor.

Sustained running for approximately one month resulted in the production of over

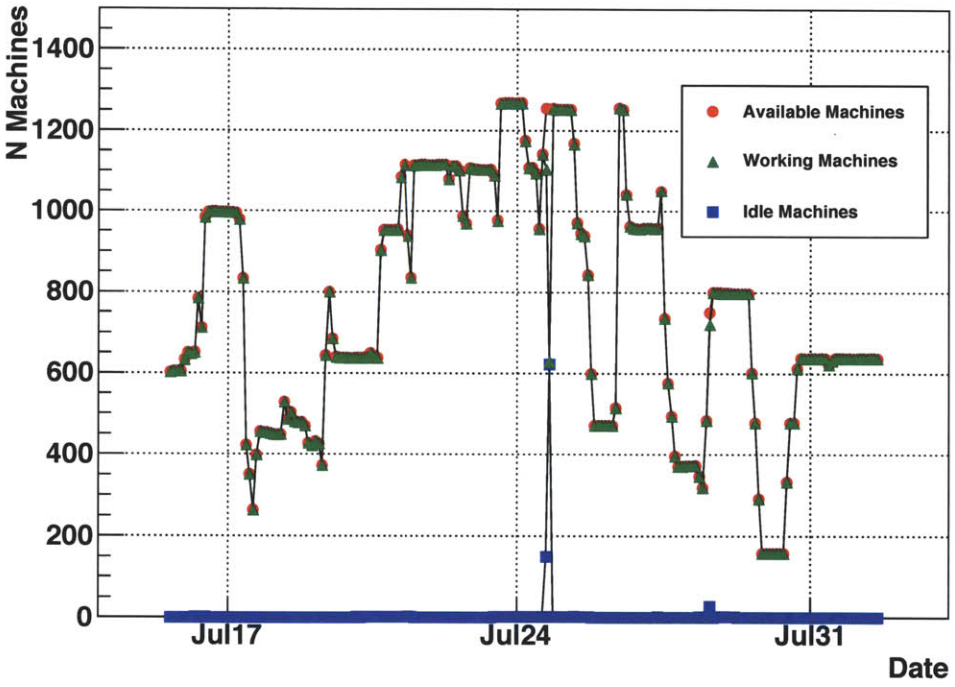

Figure C-2: Tracking the number of jobs as a function of time in the PBS and Kestrel systems. The number of virtual machines instantiated tracks the number of available nodes, indicating a good response of the system. A guaranteed allocation of 1,000 slots for a few days around July 21 shows we exceeded the allocation and took advantaged of empty slots on the farm.

12 billion events using the PYTHIA event generator. Using a filtering framework developed in STAR, this total was reduced to 36 million signal events. Nearly 7 TB were transfered back to the RCF for additional analysis. The total CPU time used was over 400,000 hours, which represents an expansion of 25% over what was available to STAR at the RCF, of which only about 2.5% would be available to a similar simulation request. In other words, this simulation would have taken approximately a year if only RCF resources had been used.

Appendix D

Logical Deduction of Cross Section Formula

The purpose of this section is to explain where Eq. 5.1 came from and why it is used in this analysis. The formula is reproduced here for convenience

$$\frac{d\sigma_i}{dM_i} = \frac{1}{\Delta M_i}\frac{1}{L}\frac{1}{A_{vert}}\frac{1}{\epsilon_i^{reco,vert}}\sum_j \alpha_{ij}\epsilon_j^{misreco}\frac{1}{\epsilon_j^{trig}}J_{j,reco}^{trig}. \tag{D.1}$$

In general, the formula for a differential cross section should look something like

$$\frac{d\sigma_i}{dM_i} = \frac{1}{\Delta M_i}\frac{1}{L}\frac{1}{A_{vert}}C_i J_{i,reco}^{trig}, \tag{D.2}$$

where C_i is some correction factor and $J_{i,reco}^{trig}$ is the reconstructed triggered dijet yield in bin i. The vertex acceptance A_{vert} is a factor to account for the amount of events that occur outside of the allowed vertex region.

The decision to use an unfolding method dictates the formula become

$$\frac{d\sigma_i}{dM_i} = \frac{1}{\Delta M_i}\frac{1}{L}\frac{1}{A_{vert}}B_i\sum_j \alpha_{ij}D_j J_{j,reco}^{trig}, \tag{D.3}$$

where $J_{j,reco}^{trig}$ is now the same yield in bin j, D_j is some correction to bin j that must be applied before unfolding, α_{ij} is the unfolding matrix element, and B_i is a correction

to bin i that is applied after unfolding. This new formula closely resembles Eq. 5.1.

Calculation of the unfolding matrix requires that dijets be found at both the particle and detector level in simulation. This requirement will dictate what effects are corrected before or after unfolding. Since the dijet reconstruction efficiency by definition is a calculation of how often a dijet found at the particle level is not found at the detector level, this correction must go after unfolding is applied (as part of B_i). Similarly, the vertex reconstruction efficiency must be applied at the same stage. Though it's possible to calculate the vertex reconstruction efficiency by itself, it is not possible to calculate an independent dijet reconstruction efficiency, so these two terms should be combined into a single correlated efficiency $\epsilon_i^{reco,vert}$ and $B_i = \frac{1}{\epsilon_i^{reco,vert}}$.

On the other side of the unfolding, any explicit biases that could be present in the reconstructed dijet spectrum should be corrected be corrected. The BJP2 trigger fires in the presence of a neutral energy sum above a certain threshold in one of the six jet patches. This situation introduces a neutral energy bias that is largest near the threshold. There is also an acceptance effect that has the largest effect near threshold. Trigger effects are quantified by the trigger efficiency ϵ_j^{trig}. Dijets can also be also be reconstructed even if associated jets failed some cuts at the particle level due to resolution. These dijets should be removed from the reconstructed dijet spectrum using $\epsilon_j^{misreco}$. No other effects need to be corrected here, so $D_j = \epsilon_j^{misreco}\frac{1}{\epsilon_j^{trig}}$.

Substituting for B_i and D_j in Eq. D.3, Eq. 5.1 comes out.

Appendix E

Tests of the Unfolding Method

To test the robustness of the unfolding method, a toy model was developed. In the model, an unfolding matrix was calculated for an input distribution and point spread function. To create the tree for the unfolding matrix, the distribution

$$f(\mu) = \frac{1}{\mu^{-8}} \tag{E.1}$$

was sampled 10^7 times. For each sample "event" the point spread function

$$y(x;\mu) = \exp\frac{(x-\mu)^2}{2} \tag{E.2}$$

was sampled once. In this example, y represents the reconstructed variable and μ represents the true variable. Knowing the relation between y and μ makes it possible to calculate the unfolding matrix.

The unfolding matrix was then applied to six samples with the same point spread function but unknown input distributions. Fig E-1 shows the performance for the different input distributions. This study indicated that the unfolding method did not bias the shape of the differential cross section.

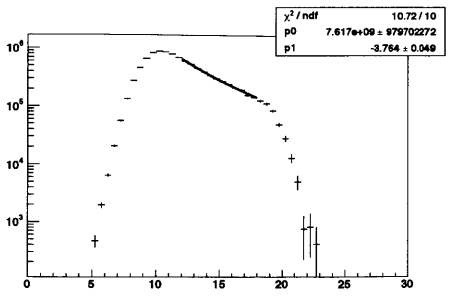

(a) n = -4

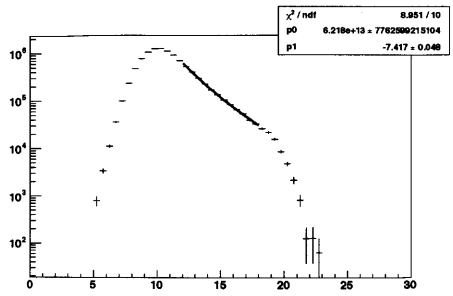

(b) n = -7.5

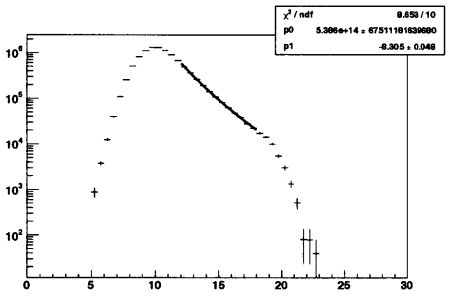

(c) n = -8.3

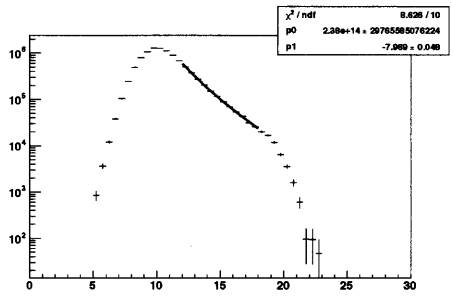

(d) n = -8

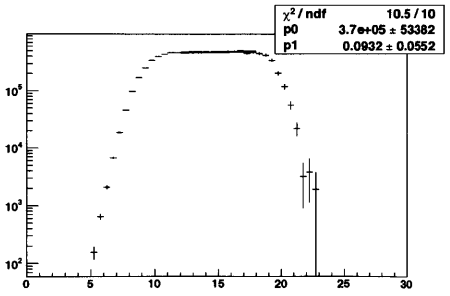

(e) n = 0

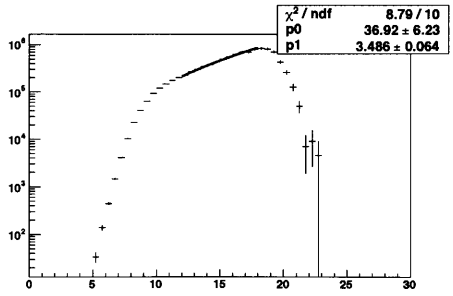

(f) n = 3.8

Figure E-1: An unfolding matrix was caluclated for an input distribution of $f(x) = \frac{1}{x^{-8}}$ and a gaussian point spread function with $\sigma = 1$. This figure shows the unfolding performance for unknown input distributions of the form $f(x) = x^n$.

Table E.1: Unfolding Toy Model Performance

n_{true}	n_{reco}
-4	-3.8 ± 0.05
-7.5	-7.4 ± 0.05
-8	-8.0 ± 0.05
-8.3	8.3 ± 0.05
0	0.1 ± 0.05
3.8	3.5 ± 0.06

Table E.2: Comparison of uncertainties for Bin by Bin versus Matrix Unfolding

Mass	Bin Stat.	Bin Syst. Up/Down	Matrix Stat.	Matrix Syst. Up/Down
20 - 24.25	0.045	0.29/0.28	0.049	0.27/0.28
24.25 - 30.01	0.036	0.16/0.26	0.037	0.18/0.23
30.01 - 37.90	0.041	0.18/0.23	0.035	0.19/0.24
37.90 - 48.83	0.059	0.23/0.24	0.047	0.21/0.25
48.83 - 64.15	0.08	0.23/0.35	0.06	0.23/0.30
64.15 - 85.92	0.18	0.39/0.54	0.12	0.29/0.41
85.92 - 117.29	na	na	0.48	0.34/0.48

E.1 Comparison of Matrix Unfolding with Bin-by-bin

Previous STAR jet analyses have used a bin-by-bin unfolding method, which was essentially an approximation in which the unfolding matrix was exactly diagonal. This method was compared to the matrix unfolding method used in the 2005 cross section analysis to understand the differences. The major difference was that it was not possible to extract the cross section from the bin with $85.92 < M < 117.29$ in the bin by bin method. Table E.2 shows the effect of the two methods on the statistical and systematic uncertainties. Figure E-2 shows that the two methods only resulted in slight differences in the cross section values.

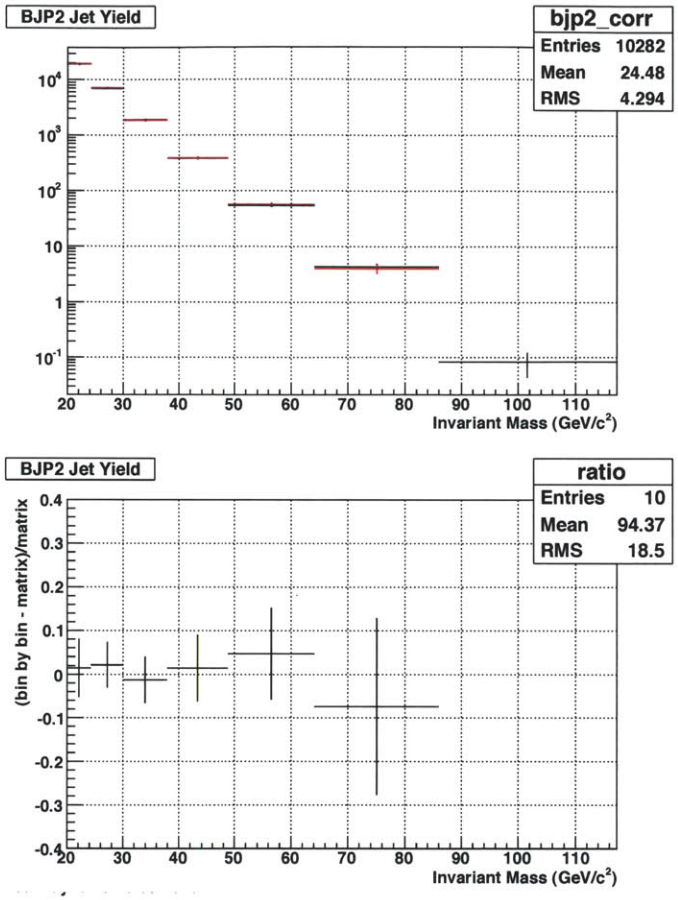

Figure E-2: (Top panel)A comparison of the cross section using the matrix unfolding (black) with the bin by bin unfolding (red) and statistical uncertainties only. The most important difference is the inability of the bin by bin method to extract the cross section in the last bin. (Bottom panel) The ratio of bin by bin cross section over the matrix cross section with statistical uncertainties only. The different methods do not shift the values considerably.

Appendix F

Spin-Sorted Yields in Simulation

In simulation, it might be helpful to be able to group events using the usual spin sorting conventions used by the data. This grouping could be useful for studying, for example, if different trigger efficiencies for the different subprocesses introduces a false asymmetry. This note will explain how to perform this separation for a given polarized cross-section calculation.

To determine the spin state, it is necessary to know the posterior probability of the spin state with both partons aligned with their protons given the scattering kinematics x: $p(++|x)$. Unless otherwise state or obviously separated, we will denote $p(++|x) = p(++|x) + p(--|x)$ and $p(+-|x) = p(+-|x) + p(-+|x)$. We will present two derivations for the expression for $p(++|x)$.

F.1 Simple Derivation

Recall the theoretical expression for A_{LL}:

$$A_{LL} = \frac{\int dx \sum_{f,g,h} \Delta f \times \Delta g \times d\sigma \cdot a_{LL} \times D_h}{\int dx \sum_{f,g,h} f \times g \times d\sigma \times D_h} \tag{F.1}$$

and the experimental expression for A_{LL} with 100% polarization and equal relative luminosities:

$$A_{LL} = \frac{N^{++} - N^{+-}}{N^{++} + N^{+-}}. \tag{F.2}$$

We can ignore the fragmentation and equate the numerator and denominator of the two equations.

$$
\begin{aligned}
1 &= p(++|x) + p(+-|x) \\
\int dx \sum_{f,g} f \times g \times \sigma &= N^{++} + N^{+-} \\
\int dx \sum_{f,g} f \times g \times \sigma &= \int dx \sum_{f,g} f \times g \times \sigma (p(++|x) + p(+-|x)) \\
\int dx \sum_{f,g} \Delta f \times \Delta g \times \sigma \cdot a_{LL} &= N^{++} - N^{+-} \\
\int dx \sum_{f,g} \Delta f \times \Delta g \times \sigma \cdot a_{LL} &= \int dx \sum_{f,g} f \times g \times \sigma (p(++|x) - p(+-|x)) \\
&= \int dx \sum_{f,g} f \times g \times \sigma (2p(++|x) - 1) \\
p(++|x) &= \frac{1}{2}[1 + \frac{a_{LL} \Delta f(x) \Delta g(x)}{f(x) g(x)}]
\end{aligned}
\tag{F.3}
$$

In Eq. F.3, we have dropped the sum and integral because the probability must be true for each set of kinematics.

F.2 Probabilistic Derivation

From the definition of Δf, it follows that the probability, q_f, that the spin of the parton is aligned with the spin of its parent proton is

$$q_f = \frac{1}{2}(1 + \frac{\Delta f}{f}). \tag{F.4}$$

Furthermore, the fraction, α, of the cross section contributed by aligned spin states is

$$\alpha = \frac{1}{2}(1 + a_{LL}). \tag{F.5}$$

From these two expressions, we can calculate the likelihood $p(x|++)$:

$$\begin{aligned} p(x|++) &= 2(q_f q_g + (1-q_f)(1-q_g))\alpha + 2((1-q_f)q_g + q_f(1-q_g))(1-\alpha) \\ &= \frac{1}{4}[(2+2\frac{\Delta f \Delta g}{fg})(1+a_{LL}) + (2-2\frac{\Delta f \Delta g}{fg})(1-a_{LL})] \\ &= \frac{1}{2}(1+a_{LL}\frac{\Delta f \Delta g}{fg}) \end{aligned} \tag{F.6}$$

Similarly, we find

$$p(x|+-) = \frac{1}{2}(1-a_{LL}\frac{\Delta f \Delta g}{fg}) \tag{F.7}$$

We can then used Bayes' Rule to calculate $p(++|x)$:

$$\begin{aligned} p(++|x) &= \frac{p(x|++)p(++)}{p(x|++)p(++) + p(x|+-)p(+-)} \\ p(++) &= p(+-) \\ p(++|x) &= \frac{\frac{1}{2}(1+a_{LL}\frac{\Delta f \Delta g}{fg})}{\frac{1}{2}(1+a_{LL}\frac{\Delta f \Delta g}{fg}) + \frac{1}{2}(1-a_{LL}\frac{\Delta f \Delta g}{fg})} \\ p(++|x) &= \frac{1}{2}(1+a_{LL}\frac{\Delta f \Delta g}{fg}) \end{aligned} \tag{F.8}$$

We see that both derivations achieve the same result.

F.3 Application

There are two methods for using $p(++|x)$ to generate $N^{++(+-)}$. The first method is to assign a weight, $w = p(++|x)$ to each event and increment the N^{++} histogram by w (or N^{+-} by $(1-w)$). The second method is to separate the two samples by assigning each event to N^{++} with probability $p(++|x)$ and to N^{+-} otherwise. We recommend using the second method, since the two samples will then be statistically independent.

This separation needs to be performed independently for each asymmetry calculation. For instance, there are twenty different calculations coded into StMCAsymMaker, so there would need to be twenty different sets of spin-sorted yields.

F.4 Comparison to Method of Asymmetry Weights

The current method for determining an asymmetry from Monte Carlo is based on the Method of Asymmetry Weights (MAW) described originally by the developers of SPHINX, a polarized MC generator based on PYTHIA, but using transverse polarization. Note that SPHINX does not use the MAW, but actually generated events using polarized parton distribution functions.

In this method, each event is assigned an asymmetry weight $A_{LL,i}$, and the total asymmetry A_{LL} is the sum over these weights divided by the unpolarized cross section:

$$A_{LL} = \frac{\sum_i w_i a_{LL,i} \frac{\Delta f_i \Delta g_i}{f_i g_i}}{\sum_i w_i}, \tag{F.9}$$

where w_i is the usual weight from the cross section in the events partonic p_T bin.

This method is equivalent to the first method described in the application section, which we demonstrate:

$$\begin{aligned} A_{LL} &= \frac{N^{++} - N^{+-}}{N^{++} + N^{+-}} \\ &= \frac{\sum_i w_i (p(++|x) - p(+-|x))}{\sum_i w_i (p(++|x) + p(+-|x))} \\ &= \frac{\sum_i w_i a_{LL,i} \frac{\Delta f_i \Delta g_i}{f_i g_i}}{\sum_i w_i}. \end{aligned} \tag{F.10}$$

Bibliography

[1] J. Ashman et al. A measurement of the spin asymmetry and determination of the structure function g1 in deep inelastic muon-proton scattering. *Physics Letters B*, 206(2):364 – 370, 1988.

[2] Daniel de Florian, Rodolfo Sassot, Marco Stratmann, and Werner Vogelsang. Global Analysis of Helicity Parton Densities and Their Uncertainties. *Phys. Rev. Lett.*, 101:072001, 2008.

[3] A. N. Zelensky. High-intensity optically pumped polarized H- ion source development for RHIC and HERA. Prepared for 13th International Symposium on High-Energy Spin Physics (SPIN 98), Protvino, Russia, 8-12 Sep 1998.

[4] T Sakuma. *Inclusive Jet and Dijet Production in Polarized Proton-Proton Collisions at* $\sqrt{s} = 200$ *GeV at RHIC.* PhD dissertation, Massachusetts Institute of Technology, Department of Physics, December 2009. This is a full PHDTHESIS entry.

[5] R Jaffe and A Manohar. The g1 problem: Deep inelastic electron scattering and the spin of the proton* 1. *Nuclear Physics B*, Jan 1990.

[6] David Griffiths. *Introduction to Elementary Particle Physics.* Wiley, 1987.

[7] W Gerlach.... Das magnetische moment des silberatoms. *Zeitschrift für Physik A Hadrons and Nuclei*, Jan 1922.

[8] O Greenberg. Spin and unitary-spin independence in a paraquark model of baryons and mesons. *Physical review letters*, Jan 1964.

[9] Francis Halzen and Alan D. Martin. *Quarks and Leptons.* Wiley, 1984.

[10] R Taylor, J Friedman, G Hartmann, and H Kendall.... Inelastic electron-proton scattering at large momentum transfers and the inelastic structure functions of the proton. *Physical Review D*, Jan 1972.

[11] B. W. Filippone and Xiangdong Ji. The spin structure of the nucleon. *ADV.NUCL.PHYS.*, 26:1, 2001.

[12] John R. Ellis and Robert L. Jaffe. A Sum Rule for Deep Inelastic Electroproduction from Polarized Protons. *Phys. Rev.*, D9:1444, 1974.

[13] M. Glueck, E. Reya, M. Stratmann, and W. Vogelsang. Models for the polarized parton distributions of the nucleon. *Phys. Rev.*, D63:094005, 2001.

[14] M. Sarsour. *(STAR Collaboration), SPIN 2008 hep-ex/0901.4061,*, 2008.

[15] A. N. Zelenski, V. Klenov, S. A. Kokhanovski, V. Zoubets, G. Dutto, C. D. P. Levy, G. W. Wight, J. Alessi, and Y. Mori. Optically pumped polarized $H^?$ ion sources for RHIC and HERA colliders. *Hyperfine Interactions*, 127:475–479, August 2000.

[16] A. N. Zelenski and et al. Optically pumped polarized H- ion sources for RHIC and HERA colliders. In *Proceedings of the 1999 IEEE Particle Accelerator Conference. 29 Mar - 2 Apr 1999, New York, New York. 18th IEEE Particle Accelerator Conference, p.106-108*, pages 106–108, 1999.

[17] J. G. Alessi, J. M. Brennan, J. Brodowski, H. N. Brown, R. Gough, A. Kponou, V. Lodestro, P. Montemurro, K. Prelec, J. Staples, and R. Witkover. Performance of the New AGS RFQ Preinjector. In *Proceedings of the 1989 IEEE Particle Accelerator Conference. 20-23 Mar 1989, Chicago, Illinois 13th IEEE Particle Accelerator Conference., p.999*, pages 999–+, 1989.

[18] J. F. Sheehan, R. F. Lankshear, and R. L. Witkover. The RF System for the AGS Linac Injector. *IEEE Transactions on Nuclear Science*, 14:217–+, June 1967.

[19] Thomas Roser. High intensity beam operation of the brookhaven ags. *Workshop on instabilities of high intensity hadron beams in rings. AIP Conference Proceedings*, 496:22, Dec 1999.

[20] H Huang, L Ahrens, J Alessi, and M Bai. Polarized proton acceleration at the brookhaven ags-an ...., Jan 2002.

[21] M Brennan, I Marneris, T Roser, and A Ruggiero. Upgrading the ags to 1 mw proton beam power. ... *IL (US)*, Jan 2001.

[22] W MacKay, L Ahrens, M Brennan, and K Brown. Ags to rhic transfer line: Design and commissioning. *EPAC ...*, Jan 1996.

[23] H. Hahn, E. Forsyth, H. Foelsche, M. Harrison, J. Kewisch, G. Parzen, S. Peggs, E. Raka, A. Ruggiero, A. Stevens, S. Tepikian, P. Thieberger, D. Trbojevic, J. Wei, E. Willen, S. Ozaki, and S. Y. Lee. The RHIC design overview. *Nuclear Instruments and Methods in Physics Research A*, 499:245–263, March 2003.

[24] I. Alekseev, C. Allgower, M. Bai, Y. Batygin, L. Bozano, K. Brown, G. Bunce, P. Cameron, E. Courant, S. Erin, J. Escallier, W. Fischer, R. Gupta, K. Hatanaka, H. Huang, K. Imai, M. Ishihara, A. Jain, A. Lehrach, V. Kanavets, T. Katayama, T. Kawaguchi, E. Kelly, K. Kurita, S. Y. Lee, A. Luccio, W. W. MacKay, G. Mahler, Y. Makdisi, F. Mariam, W. McGahern, G. Morgan, J. Muratore, M. Okamura, S. Peggs, F. Pilat, V. Ptitsin, L. Ratner, T. Roser, N. Saito,

H. Satoh, Y. Shatunov, H. Spinka, M. Syphers, S. Tepikian, T. Tominaka, N. Tsoupas, D. Underwood, A. Vasiliev, P. Wanderer, E. Willen, H. Wu, A. Yokosawa, and A. N. Zelenski. Polarized proton collider at rhic. *Nuclear Instruments and Methods in Physics Research Section A: Accelerators, Spectrometers, Detectors and Associated Equipment*, 499(2-3):392 – 414, 2003. The Relativistic Heavy Ion Collider Project: RHIC and its Detectors.

[25] Harold Spinka. Proton beam polarimetry at bnl. *SPIN 2002: 15th International Spin Physics Symposium and Workshop on Polarized Electron Sources and Polarimeters. AIP Conference Proceedings*, 675:807, Jul 2003.

[26] H Okada, I Alekseev, A Bravar, G Bunce, S Dhawan, K. O Eyser, R Gill, W Haeberli, H Huang, O Jinnouchi, Y Makdisi, I Nakagawa, A Nass, N Saito, E Stephenson, D Sviridia, T Wise, J Wood, and A Zelenski. Absolute polarimetry at rhic. *POLARIZED ION SOURCES*, 980:370, Feb 2008.

[27] M Beddo, E Bielick, T Fornek, V Guarino, D Hill, et al. The star barrel electromagnetic calorimeter. *Nuclear Instruments and ...*, Jan 2003.

[28] M Anderson, J Berkovitz, and W Betts. The star time projection chamber: a unique tool for studying high multiplicity .... *Nuclear Instruments and ...*, Jan 2003.

[29] J Kiryluk and for the STAR Collaboration. Local polarimetry for proton beams with the star beam beam counters. *arXiv*, hep-ex, Jan 2005.

[30] C Adler, A Denisov, E Garcia, M Murray, H Strobele, and S White. The rhic zero-degree calorimeters. *Nuclear Instruments and Methods in Physics Research Section A*, 499:433, Mar 2003.

[31] Gavin P Salam. Towards jetography. *The European Physical Journal C*, 67:637, Jun 2010.

[32] J Huth, N Wainer, K Meier, and N Hadley.... Toward a standardization of jet definitions. *Fermilab-conf-90/ ...*, Jan 1990.

[33] G Blazey, J Dittmann, S Ellis, and V Elvira.... Run ii jet physics: Proceedings of the run ii qcd and weak boson physics workshop. *Arxiv preprint hep-ex*, Jan 2000.

[34] T Sjöstrand and S Mrenna.... Pythia 6.4 physics and manual. *Journal of High Energy ...*, Jan 2006.

[35] R Brun, F Bruyant, A C McPherson, and P Zanarini.... Geant3 users guide. *CERN DD/EE/84-1 ...*, Feb 1985.

[36] V Fine.... Oo model of star detector for simulation, visualization and reconstruction. *Computing in High Energy Physics-CHEP'2000*, 2000.

[37] B Andersson, G Gustafson, and G Ingelman.... Parton fragmentation and string dynamics. *Physics ...*, Jan 1983.

[38] T Sjöstrand. The lund monte carlo for jet fragmentation. *Computer Physics Communications*, Jan 1982.

[39] R Field. Pythia tune a, herwig, and jimmy in run 2 at cdf. *Arxiv preprint hep-ph*, Jan 2005.

[40] P Skands. Tuning monte carlo generators: The perugia tunes. *Arxiv preprint arXiv:1005.3457*, Jan 2010.

[41] A Buckley, H Hoeth, H Lacker, and H Schulz.... Systematic event generator tuning for the lhc. *The European Physical ...*, Jan 2010.

[42] M Betancourt, J Balewski, J Lauret, V Perevoztchikov, J Webb, and Q Xu. Targeted monte carlo: Filtered simulations at star. *STAR Note*, July 2010.

[43] T. Sakuma. *http://deltaq.lns.mit.edu/ sakuma/protected/wordpress/jets/incxsec/luminosity/jet2005805/*, 2009.

[44] J. Dunlop. *http://orion.star.bnl.gov/protected/common/common2005/trigger2005/ppDetails/*, 2005.

[45] G.C. Blazey et al. Run II jet physics. *hep-ex/0005012*.

[46] M. Cormier, A.I. Pavlinov, M.V. Rykov, V.L. Rykov, and K.E. Shestermanov. Star barrel electromagnetic calorimeter absolute calibration using "minimum ionizing particles" from collisions at rhic. *STAR Note*, July 2001.

[47] S. Frixione and G. Ridolfi. Jet photoproduction at HERA. *Nuclear Physics B*, 507(1-2):315 – 333, 1997.

[48] G. D'Agostini. *Nucl. Instr. Meth. A*, 362:487, 1995.

[49] J. Adams et al. *Phys. Rev. Lett.*, 91:172302, 2003.

[50] A Kocoloski. Run 5 btow systematic uncertainty studies.

[51] J. Adams et al. *Phys. Rev. C*, 70:054907, 2004.

[52] P. Djawotho. *http://drupal.star.bnl.gov/STAR/event/2009/01/11/jet-finding-techniques-workshop/*, 2009.

[53] M Sarsour. Inclusive jets double helicity asymmetry for polarized p+p collisions at $\sqrt{s}$ = 200 gev analysis note. *http://cyclotron.tamu.edu/star/2005n06Jets/anaNote.pdf*, 2008.

[54] D de Florian.... Resummed cross section for jet production at hadron colliders. *Physical Review D*, Jan 2007.

[55] A.D. Martin, R.G. Roberts, W. J. Stirling, and R.S. Thorne. *Phys. Lett. B*, 604:61, 2004.

[56] R. Field and R.C. Group. *hep-ph/0510198*, 2005.

[57] P Djawotho. First priority run list for jet analysis. *http://www4.rcf.bnl.gov/ pibero/spin/jets/HTML1/*, 2010.

[58] J Seele. Scaler qa for run 9 relative luminosity analysis. *http://drupal.star.bnl.gov/STAR/blog/seelej/2011/jan/11/relative-luminosity-studies-iv*, 2010.

[59] I Alekseev, E Aschenauer, G Atoyan, A Bazilevsky, R Gill, H Huang, S Lee, X Li, Y Makdisi, B Morozov, I Nakagawa, D Svirida, and A Zelenski. Run-09 pc polarimeter analysis.

[60] A Hoffman. Data/simulation comparison for π^0 mass positions. *http://drupal.star.bnl.gov/STAR/pwg/spin/run-6-neutral-pions/cross-section-analysis/data-mc-comparison*, 2009.

[61] T. Gehrmann and W. James Stirling. Polarized Parton Distributions in the Nucleon. *Phys. Rev.*, D53:6100–6109, 1996.

[62] A Deshpande, R Milner, and R Venugopalan.... Study of the fundamental structure of matter with an electron-ion collider. *Arxiv preprint hep-ph*, Jan 2005.

[63] X Ji. Generalized parton distributions. *Annual Review of Nuclear and Particle Science*, Jan 2004.

[64] J Balewski, J Seele, S Trentalange, and M Walker. Run9 btow hv mapping analysis - summary. *http://drupal.star.bnl.gov/STAR/subsys/bemc/calibrations/run-9-btow-calibration-page/02-comparing-2007-2008-and-2009-btow-slopes*, 2009.

[65] S Trentalange. Comparing 2007, 2008 and 2009 btow slopes. *http://drupal.star.bnl.gov/STAR/blog-entry/seelej/2009/mar/10/run9-btow-hv-mapping-analysis-summary*, 2009.

[66] G Popek and R Goldberg. Formal requirements for virtualizable third generation architectures. *Communications of the ACM*, Jan 1974.

[67] Jim Smith and Ravi Nair. *Virtual Machines: Versatile Platforms for Systems and Processes (The Morgan Kaufmann Series in Computer Architecture and Design).* Morgan Kaufmann Publishers Inc., San Francisco, CA, USA, 2005.

[68] L Stout, M Murphy, and S Goasguen. Kestrel: an xmpp-based framework for many task computing applications. ... *of the 2nd Workshop on Many-* ..., Jan 2009.